Development of Cu-based electrodes for proton-conducting membrane reactors

Shay Alexander Robinson

Dissertation for the degree of Philosophiae Doctor

Department of Chemistry

Faculty of Mathematics and Natural Sciences

UNIVERSITY OF OSLO

2017

Series of dissertations submitted to the
Faculty of Mathematics and Natural Sciences, University of Oslo
No. 1903

ISSN 1501-7710

Cover: Hanne Baadsgaard Utigard.

Print Production: Reprosentralen, University of Oslo.

Preface

This dissertation is submitted in partial fulfilment of the requirements for the degree of Philosophiae Doctor (PhD) at Department of Chemistry, Faculty of Mathematics and Natural Sciences, University of Oslo, Norway. The work has been carried out at the Centre for Materials Science and Nanotechnology (SMN) in the Group for Solid State Electrochemistry under the supervision of Professor Truls Norby during the period of June 1st, 2013 to August 8th, 2017.

Firstly, I express my warmest thanks and highest regards to my main supervisor Professor Truls Norby for many lively and insightful discussions, and for your invaluable and tireless help with the manuscripts and the final dissertation, but most of all for allowing me the opportunity to work freely. I also would like to express my gratitude to my co-supervisors Grover Coors and Christian Kjølseth, thanks for the encouragement and the opportunity to continue my education here at the University of Oslo.

Thanks to my friends and colleagues in SMN for not only the many scientific deliberations, but also for the warm and friendly social atmosphere, and the many, many Friday commiserations. A special thanks to Ragnar Strandbakke and Min Chen for being my fellow "electrodics", and the many insights and helpful tips you provided along the way towards both theoretical and experimental developments, and also to Matthias Schrade, Einar Vøllestad, Athanasios "Sakis" Chatzitakis and many others without whom this experience would have been much different.

I am tremendously thankful for the support of my loving family, to my friends on both sides of the pond, and to the fantastic ultimate community across Europe that I have gotten to know over the last four years. A pint size thank you to Pinner for being the best dog a man could wish for; from the street, to the mountains and now a world traveler, we truly have been through quite the storm.

Oslo, August 8th, 2017

Shay Alexander Robinson

This dissertation is dedicated to my loving family, thank you for believing in me, even when I didn't know how to believe in myself.

In memory of my grandfather,
LaRoy E. Robinson, 1923 - 2003

Summary

Proton conducting oxides are versatile materials with applications in not only fuel cell and water electrolysis technologies, but also in hydrogen production and chemical processing via membrane reactors. However, applications in carbon containing atmospheres are limited by the lack of effective electrodes that are stable at high temperatures, resistant to carbon deposition and catalytically active to hydrogen dissociation. Cu-based electrodes are known to be carbon tolerant, and CeO_2 is well used as an electrocatalyst, however to successfully characterize these materials as candidates for application as hydrogen electrodes, it is essential to have a good understanding of their combined effect on the kinetics of the hydrogen oxidation reaction (HOR).

The present work develops a new and simplified HOR model, and then applies the model in the analysis of the electrode reaction kinetics of point-contact, porous metal and infiltrated backbone electrodes, using data obtained with electrochemical impedance spectroscopy (EIS).

In Manuscript I, a point-contact model electrode configuration was first used to compare the reaction kinetics of Cu and Pt on the proton conducting yttrium-doped barium-cerate zirconate (BZCY) as functions of $p\mathrm{H}_2$ and temperature. The EIS data obtained was analyzed through the development of the simplified HOR model, which is based on Langmuir adsorption and Butler-Volmer charge transfer theories. The charge and mass transfer reaction mechanisms are then characterized through $p\mathrm{H}_2$ dependencies, site coverages, and activation enthalpies. The HOR model predicts the ranges of the $p\mathrm{H}_2^n$ dependencies to be, $-1/4 \leq n \leq 1/4$ for $1/\mathrm{R}_{ct}$, and $0 \leq n \leq 1$ for $1/\mathrm{R}_{mt}$. These ranges are based on the varying Langmuir $p\mathrm{H}_2$ dependencies of the hydrogen coverages at three phase boundary (3pb) and adsorption sites, given by associative or dissociative adsorption mechanisms. The experimental results established the applicability of the HOR model, and it was determined that the hydrogen coverages at adsorption and 3pb sites is very likely to be different, thus yielding different $p\mathrm{H}_2^n$ coverage terms which combine with the thermodynamically predicted $p\mathrm{H}_2$ depedencies.

Methods to improve the HOR kinetics of Cu-based electrodes are then the emphasis of the remaining work in this dissertation. This focuses on investigating how the addition of CeO_2 affects the kinetics of hydrogen oxidation, and uses infiltration as a method to prepare cermet-like multi-phase composite electrodes that are then characterized by a representative 3pb length.

At elevated temperatures Cu becomes a mobile species, however, other researchers have shown that it is thermally stabilized with the addition of Co, and performs well as a bimetallic Cu-Co composition. This composition was applied as a solvent based

metal nitrate solution, producing successive films that were decomposed to metal oxides and then reduced upon exposure to hydrogen. The influence of a surface coating of CeO_2 on the HOR kinetics of a Cu-Co electrode was compared to that of an electrode without the coating. Through the HOR model analysis of the pH_2 and temperature dependencies, it was determined that CeO_2 contributes to hydrogen dissociation. This is commonly considered to be part of chemical mass transfer, however, the effect was primarily observed in the charge transfer response of EIS spectra. The pH_2 dependencies identified a higher "apparent" coverage on the uncoated electrode than on the electrode with the CeO_2 coating, and the activation enthalpies indicated that this is due to site populations of molecular versus atomic hydrogen on the respective electrodes.

To further reduce the polarization resistance, and in an attempt to emulate the state-of-the-art Ni-cermet, two different types of backbone microstructures were investigated. As the first of their kind, macro-porous skeletal backbones were fabricated by co-sintering with a NiO-BZCY supported electrolyte membrane, and infiltrated with the CeO_2 coated Cu-Co composition. The measured pH_2 dependencies validated model predictions for low coverage, and the activation enthalpies suggested that the electrocatalyst was in a highly reduced state in the low pH_2O atm, such as $CeO_{2-\delta}$, and thus more active towards hydrogen dissociation. A micro-porous functional backbone of graded porosity was also fabricated on a pre-sintered NiO-BZCY72 supported membrane and infiltrated with a solvent based Cu-Co-Ce metal nitrate solution. By investigating successively higher annealing temperatures, it was observed that although the polarization resistance doubled, the electrode exhibited high performance. At the lower annealing temperature of 725 °C, the high activation enthalpy for mass transfer was indicative of a dissociative adsorption mechanism, while after annealing at 825 °C, the activation enthalpy had decreased considerably and the mass transfer mechanism had changed to dissociation after adsorption. This is further evidence for the coarsening of the infiltrated components, however this reduced the overall energy requirement of the HOR due to the exposure of more catalytically active CeO_2 on the surface of the infiltrated composition.

The charge transfer pre-exponential obtained from temperature dependencies is hypothesized to represent material specific properties and geometric factors associated with the 3pb region. We propose that there exists a proportionality between the inverse charge transfer resistance, the pre-exponential, $A_{0\,ct}$, and the 3pb length. Through the use of a pre-exponential with a known 3pb length, an unknown 3pb length can be estimated based on the ratio of the A_0's for the known and unknown values. A good correlation was observed between these parameters for the porous metal electrodes and the infiltrated backbones, and was further supported by the corresponding ASR values. This is adequate confirmation for the validity of this approach, and justifies further

investigations into this widely sought after parameter.

This work presents a new, simplified HOR model that is valuable in the analysis of $p\mathrm{H}_2$ dependencies obtained with impedance spectroscopy, and that in combination with temperature dependencies, may be used to identify charge and mass transfer reaction mechanisms. Unique methods for producing Cu-based electrodes are also presented, and the role of CeO_2 as an electrocatalyst in the hydrogen oxidation reaction is clarified. New methods for the fabrication of porous backbone microstructures have been established, and though the performance of the infiltrated electrodes presented here is only average, it is thought that the further optimization of infiltrated backbone electrodes shows great promise towards the eventual implementation in functional applications. As such, I have high hopes that this work, building on the progress of the many researchers, may be of benefit both to the scientific community and to the world at large.

Contents

1 Introduction **1**

1.1 Fossil Fuels are not the Hydrogen Solution 1

1.2 Background 2

Development of a state-of-the-art proton conducting electrolyte 2

Electrode development 3

Model anodes and extended microstructures 4

1.3 Practical Applications 5

Electrochemical conversion 5

Proof of concept demonstration 7

1.4 Literature Basis 8

Hydrogen Oxidation Reaction 8

Cu-based Electrodes 9

1.5 Content of this Dissertation 10

2 Theory **13**

2.1 Defect Chemistry 13

Oxygen vacancy formation in BZCY72 13

Proton incorporation in reducing atmospheres 14

2.2 Proton Transport 16

Mechanisms 16

Electrochemical transport 16

2.3 The Electrode Reaction Kinetics of Hydrogen Oxidation 18

Mass transfer: adsorption, dissociation and diffusion 19

The charge transfer interface: Butler-Volmer theory 23

The total polarization resistance 25

Temperature dependencies 28

Charge transfer pre-exponential 29

3 Synthesis **31**

3.1 Electrolytes 31

3.2 Backbone Microstructures 31

Example morphologies 32

3.3 Infiltrations 33

Solvent based solution 35

Thermal Stabilization 36

Catalytic modification 37

4 Experimental Methodology **39**
4.1 Test System . . . 39
4.2 Configurations . . . 40
Point-Contact Electrodes . . . 40
Ni-cermet supported membranes . . . 41
4.3 Electrochemical Measurements . . . 42
Impedance Spectroscopy . . . 42
Deconvolution of impedance spectra . . . 43
4.4 Data Analysis . . . 46
Error in fitting . . . 46
Uncertainty . . . 46
4.5 Hydrogen Flux . . . 48
Faradaic efficiency . . . 49

5 Manuscripts **51**
Manuscript I . . . 53
Manuscript II . . . 65
Manuscript III . . . 83
Manuscript IV . . . 97

6 Summarizing Discussion and Further Results **111**
6.1 HOR Model . . . 111
$p\mathrm{H_2}$ dependencies . . . 111
Temperature dependencies . . . 113
Reaction mechanisms . . . 114
Pre-exponentials . . . 116
6.2 Infiltrated backbones . . . 117
Microstructure . . . 117
Combination functional-skeletal backbones . . . 117
Infiltrations . . . 118
6.3 Further Results . . . 119
Hydrogen pumping . . . 119
6.4 Current challenges . . . 122
"Is YSZ stable in the presence of Cu?" . . . 122
Stability of the Cu-BZCY72 system . . . 122
6.5 Outlook . . . 123

7 Concluding remarks **127**

Bibliography **130**

8 Appendix **141**

Manuscript V 143

Manuscript VI 153

1 Introduction

1.1 Fossil Fuels are not the Hydrogen Solution

Hydrocarbons are critical to human welfare, and indeed, not only are they used as the primary energy source for most of the world, they provide the building blocks for much of the chemistry that produces plastics, polymers and other industrial products. Despite the fact that hydrocarbon sourcing and use has become the single largest contributor to the environmental challenges we face today, it will be difficult for modern society to progress without them, but as we transition to the use of new energy technologies, the ways in which hydrocarbon resources are utilized must change.

Natural gas, which has methane (CH_4) as the most significant component, offers a hydrocarbon resource that is cleaner and more efficient than coal or oil. Methane is a rich source of hydrogen, which is widely proclaimed to offer a sustainable solution to the worlds energy needs. In 2012, annual hydrogen production was estimated to be over 55 million tons, with a projected increase of 6% per annum, however, 96% of that was fossil fuel sourced, typically produced via the steam reforming of natural gas [1, 2].

Steam reforming: $$CH_4(g) + H_2O(g) \rightarrow 3H_2(g) + CO(g) \tag{1.1}$$

The product is syngas, composed of H_2 and carbon monoxide (CO), which may then be converted into methanol, higher alcohols or liquid hydrocarbons through the energy-intensive Fischer-Tropsch process [3, 4]. Alternatively, in the water-gas shift reaction syngas is converted to H_2 and carbon dioxide (CO_2).

Water-gas shift: $$CO(g) + H_2O(g) \rightarrow H_2(g) + CO_2(g) \tag{1.2}$$

As seen in (1.1) and (1.2), these methods of hydrogen production are carbon intensive, for every ton of CH_4 consumed, approximately 2.75 tons of CO_2 are produced, and as a result the fossil fuel derived product is termed “brown hydrogen”. For hydrogen to be a practical solution to the worlds energy needs, the net carbon emissions from production must be addressed, and as the above reactions demonstrate, current methods are significantly carbon positive [5].

Fortunately, developments in materials science and solid-state electrochemistry have enabled technologies that offer to help satisfy the need for clean hydrogen in carbon neutral or even carbon negative ways, and also to present alternative methods of hydrocarbon processing and providing industrial chemicals. Proton conducting perovskites are versatile materials with the potential to produce hydrogen in environmentally friendly and sustainable ways, to process and utilize hydrocarbons without directly contributing

to climate change and possibly to even help mitigate rising carbon dioxide levels in the atmosphere. Many of these applications are limited by the lack of effective electrodes that are stable at high temperatures, resistant to carbon deposition and catalytically active to hydrogen dissociation. Thus, the aim of this dissertation is to contribute to the development of an electrode with these characteristics that will aid in the implementation of these environmentally mitigating technologies.

1.2 Background

Development of a state-of-the-art proton conducting electrolyte

The pioneering research of Iwahara in the early 1980's showed the applicability of proton conductors to fuel cells, hydrogen production via steam electrolysis, as well as hydrogenation and dehydrogenation reactions, using the doped strontuim cerate, $SrCe_{1-x}M_xO_{3-\delta}$, family of materials [6, 7]. Following this work, numerous proton conducting materials were identified and have had a considerable history of development [8–13]. Kreuer published a widely cited review comparing the proton conductivities of numerous oxide compositions, as shown in Fig. 1.1, based on calculations by Norby and Larring, identifying yttrium-doped barium zirconate ($BaZr_{1-x}Y_xO_{3-\delta}$, BZY) as the most promising candidate for industrial applications [14, 15]. However, BZY ex-

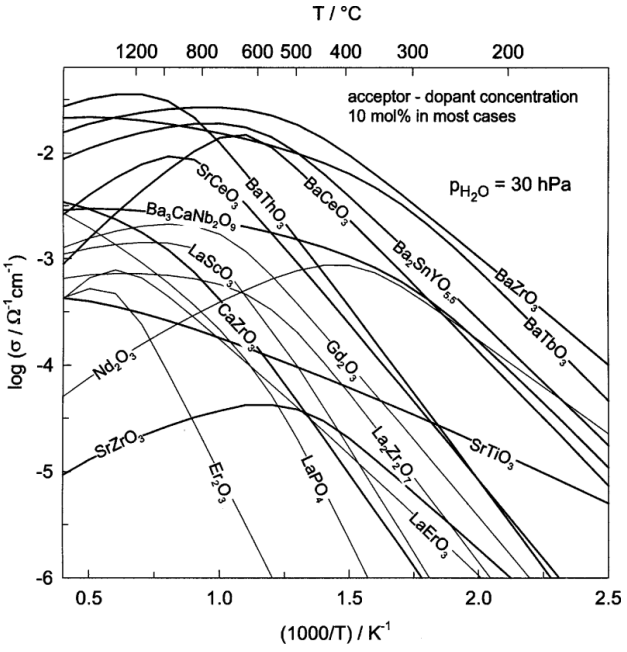

Figure 1.1: Proton conductivities of various perovskite oxides based on calculations by Norby & Larring. The conductivities of perovskite-type oxides are shown by bold lines [14, 15].

hibits relatively poor proton conductivity due to its high grain boundary resistance [16]. Yttrium-doped barium cerate, ($BaCe_{1-x}Y_xO_{3-\delta}$, BCY), exhibits high proton conductivity at relatively low temperatures and has a lower grain boundary resistance, but is unstable and forms barium carbonates in carbon-containing atmospheres [17–19]. Whereas the chemical stability of yttrium-doped barium zirconate BZY based electrolytes in carbon and H_2S containing atmospheres has been well documented [20–23].

In 2000, Iwahara's group first isolated the solid solution of yttrium-doped barium zirconate with cerium substitution ($BaZr_{1-x-y}Ce_xY_yO_{3-\delta}$, BZCY), and reported on the significant mixed conductivity at high temperatures [24]. The advent of BZCY presented a material that exhibits the most desirable characteristics of both of its constituents, high proton conductivity as well as chemical stability [15, 24–26]. BZCY has since been shown to be able to perform well as fuel cells, hydrogen pumps and membrane reactors, and these advances demonstrate that BZCY based systems can be used for many applications including gas separation and chemical conversion through hydrogenation and dehydrogenation reactions [27–31].

Electrode development

As the development of BZCY has matured, the need for high performance electrodes has slowed the implementation of proton-conducting ceramic membranes in industrial processes. Considerable research has been devoted to oxygen electrodes, where some of the best candidates are based on advances adopted from the SOFC community, these include $La_{1-x}Sr_xMnO_{3-\delta}$ (LSM), $La_{0.6}Sr_{0.4}Co_{0.2}Fe_{0.8}O_{3-\delta}$ (LSCF) and $Ba_{0.5}Sr_{0.5}Co_{0.8}Fe_{0.2}O_{3-\delta}$ (BSCF) [32–36]. More recently, so-called triple conducting oxides have been developed and are hypothesized to have high conductivities of protons, oxide ions and electron holes. These include the compositions $Ba_{0.5}Gd_{0.8}La_{0.7}Co_2O_{6-\delta}$ (BGLC), $BaCo_{0.4}Fe_{0.4}Zr_{0.1}Y_{0.1}O_{3-\delta}$ (BCFZY), $Pr_{0.4}Sr_{0.6}Co_{0.2}Fe_{0.7}Nb_{0.1}O_{3-\delta}$ and $Sr_3Fe_2O_{7-\delta}$, all of which have reported better performance than both BSCF and LSCF [37–40].

For all these advances in oxygen electrodes, hydrogen electrodes have yet to show any truly innovative developments. The Ni-cermet (**cer**amic-**met**al) electrode has remained the benchmark SOFC anode for well over 50 years [41]. In Ni-cermets, the ceramic phase is primarily structural but also provides a conduction path for ions, and the extended three-phase boundary (3pb) of the metal-electrolyte interface provides innumerable reaction sites. However, it is the catalytic activity of Ni towards H_2 oxidation that makes Ni-cermets such good electrodes, but this is also a disadvantage to applications in carbon or sulphur containing fuels. Ni catalyzes significant coke formation and is also susceptible to sulphur poisoning, leading to the loss of tpb sites and the subsequent deactivation of the electrode. As a result, a carbon and sulphur tolerant

anode is required to successfully implement BZCY based proton conductors in natural gas or biogas applications.

Cu is a well used material that is known for its excellent conductivity, wide availability and it's resistance to corrosion and carbon deposition. As such, it has been proposed to utilize Cu as an anode electrode for PCMR dehydrogenation reactions in order to implement proton conducting electrochemical devices in industrial applications using hydrocarbon fuels.

Model anodes and extended microstructures

To successfully use Cu as an electrode, it is essential to have a good understanding of the behavior of Cu at the metal-proton conducting electrolyte interface. Model anodes, such as point-contact electrodes, are characterized by an easily measurable and well defined geometry, and are useful configurations for investigations into fundamental electrode hydrogen oxidation kinetics. These types of electrodes remove variables such as microstructure, and allow detailed studies of the three phase boundary (3pb), where the ionic, electronic and gas phases interact. Fig. 1.2 illustrates examples of a point-contact model electrode, a porous metal electrode and a more complicated cermet electrode with an extended 3pb. Point-contact electrodes typically consist of a small diameter metal

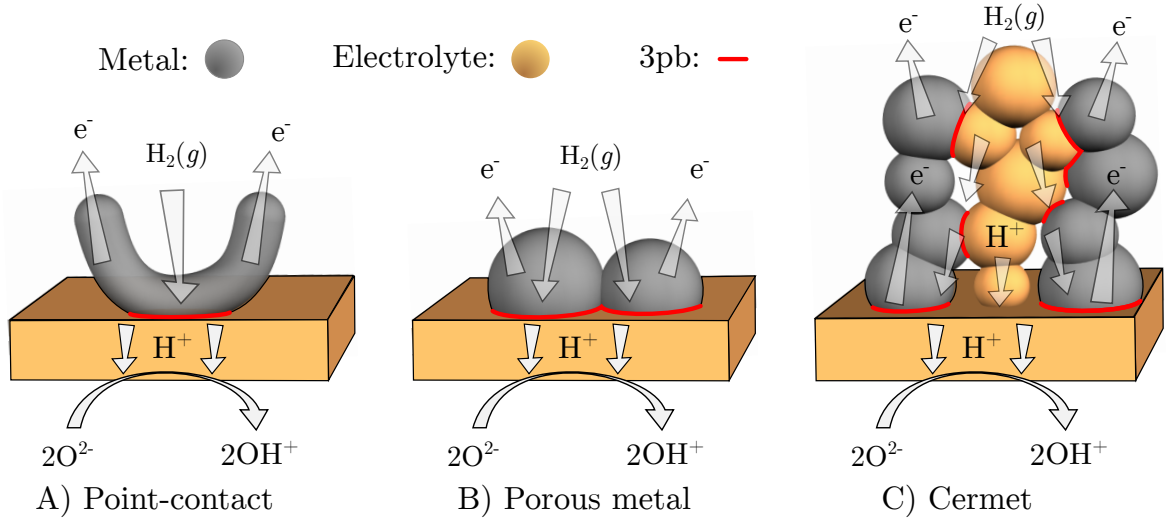

Figure 1.2: Schematics of a A) metal point-contact electrode and a B) porous metal film, typically painted or screen printed onto an electrolyte, and C) a typical cermet type microstructure, with an extended microstructure composed of both ionic and electronically conducting phases, adapted from [42].

wire bent around a support and pressed against the electrolyte surface. This yields a roughly elliptical contact area, the perimeter of which is considered to be the 3pb. This makes the 3pb of the point-contact electrode directly measurable using methods

such as SEM imaging. Thin porous metal electrodes also have a well defined 3pb that can be measured using SEM imaging, but the total 3pb length of the entire electrode must be estimated through correlation with an area specific 3pb length. The extended 3pb length of cermet type electrodes is much more complex, and direct measurement is not possible due to the highly tortuous microstructure. It is proposed in this work that there exists an empirical method to estimate the 3pb length of an electrode with a known 3pb specific resistivity, and that this method may be extended to more complex geometries such as cermet type electrodes.

1.3 Practical Applications

Electrochemical conversion

Proton conducting solid state electrochemical devices can be used as power generating fuel cells, but can also be powered by renewable energy sources, such as solar, wind and geothermal, and used for steam electrolysis as well as hydrogenation and dehydrogenation reactions. The global fuel cell (PCFC) and steam electrolysis (PCEC) reactions are shown in Eq. (1.3),

$$\mathrm{H_2}(g) + {}^1\!/_2\,\mathrm{O_2}(g) \rightleftharpoons \mathrm{H_2O}\,(g) \tag{1.3}$$

Their working principles are illustrated in Fig. 1.3, as applied to fuel cells in the forward direction, and to electrolyzers in the reverse direction. Proton-conducting oxides have

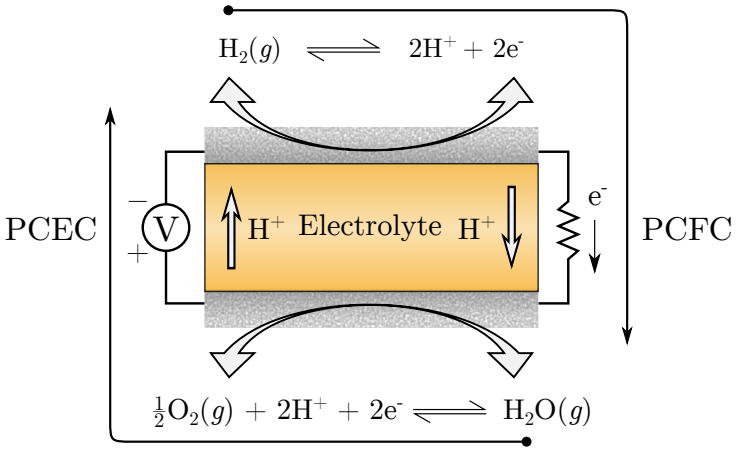

Figure 1.3: Schematic of a proton-conducting solid state electrolyte, shown as a fuel cell (PCFC) in the forward direction and an electrolyzer (PCEC) in the reverse direction.

attracted increased attention due to lower operating temperatures than oxide ion conductors. When operated as PCFC's, they also offer the benefits of high efficiency and

zero emissions, the product water vapor is produced on the oxygen side of the electrolyte and there is no issue with fuel dilution. Hydrogen can also be produced through steam electrolysis using a proton conductor (PCEC), producing an ultra-purified product [43].

When proton conducting electrolytes are applied as catalytic membrane reactors (PCMR's), they are capable of facilitating many different hydrogenation and dehydrogenation reactions [44]. The general form for a reaction describing the hydrogenation (forward) or dehydrogenation (reverse) of chemical compounds is,

$$\mathrm{A} + \mathrm{H_2}(g) \rightleftharpoons \mathrm{B} \tag{1.4}$$

If the triple covalent bond of the N_2 molecule can be catalytically broken, nitrogen from air can be hydrogenated to produce ammonia hydroxide, which is stable at atmospheric pressure and temperature [45–47]. Alternatively, CO_2 can also be hydrogenated, generating valuable chemical products such as methanol or dimethyl ether [48]. A schematic of PCMR hydrogenation, illustrating the N_2 and CO_2 reactions, is shown in Fig. 1.4,

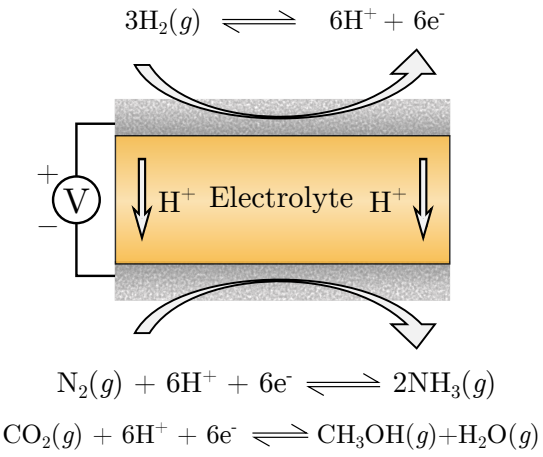

Figure 1.4: Schematic of a proton-conducting membrane reactor, illustrating the hydrogenation of N_2 and CO_2, to produce NH_3 and CH_3OH.

Methane and ethane can be catalytically dehydrogenated and the hydrogen byproduct removed by hydrogen pumping, producing not only ultra-pure hydrogen, but also valuable industrial chemicals such as ethylene and benzene [31, 49–51]. Thus it is possible to both use hydrocarbon fuels in an environmentally sustainable way, for example by using anthropogenic methane to produce both valuable chemicals as well as ultra-pure hydrogen. However, the biggest challenge to the implementation of PCMR's in industrial processes is the lack of carbon stable and catalytically effective electrodes, and though there has been encouraging recent progress, this still remains a significant obstacle.

Proof of concept demonstration

Originated by Protia AS (now CoorsTek Membrane Sciences AS, CMS), it was proposed to directly convert inlet hydrocarbons gases to liquid fuels and other chemicals using a PCMR in a single-step catalytic process. This was made possible by ceramic engineering advances by CoorsTek Inc. in Golden, CO. USA, that enabled the fabrication of NiO-BZCY72 cermet supported electrolyte membranes. The reactive sintered NiO-BZCY72 cermet electrode supports were fabricated both by extrusion and slip casting, and then spray coated with a slurry of the membrane precursors, prior to high temperature sintering. Both fuel cell and hydrogen pumping operation was demonstrated using an LSCF electrode painted on the BZCY72 electrolyte coated tubes, providing precedent for further technological developments [28, 29].

In 2015, CMS demonstrated the one-step catalytic process of the direct conversion of CH_4 to benzene over an MCM-22 catalyst [49]. The methane dehydroaromatization reaction describing the production of C_6H_6 over the MCM-22 catalyst is shown in Eq. (1.5), with a schematic

$$6CH_4 \longrightarrow C_6H_6 + 9H_2 \qquad (1.5)$$

of the catalytic membrane reactor shown in Fig. 1.5. It was demonstrated that the reaction was enhanced by the use of proton ceramic membranes, facilitated by LeChatelier's principle, removing the product hydrogen from the reaction zone. It was also reported that the non-negligible oxide-ion conductivity of BZCY72 improved conversion rates by removing carbon depositions from the catalyst surface, however, this concept could be extended to the electrode as well. In such a case, a Cu-based anode, as shown in Fig. 1.5, would also benefit from the removal of carbon deposits.

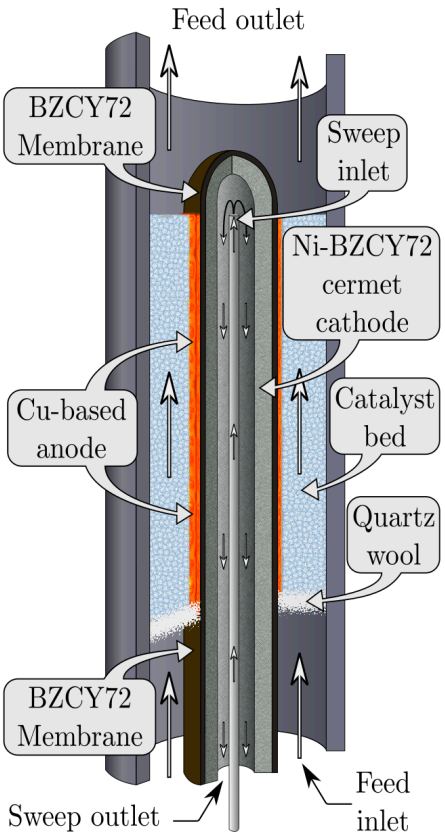

Figure 1.5: Illustration of the PCMR used by Morejudo et al. in the direct conversion of CH_4 to C_6H_6, adapted from [49].

1.4 Literature Basis

This brief review is included only as a point of reference to provide the basis for the developments presented in this dissertation. Hydrogen oxidation has been studied since the early history of electrochemical devices, and the general theory of mass and charge transfer is well established. The mass transfer processes on metallic Cu are well reported in literature, and theory is backed up by many experimental studies. However, the charge transfer mechanism is not widely reported for the proton conducting metal-electrolyte interface.

Hydrogen oxidation reaction

The hydrogen oxidation reaction (HOR) is well studied in SOFC literature, but in order to extend this to electrode kinetics on proton-conducting ceramics, one should have a reasonable understanding of the relevant processes. This section would be quite exhaustive if all of the pertinent resources were mentioned, thus only the specific body of knowledge critical to the development of the HOR model reported in this work is reviewed. The central tenet of the HOR model developed herein is that it proceeds through a number of elementary steps, and these steps are then extended through the use of reaction rate theory [52].

First are the mass transfer steps of adsorption, dissociation and diffusion, all of which are elementary processes that are well described by thermodynamics and the conservation of mass. There is extensive literature on associative and dissociative hydrogen adsorption both specific to Cu and generalized to metal surfaces, however Christmann provided an excellent review in 1988, and in particular noted that although there are general trends associated with the evaluation of activation enthalpies, there is no clear consensus [53]. Similar to the analogous work by Kim et al. on oxygen electrodes using LSM on a YSZ electrolyte, here, the activity of hydrogen is considered to be equivalent to surface coverage, and by extension to the $p\mathrm{H}_2$ [32]. Following mass transfer, a single-electron charge transfer reaction takes place that is described by the general Butler-Volmer formalism. This is done using the form of the equation for the hydrogen oxidation half-cell as given by O'Hayre et al. in the 2009 textbook, "*Fuel Cell Fundamentals*" [54]. In chapter 2 of *"The CRC Handbook of Solid State Electrochemistry"*, Gerischer presents a derivation of the electrostatic potential at a hydrogen electrode based on the Galvani potentials of a metal electrode-electrolyte interface [55]. Additionally, in *"Electrochemical Methods"*, Bard and Faulkner provide insight into the treatment of mass transfer [56]. These concepts are then related to proton conducting ceramics through the relevant transport equations and defect equilibria within the

electrolyte.

Cu-based electrodes

Among the first attempts to utilize Cu as an anode for SOFC operation was the work reported by Park et al. in 1999 at the University of Pennsylvania [57]. Using a yttria-stabilized zirconia (YSZ) electrolyte, a porous scaffold was prepared by tape casting and co-sintered with the electrolyte, then infiltrated with aqueous Cu nitrates. The resulting Cu-YSZ structure was not active to methane oxidation, and carbon deposition did not occur. Based on some of the Gorte groups previous studies, CeO_2 was then added as an electrocatalyst, and reasonable fuel cell performance was obtained [57–60]. There was no mention of whether or not carbon deposition ocurred after the addition of CeO_2.

In 2001, Kiratzis et al. performed a similar study, using a Cu-titania doped yttria-stabilized zirconia (Cu-YTZ) cermet anode with a YSZ electrolyte at the University of St. Andrews [61]. This study reported similar results, but also detailed the general lack of thermal stability of Cu-cermet anodes at high temperature, leading to significant degradations in performance. This paper concluded that Cu-based cermet electrodes produced by that method were not promising candidates for high temperature applications. However, the research on Cu-based cermets continued at both institutions with the further development of advanced synthesis techniques and electrochemical characterization [62–65].

In 2004, the Gorte and Irvine research groups together published the article by Atkinson et al. titled “Advanced anodes for high-temperature fuel cells” in *Nature*, which based on the above works reviewed both advantages and disadvantages of Cu-cermets [66]. The Gorte group continued their research on Cu-based cermet electrodes, with efforts primarily focused on the thermal stabilization of Cu, and by 2007, this had been accomplished through the use of both Co and Cr [67–70]. The more relevant development of this work was the utilization of the immiscible metal phases, Cu and Co, where it was found that Cu will diffuse through electrodeposited Co, forming a monolayer of the carbon resistant metal on top of the Co; which would otherwise susceptible to carbon deposition. Additionally, through the addition of CeO_2 to the infiltrated Cu-YSZ anode structure, an SOFC operating on pure H_2 could be fed H_2S at concentrations of up to 200 ppm, with no decrease in power density [71]. The Gorte group apparently concluded their work on Cu-YSZ cermets in 2007 with the final dissemination of their findings, emphasizing that much work remains for developing the novel Cu-based anode for hydrocarbon applications [72].

1.5 Content of this Dissertation

The remainder of this dissertation is composed of the following sections:

- Chapter 2 offers a brief synopsis of the relevant defect chemistry in reducing atmospheres and proton transport mechanisms, the more fundamental aspect of this work focuses on the hydrogen oxidation electrode reaction kinetics at the metal-electrolyte interface.
- Chapter 3 generalizes the ceramic engineering of porous backbone microstructures, and includes the development of a solvent-based infiltration solution used to introduce both electronically conducting and electrocatalytically active components, forming a cermet type electrode.
- Chapter 4 describes the experimental configurations, electrochemical measurement techniques and data analysis procedures.
- Chapter 5 then presents the scientific contributions of this dissertation as a collection of published and unpublished manuscripts; a brief description of their content given below:

Manuscript I (MI): **"Comparison of Cu and Pt point-contact electrodes on proton conducting $\mathbf{BaZr_{0.7}Ce_{0.2}Y_{0.1}O_{3-\delta}}$"**

Shay Robinson, Christian Kjølseth, Truls Norby
Solid State Ionics, 306 (2017) 38−47

As a fundamental study, the electrode reaction kinetics of the Cu and Pt metal-electrolyte interface on a proton conducting ceramic are investigated. A simplified HOR model is developed to explain the $p\mathrm{H_2}$ dependencies of mass and charge transfer conductances, as determined through impedance spectroscopy.

Manuscript II (MII): **"Thermally stable Cu-Co electrodes with and without $\mathbf{CeO_2}$ activation on a $\mathbf{BaZr_{0.7}Ce_{0.2}Y_{0.1}O_{3-\delta}}$ proton conducting electrolyte"**

Shay Robinson, Christian Kjølseth, Truls Norby
To be submitted to the Journal of Hydrogen Energy

This work introduces the use of a solvent based infiltration solution, and the thermal stabilization of Cu is accomplished through the addition of Co. The effects of CeO_2 as an electrocatalyst are investigated, and the HOR model is used to interpret data obtained through impedance spectroscopy. SEM imaging is used to estimate the area specific tpb length, and this is related to the charge transfer pre-exponential of the temperature dependencies.

Manuscript III (MIII): **"Infiltration of Cu-Co and CeO_2 in a BZCY72 backbone co-sintered with a NiO-BZCY72 supported electrolyte"**

Shay Robinson, Christian Kjølseth, Truls Norby
In preparation

A co-sintered backbone is fabricated on a section of NiO-BZCY72 electrode supported membrane, and then infiltrated with a Cu-Co solvent-based solution. CeO_2 is used as an electrocatalyst at the metal-electrolyte interface, and the HOR model is used to interpret both biased and unbiased data obtained through impedance spectroscopy. The exhibited $p\mathrm{H}_2$ dependencies agree with model predictions, and the charge transfer pre-exponential obtained from the temperature dependencies indicates that this skeletal type co-sntered backbone yields a comparable area specific tpb length, as compared to the porous Cu-Co electrode from MII.

Manuscript IV (MIV): **"Performance of Cu-Co-CeO_2 infiltrated graded backbone on a Ni-cermet supported $BaZr_{0.7}Ce_{0.2}Y_{0.1}O_{3-\delta}$ electrolyte"**

Shay Robinson, Christian Kjølseth, Truls Norby
In preparation

A graded porosity backbone is applied to a section of pre-sintered NiO-BZCY72 electrode supported membrane and infiltrated with a Cu-Co-Ce solvent-based solution. The thermal stability of the infiltrated composition is evaluated as a function of thermal cycling, and theories are postulated for the observed changes in charge and mass transfer activation enthalpies. The charge transfer pre-exponential is then used to estimate the area specific 3pb length for this cermet microstructure.

- Chapter 6 then reviews the key findings and developments of this work, and collectively discusses the obtained results.
- Chapter 7 presents further results that were not included in the manuscripts but that may be relevant to future work, and reviews the remaining challenges and outlook.

Two further manuscripts are also included in the appendix that, although relevant to parts of this work, were not directly tied to the theoretical developments herein:

Manuscript V (MV): **"Galvanic hydrogen pumping in the protonic ceramic perovskite $BaZr_{0.7}Ce_{0.2}Y_{0.1}O_{3-\delta}$"**

Shay Robinson, Anthony Manerbino, W. Grover Coors
Journal of Membrane Science, 446 (2013) 99−105

This earlier work demonstrated the stability of BZCY72 membranes under galvanic operation at high-current, providing the precedent for the use of BZCY, and for further investments by CoorsTek Inc. into research and development in this area. Using an LSCF cathode on a Ni-cermet supported BZCY72 membrane, galvanic hydrogen flux was quantified from 650 to 800 °C, up to a 1 $A\,cm^{-2}$ current density.

Manuscript VI (MVI): **"$Ba_{0.5}Gd_{0.8}La_{0.7}Co_2O_{6-\delta}$ Infiltrated in Porous $BaZr_{0.7}Ce_{0.2}Y_{0.1}O_{3-\delta}$ Backbones as Electrode Material for Proton Ceramic Electrolytes"**

R. Strandbakke, E. Vøllestad, S. Robinson, M. L. Fontaine, T. Norby
Journal of the Electrochemical Society, 164 (2017) F196−F202

The performance of different BGLC infiltrated backbone microstructures were compared to that of a homogeneous ink of the triple conducting oxide. No noticeable improvements were obtained using the infiltrated backbones, suggesting that the high performance obtained with this material is due increased proton, oxide ion and hole conductivity. (I contributed to this work through the development of an optimized backbone microstructure)

2 Theory

In this chapter I first will touch upon the basics of defect formation, hydrogen incorporation and transport through the electrolyte. Then the reaction kinetics at the hydrogen electrode are described, and include the development of a simplified hydrogen oxidation model that is used to interpret the pH_2 dependencies obtained in this work.

2.1 Defect Chemistry

Oxygen vacancy formation in BZCY72

Transport in proton conducting oxides occurs largely due to the presence of oxygen vacancy defects in the crystalline lattice structure. Intrinsic defect formation in stoichiometric compounds occurs through Schottky disorder, resulting in both anion and cation vacancies, through Frenkel disorder, resulting in interstitial anions or cations (and the respective vacancy), and through the ionization of electrons. For non-stoichiometric oxygen-deficient compounds, written in Kröger-Vink notation, oxygen vacancies are created according to,

$$O_O^x \Leftrightarrow v_O^{\bullet\bullet} + 2e' + \frac{1}{2}O_2\,(g) \tag{2.1}$$

resulting in the evolution of oxygen gas; the electrons are delocalized in the conduction band. Material scientists promote oxygen vacancy formation through substitutional acceptor doping by introducing foreign aliovalent metal oxides. For ABO_3 perovskites, such as shown in Fig. 2.1, this is written as $AB_{1-x}Bf_xO_{3-\delta}$, where the substitutional B-site doping, x, of a foreign lower valent cation, (Bf), results in the formation of oxygen vacancies. In the case of oxygen deficient barium zirconate, $BaZr_{1-x}Y_xO_{3-\delta}$ (BZY), the

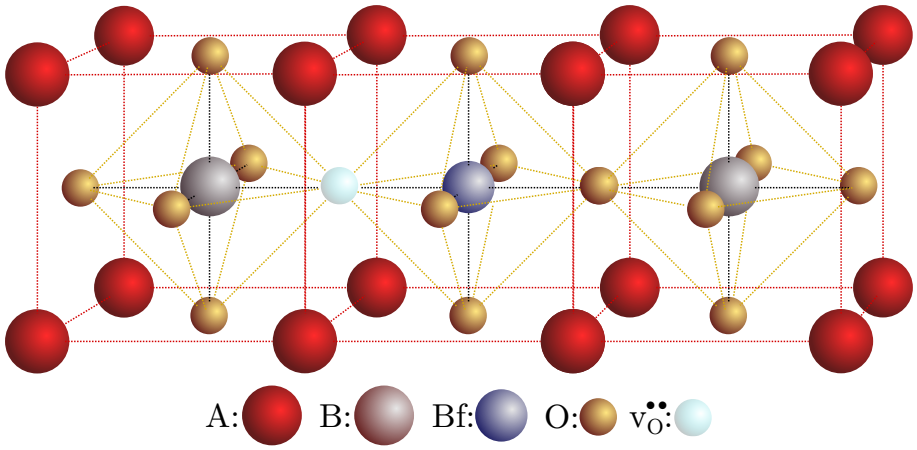

Figure 2.1: The ABO_3 perovskite structure, where B site doping of a lower valent cation, Bf, will promote the formation of oxygen vacancies, $v_O^{\bullet\bullet}$.

equation describing the substitution of yttrium onto a zirconia B site is,

$$Y_2O_3\,(s) \overset{ZrO_2}{\Longleftrightarrow} 2Y'_{Zr} + 2O_O^{\times} + v_O^{\bullet\bullet} + \tfrac{1}{2}O_2(g) \tag{2.2}$$

The research performed in this dissertation utilizes yttrium-doped barium cerate zirconate oxide, $BaZr_{1-x-y}Ce_xY_yO_{3-\delta}$ (BZCY). The oxidation state of Ce in CeO_2 is the same as that of Zr in ZrO_2, and so the doping equation appears the same for $BaCeYO_{3-\delta}$, however the characteristics of the Ce cation substitution on the b-site are significantly different [73]. Ce is known to change oxidation states from Ce^{4+} to Ce^{3+} when exposed to hydrogen containing atmospheres, creating an effectively negative charged Ce cation in addition to an additional oxygen vacancy [74–76]. The reduction would proceed as,

$$H_2\,(g) + 2Ce_{Zr}^{\times} + O_O^{\times} \Longleftrightarrow 2Ce'_{Zr} + v_O^{\bullet\bullet} + H_2O\,(g) \tag{2.3}$$

This gives rise to an increase in both electronic and ionic conductivity, which is not desirable from a pure proton-conducting point of view. However, mixed conductivity is reported to be beneficial for some applications where carbon deposition is problematic, as oxygen reacts with C to form CO or CO_2 [31, 49, 77].

Proton incorporation in reducing atmospheres

In wet reducing atmospheres, protons are incorporated into materials such as BZCY through both the hydration of oxygen vacancies and the hydrogenation of oxide ions [78]. When protons and oxygen vacancies charge compensate the negatively charged acceptor dopant, $[Y'_{Zr}]$, the electroneutrality condition reads, $[Y'_{Zr}] = 2[v_O^{\bullet\bullet}] + [OH_O^{\bullet}]$, and has two limiting cases which can be used to determine the proton concentration. In water-vapor saturated atmospheres, protons are equilibrated with oxygen vacancies and oxide ions according to the hydration reaction,

$$H_2O\,(g) + O_O^{\times} + v_O^{\bullet\bullet} \Longleftrightarrow 2OH_O^{\bullet} \tag{2.4}$$

Here, an oxide ion has dissolved into and occupied the vacancy, filling the empty lattice position. The hydrogen has also dissolved into the lattice and is now associated with the oxide ions as hydroxides. Through the mass action law, the corresponding equilibrium constant is,

$$\mathbf{K}_{H_2O} = \frac{[OH_O^{\bullet}]^2}{[O_O^{\times}][v_O^{\bullet\bullet}]pH_2O} = \exp\left(-\frac{\Delta G^0_{H_2O}}{RT}\right) = \exp\left(\frac{\Delta S^0_{H_2O}}{R}\right)\exp\left(-\frac{\Delta H^0_{H_2O}}{RT}\right) \tag{2.5}$$

In this condition where oxygen vacancies are fully hydrated and protons predominate, such as at intermediate temperatures, the concentration of protons can be approximated directly by,

$$[\mathrm{OH}_{\mathrm{O}}^{\bullet}] \approx [\mathrm{Y}'_{\mathrm{Zr}}] = \text{constant} \tag{2.6}$$

Alternatively, in lower $p\mathrm{H_2O}$ atmospheres, where protons are the minority, the electroneutrality condition is then approximated by,

$$2[\mathrm{v}_{\mathrm{O}}^{\bullet\bullet}] \approx [\mathrm{Y}'_{\mathrm{Zr}}] = \text{constant} \tag{2.7}$$

From (2.5), the concentration of protons is given by,

$$[\mathrm{OH}_{\mathrm{O}}^{\bullet}] = \sqrt{\mathbf{K}_{\mathrm{H_2O}}[\mathrm{O}_{\mathrm{O}}^{\times}][\mathrm{v}_{\mathrm{O}}^{\bullet\bullet}]p\mathrm{H_2O}} \tag{2.8}$$

Upon substituting the above electroneutrality approximation, (2.7), the thermodynamic properties for $\mathbf{K}_{\mathrm{H_2O}}$ with the concentration of oxide ions on oxygen sites $[\mathrm{O}_{\mathrm{O}}^{\times}] \approx 1$, the concentration of protons is

$$[\mathrm{OH}_{\mathrm{O}}^{\bullet}] = \frac{1}{\sqrt{2}}[\mathrm{Y}'_{\mathrm{Zr}}]^{1/2}p\mathrm{H_2O}^{1/2}\exp\left(\frac{\Delta S^0_{\mathrm{H_2O}}}{2R}\right)\exp\left(-\frac{\Delta H^0_{\mathrm{H_2O}}}{2RT}\right) \tag{2.9}$$

As the $p\mathrm{H_2O}$ decreases further, the conductivity decreases due to depleted charge carrier concentrations [16, 17, 79]. The hydration reaction no longer dominates and the protonation mechanism changes to hydrogenation. This reaction can be written numerous ways, the simplest is if the protons are charge compensated by electrons,

$$\frac{1}{2}\mathrm{H_2\,(g)} + \mathrm{O}_{\mathrm{O}}^{\times} \Longleftrightarrow \mathrm{OH}_{\mathrm{O}}^{\bullet} + \mathrm{e}' \tag{2.10}$$

Electrons may interact with other defects so that the protons are compensated by the formation of new defects. In Ce containing BZCY compounds, the Ce may change oxidation states according to the following,

$$\frac{1}{2}\mathrm{H_2\,(g)} + \mathrm{O}_{\mathrm{O}}^{\times} + \mathrm{Ce}_{\mathrm{Zr}}^{\times} \Longleftrightarrow \mathrm{OH}_{\mathrm{O}}^{\bullet} + \mathrm{Ce}'_{\mathrm{Zr}} \tag{2.11}$$

2.2 Proton Transport

Mechanisms

After incorporation into the crystal structure, a proton initially resides in the electron cloud of a lattice oxygen as the hydroxide defect, $OH_O^{\bullet}$. In principle, protons are mobile through two primary means: free transport, also termed the Grotthus mechanism, and the vehicle mechanism. The Grotthus mechanism is widely acknowledged to be primarily responsible for proton transport through materials such as BZY. As the crystal lattice vibrates, the proton rotates around the oxide ion, and when lattice vibrations bring oxide ions closer together, the proton will then hop from one oxygen site to another. The sequence of steps in the Grotthuss mechanism are illustrated graphically in Fig. 2.2. In the vehicle mechanism the oxide ion carries the proton and moves as a

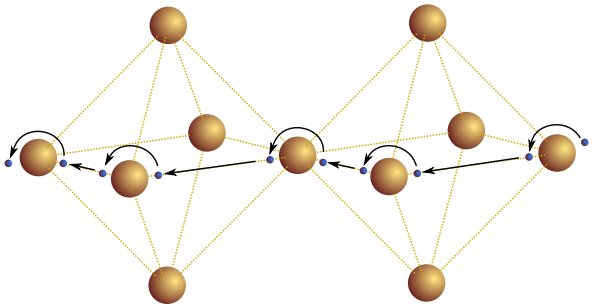

Figure 2.2: Graphical depiction of the Grotthuss mechanism, involving the diffusional rotation of a proton (in blue) around oxide ions (in yellow) and hopping to a neighboring oxide ion.

hydroxide, transporting by way of adjacent oxygen vacancies.

The activation enthalpy for the mobility of protonic defects in BZCY varies from around 0.4 to 0.6 eV [16, 80]. However, the activation enthalpy of the rotational reorientation is near 0.1 eV [14], and that of the longer range proton transfer step is near 0.15 eV [15]. This discrepancy is typically attributed to trapping through proton-dopant association, and to the notoriously high grain boundary impedance of barium zirconate based ceramics [81].

Electrochemical transport

As protons are one amongst numerous charged species in BZCY, the following treatment is generalized to encompass all charged species; for practical calculations the sign of the charge indicates the direction of flux. The equations describing the diffusion of a charged species i in an electrochemical potential gradient can be derived using Ficks

law,

$$\boldsymbol{J}_i = -D_i \frac{\chi_i}{RT} \boldsymbol{\nabla} \tilde{\mu}_i \tag{2.12}$$

Here, $\boldsymbol{J}_i$ is the flux vector, D_i is the diffusivity, χ_i is concentration and is proportional to activity through $a_i = \chi_i/\chi_{i,0}$, R is the universal gas constant and T is temperature. $\boldsymbol{\nabla}$ is the gradient operator, and the electrochemical potential, $\tilde{\mu}_i$, is defined as,

$$\tilde{\mu}_i = \mu_i^0 + RT \ln\left(\frac{\chi_i}{\chi_{i,0}}\right) + z_i F \phi_i \tag{2.13}$$

where μ_i^0 is the standard chemical potential, z_i is charge and ϕ_i is electrostatic potential. If we limit the problem by restricting it to one dimensional diffusion across the membrane in only the x-direction, then,

$$\frac{\partial \tilde{\mu}_i}{\partial x} = \frac{RT}{\chi_i}\frac{\partial \chi_i}{\partial x} + z_i F \frac{\partial \phi_i}{\partial x} \tag{2.14}$$

After performing the differentiation, and by utilizing the Einstein relation between diffusivity and conductivity,

$$\sigma_i = D_i \frac{\chi_i (z_i F)^2}{RT} \tag{2.15}$$

the flux of a charged species i is then defined in terms of its chemical and electrical driving forces as,

$$J_i = -\frac{\sigma_i}{(z_i F)^2}\left(\frac{RT}{\chi_i}\frac{\partial \chi_i}{\partial x} - z_i F \frac{\partial \phi_i}{\partial x}\right) \tag{2.16}$$

The motion of a charged species constitutes a current, described mathematically as the product of the charge z, Faradays constant and the flux of each respective species,

$$i_i = z_i F J_i \tag{2.17}$$

More specifically, this equation may be used to calculate the theoretical hydrogen flux density during galvanic operation,

$$J_H = \frac{i}{nFA} \tag{2.18}$$

and will be used later to compare the theoretically predicted flux to experimental results obtained in this work.

2.3 The Electrode Reaction Kinetics of Hydrogen Oxidation

The hydrogen oxidation reaction (HOR) is fundamental to the operation of many electrochemical devices, and is thought to occur primarily in a small region at the three phase boundary (3pb) of the gas-metal-electrolyte interface. It is also hypothesized that in the case of an electrode material with high hydrogen permeability, such as Pd or a Cu-Pd alloy [82, 83], this may also occur at the two-phase metal-electrolyte boundary (2pb). Fig. 2.3 schematically depicts the possible reaction pathways to each of these regions, collectively referred to as the phase boundary, (pb).

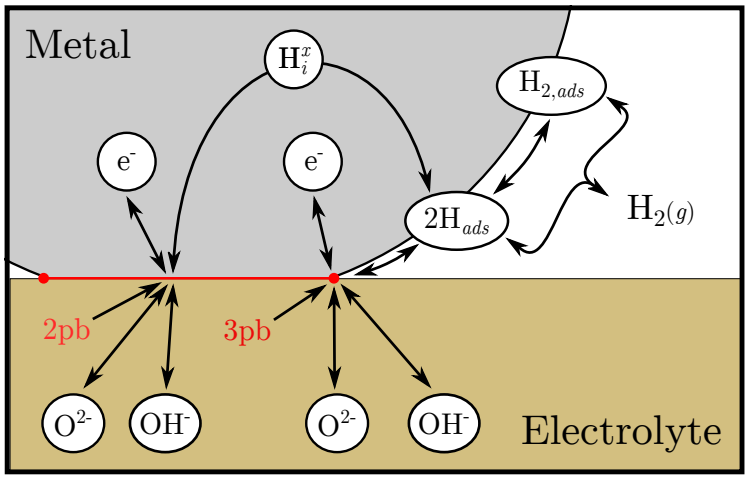

Figure 2.3: Possible reaction paths at the metal-electrolyte interface of proton conducting BZCY72, showing hydrogen gas associatively adsorbing ($H_{2,ads}$) and subsequently dissociating, or dissociatively adsorbing ($2H_{ads}$). This is followed by interstitial (H_i^x) and surface diffusion to the pb, where the electron transfers to the metal, and the proton transfers to an oxide ion (O^{2-}) in the electrolyte, resulting in the hydroxide defect (OH^-).

As illustrated, this elementary reaction sequence can be described first by the adsorption of hydrogen gas onto a vacant adsorption site (v_{ads}) on the surface of the electrode as follows,

$$1 \text{ - adsorption: } H_2(g) + v_{ads} \Longleftrightarrow H_{2,ads} \tag{2.19}$$

$$2 \text{ - dissociation: } H_{2,ads} + v_{ads} \Longleftrightarrow 2H_{ads} \tag{2.20}$$

If a molecule adsorbs associatively, the dissociation step is given in (2.20), or for dissociative adsorption the second order process is given by the sum of (2.19) and (2.20). Diffusion to the pb will occur either on the surface of the electrode to the 3pb and/or intersitially through the bulk electrode to the 2pb. This will progress as,

$$\text{3a - surface diffusion: } \mathrm{H}_{ads} + v_{3pb} \Longleftrightarrow \mathrm{H}_{3pb} + v_{ads} \tag{2.21}$$

$$\text{3b - } \begin{cases} \text{dissolution into metal: } \mathrm{H}_{ads} + v_i \Longleftrightarrow \mathrm{H}_i^x + v_{ads} \\ \text{interstitial diffusion: } \mathrm{H}_i^x + v_{2pb} \Longleftrightarrow \mathrm{H}_{2pb} + v_i \end{cases} \tag{2.22}$$

The charge transfer reaction at the pb involves the simultaneous dissociation of neutral atomic hydrogen and proton transfer to an available oxide ion in the electrolyte, with electron transfer to the electron cloud of the bulk metal. In transition state theory this is known as proton coupled electron transfer, and has been widely studied in numerous electrochemical and bio-electrochemical systems. Here, this process can be described by proton transfer to an available oxide ion in the electrolyte, forming the hydroxide species, and electron transfer to the electronically conducting phase of the electrode.

$$\text{4 - charge transfer: } \mathrm{H}_{pb} + \mathrm{O}_{\mathrm{O}}^{2-} \Longleftrightarrow \mathrm{OH}_{\mathrm{O}}^{-} + e^- + v_{pb} \tag{2.23}$$

Overall, this simplistic model may be complicated by the presence of other gaseous species, such as water vapor, through competitive adsorption at preferential sites. Additionally, both gas phase diffusion and interstitial diffusion will also be neglected in the following treatment. The following sections deal with simplifying assumptions applied to the mass and charge transfer processes, and then relates them to quanifiable characteristics of the total polarization response as measured by impedance spectroscopy.

Mass transfer: adsorption, dissociation and diffusion

The interaction of H_2 with metal surfaces has been studied in great detail for many decades, and despite the wealth of knowledge generated, there is no definitive formulation about H_2-metal surface dynamics [84–86]. H_2 is the smallest diatomic molecule and readily adsorbs on metal surfaces. For noble metals such as Cu, Ag and Au, adsorption is activated, while for many others, such as Ni, Pd and Pt, adsorption is non-activated [86–88].

The decisive factor for the adsorption process is the sticking probability, which determines whether a particle will stay on the metal surface or be reflected. Initial sticking probabilities vary for different metals and for different crystallographic orientations ($<$ 0.1 for all Cu surfaces, up to 0.4 for Pt, 0.65 for W, 0.7 for Pd, and 0.96 for Ni), but in general it is inversely proportional to the surface coverage [53]. If H_2 sticks to the surface and becomes physisorbed in a precursor state, the availability of a neighboring vacant chemisorption site will determine if it moves into the transition state. When there is a vacant site available and the activation energy barrier is overcome, the H-H bond is broken and it becomes chemisorbed on the metal surface. Fig. 2.4 shows this

process in a characteristic Lennard-Jones potential energy diagram for the adsorption of H_2 on Cu metal, adapted from [52, 53, 89–91]. First, hydrogen gas is shown approach-

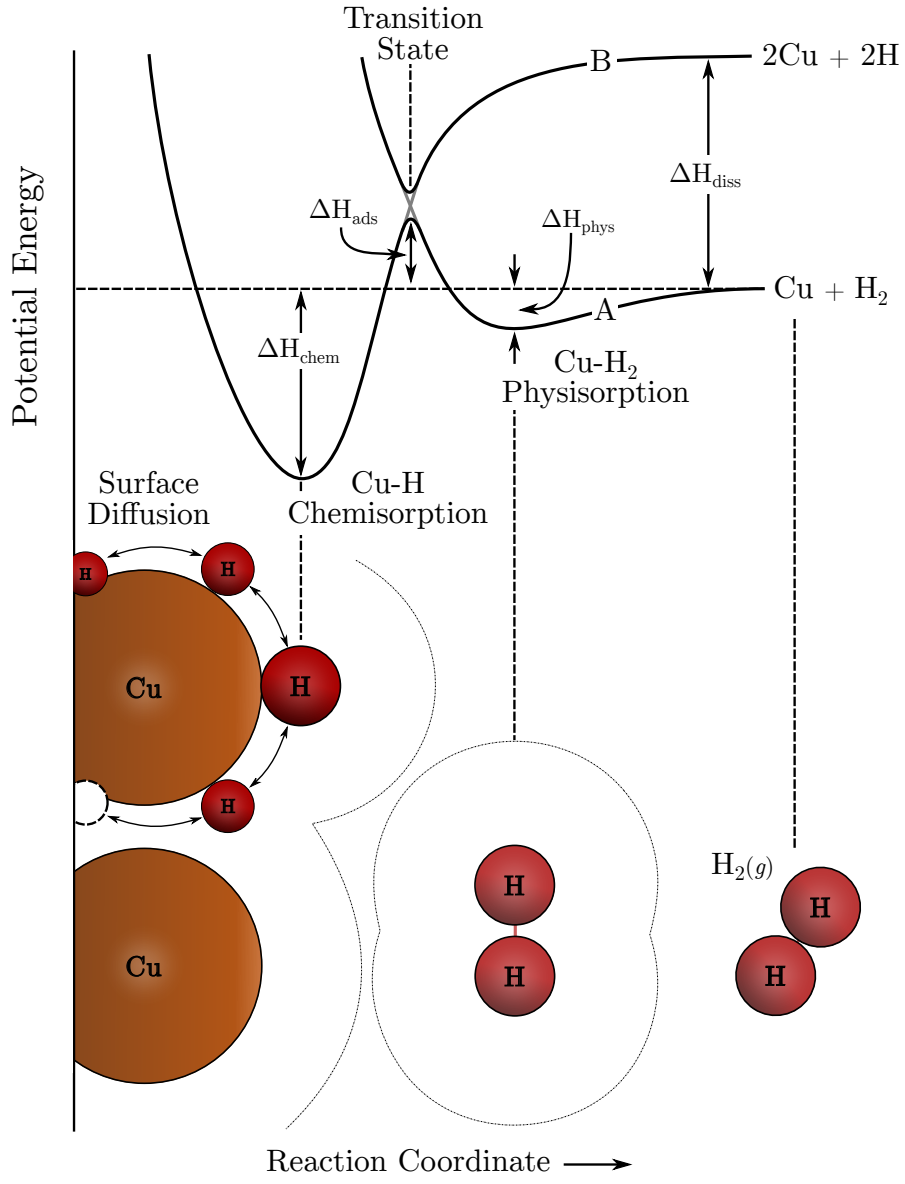

Figure 2.4: Schematic depiction of the potential energy landscape for mass transport to the 3pb using a Lennard-Jones potential energy curve for the Cu-H system. Curve A refers to the physisorption of molecular hydrogen, and curve B refers to the chemisorption of atomic hydrogen. The reaction coordinate represents increasing distance from the metal-electrolyte interface. Adapted from [52, 53, 89–91]

ing the Cu metal surface, attracted by the van der Waal force. It is then physisorbed in the precursor state, and aside from lateral interactions it is free to move across the surface of the metal [53]. Cu and other noble metals have an activated transition state

for chemisorption, such as shown in Fig. 2.4, however, for other metals such as Pt and Ni, this transition state lies below the horizontal axis, and dissociative chemisorption is non-activated.

Adsorption is largely dependent on site availability, and is inversely proportional to the surface coverage. This emphasizes surface coverage, (Θ_{ads}), as the figure of merit for the adsorption process. Langmuir first considered this process in terms of equilibrium thermodynamics, where the rates of adsorption and desorption are equal,

$$p\mathrm{H}_2\, k^+ (1 - \Theta_{ads})^x = k^- \Theta_{ads}^x \tag{2.24}$$

Here, surface coverage is equivalent to activity, and the activity of vacant sites is then $(1 - \Theta)$, with k^+ and k^- the forward and reverse rate constants, respectively. For associative adsorption, $x = 1$, and for dissociative adsorption, $x = 2$. The equilibrium constant for Eq. 2.24 is,

$$\mathbf{K}_{ads} = \frac{k^+}{k^-} = \frac{\Theta_{ads}^x}{(1 - \Theta_{ads})^x\, p\mathrm{H}_2} \tag{2.25}$$

From this, the limiting cases of the Langmuir adsorption isotherm are derived [52]. At low coverage, $\Theta_{ads} \ll$, and with the activity of vacant sites close to unity, the surface coverage is approximated by,

$$\Theta_{ads} \approx (\mathbf{K}_{ads}\, p\mathrm{H}_2)^{1/x} \tag{2.26}$$

At high coverage, $\Theta_{ads} \approx 1$, and the activity of vacant sites is approximated by,

$$(1 - \Theta_{ads}) \approx \frac{1}{(\mathbf{K}_{ads}\, p\mathrm{H}_2)^{1/x}} \tag{2.27}$$

For intermediate coverages there is no simple approximation, and a complex dependency results,

$$\Theta_{ads} = \left(\frac{\mathbf{K}_{ads}\, p\mathrm{H}_2}{1 + \mathbf{K}_{ads}\, p\mathrm{H}_2} \right)^{1/x} \tag{2.28}$$

The intermediate coverage is dependent on both the hydrogen pressure and equilibrium rate constant.

At thermodynamic equilibrium the net rate is 0, and from (2.24), with the adsorption rate constant $\mathbf{K}_{ads} = \sqrt[x]{(k_1^+/k_1^-)}$, the surface coverage of H or H_2 is,

$$\Theta_{ads}^{H_{2/x}} = \mathbf{K}_{ads}\, p\mathrm{H}_2^{1/x}(1 - \Theta_{ads}) \tag{2.29}$$

The equilibrium constant, $\mathbf{K}_{ads}$, contains parameters such as the sticking coefficient,

s_0, which is related to the catalytic activity of the metal surface. The catalytic activity of a metal surface has direct implications on the dynamics of the H_2-metal interaction, and has been attributed to geometric factors such as crystallographic orientation and surface inhomogeneities, as well as to electronic factors such as defect induced potentials, work functions and the density of states at the Fermi level [92–96].

$$\mathbf{K}_{ads} = \frac{s_0}{\nu(\Theta_{sat})^2\sqrt{2\pi mkT}}\,\mathbf{e}^{-\frac{\Delta H_{ads}}{kT}} \tag{2.30}$$

After adsorption and dissociation, diffusion to the phase boundary occurs via two paths, on the surface of the Cu electrode, and interstitially through the bulk Cu lattice, though for simplicity, only surface diffusion to the 3pb will be considered. On the electrode surface, diffusion takes place in successive jumps of the adsorbed molecular or atomic H from occupied adsorption sites to adjacent unoccupied sites. In contrast to the Nernst-Planck equation for charged species, this process can be adequately described by Ficks law,

$$J_H = -D_H\,\frac{\partial\Theta}{\partial x} \tag{2.31}$$

Where D_H is the diffusion coefficient, and the driving force is the gradient in the surface coverage of the adsorbed species, given by the difference between adsorbed hydrogen at the 3pb and on the electrode surface adjacent to the 3pb,

$$\frac{\partial\Theta}{\partial x} = \frac{\Theta^H_{3pb} - \Theta^{H_{2/x}}_{ads}}{\Delta x} \tag{2.32}$$

At equilibrium, there is no net flux, but the two coverage terms are not identical. Metals that have a high catalytic activity towards hydrogen dissociation will have a higher coverage at the phase boundary. There, the hydrogen will have already dissociated, existing as atomic hydrogen in order for the charge transfer process to take place. The hydrogen coverage at the 3pb is then given by,

$$\Theta^H_{3pb} = \mathbf{K}_{mt}\,p\mathrm{H}_2^{1/2}(1 - \Theta_{3pb}) \tag{2.33}$$

Here, the rate constants of the adsorption, dissociation and diffusion processes are referred to collectively at $\mathbf{K}_{mt}$. Once at the 3pb, the adsorbed hydrogen is then in dynamic equilibrium with the activity of protons in the electrolyte and electrons in the metal, and though there is no net exchange of charge, there is still an equilibrium charge transfer process taking place. The coverage of adsorbed hydrogen at the 3pb is then equivalent to the activity or concentration of the reduced species, $[C_R]$, which is

oxidized during the charge transfer reaction; as detailed in the next section.

Butler-Volmer theory

Charge transfer reactions have been described using the Butler-Volmer equation with much success by countless researchers. First, consider the kinetics of a generalized charge transfer reaction taking place at the electrode-electrolyte phase boundary, where a reduced species, R, such as hydrogen, is oxidized,

$$R \Leftrightarrow Ox + e^- \tag{2.34}$$

Electrochemical reactions are most fundamentally characterized by current, which at any potential, is a direct measure of the electron transfer rate [97].

$$r = \frac{i}{nFA} \tag{2.35}$$

The rate equation for the oxidation shown in (2.34) is,

$$r = [C_R]k^+ - [C_{Ox}]k^- \tag{2.36}$$

where the concentrations, $[C_i]$, are equivalent to the activities, $a_i/a_{0,i}$ of the respective reduced and oxidized species. The forward and backward rate constants are of Arrhenius form,

$$k^+ = k_0^+ \mathbf{e}^{\beta n\zeta E} \quad \text{and} \quad k^- = k_0^- \mathbf{e}^{-(1-\beta)n\zeta E} \tag{2.37}$$

Here, E is the electrode potential, and $\zeta = F/RT$, where F, R and T have their usual meaning. The symmetry coefficient, β describes the relative magnitudes of the forward and reverse energy barriers for the activated transition state [54]. Although the symmetry coefficient can in principle have any value between 0 and 1, depending upon the concentration gradient of electroactive species and the type of metal catalyst employed, it is typically near 0.5, and is often assumed to be independent of temperature and potential.

At the standard electrode potential, E_0, the concentration terms in (2.36) are at unit activity, then the net current is 0 and the forward and backward rate constants are equal [97],

$$k_0 = k_0^+ \, \mathbf{e}^{\beta n\zeta E_0} = k_0^- \, \mathbf{e}^{-(1-\beta)n\zeta E_0} \tag{2.38}$$

By defining the overpotential as the difference between the electrode and standard electrode potentials, $\eta = E - E_0$, and solving for k_0^+ and k_0^- in terms of k_0, the heterogeneous

rate constant,

$$k_0^+ = k_0\,\mathbf{e}^{-\beta n\zeta\eta} \quad \text{and} \quad k_0^- = k_0\,\mathbf{e}^{(1-\beta)n\zeta\eta} \tag{2.39}$$

Then substituting the relations from (2.39) into (2.37) and (2.36), the potential dependence of the electron transfer rate is given by,

$$r = k_0\left([C_R]\,\mathbf{e}^{\beta n\zeta\eta} - [C_{Ox}]\,\mathbf{e}^{-(1-\beta)n\zeta\eta}\right) \tag{2.40}$$

At the equilibrium potential there is no net current and the forward and reverse reaction rates are equal, however, the concentration terms are not unity. Through the current-rate equality of (2.35), this difference in concentration gives rise to the exchange current, i_0,

$$i_0 = nFAk_0\,[C_R]\,\mathbf{e}^{\beta n\zeta(E_{eq}-E_0)} = nFAk_0\,[C_{Ox}]\,\mathbf{e}^{-(1-\beta)n\zeta(E_{eq}-E_0)} \tag{2.41}$$

Dynamic equilibrium at the metal-adsorbate-electrolyte interface equates the electrochemical potentials of the three mediums,

$$\tilde{\mu}_i = \mu_i^0 + RT\ln([C_i]) + zF\phi_i \tag{2.42}$$

where μ_i^0 is the standard chemical potential, z is charge and ϕ_i is the electrostatic potential of species i. Similar to other derivations of the hydrogen electrode potential [54, 55], the equilibrium expression for the electrochemical potential of charge transfer, (2.23), at the 3pb, then becomes,

$$\mu^0_{[C_R]} + RT\ln([C_R]) = \mu^0_{[C_{Ox}]} + RT\ln([C_{Ox}]) + F\phi_{[C_{Ox}]} - F\phi_{e^-} \tag{2.43}$$

Separating terms and defining the Galvani interfacial and standard state potentials as,

$$\Delta\phi = \phi_{e^-} - \phi_{[C_{Ox}]} \quad \text{and} \quad \Delta\phi^0 = \frac{\mu^0_{[C_R]} - \mu^0_{[C_{Ox}]}}{F} \tag{2.44}$$

the equilibrium potential of the hydrogen electrode is,

$$\Delta\phi - \Delta\phi^0 = E_{eq} - E^0 = \frac{1}{\zeta}\ln\left(\frac{[C_{Ox}]}{[C_R]}\right) \tag{2.45}$$

Then inserting the above 3pb equilibrium potential, (2.45), into the expression for the exchange current, (2.41),

$$i_0 = nFAk_0\,[C_R]\,\mathbf{e}^{\beta n\zeta(\frac{1}{\zeta}\ln([C_{Ox}]/[C_R]))} = nFAk_0\,[C_{Ox}]\,\mathbf{e}^{-(1-\beta)n\zeta\left(\frac{1}{\zeta}\ln([C_{Ox}]/[C_R])\right)} \tag{2.46}$$

and simplifying, the exchange current is,

$$i_0 = nFAk_0 \left[C_R\right]^{(1-\beta)} \left[C_{Ox}\right]^{\beta} \tag{2.47}$$

By inserting (2.47) into (2.40), with $\eta = E_{eq} - E_0$, the most common form of the Butler-Volmer equation is obtained,

$$i = i_0 \left(\mathbf{e}^{\beta n\zeta\eta} - \mathbf{e}^{-(1-\beta)n\zeta\eta}\right) \tag{2.48}$$

If $\beta n\zeta\eta \ll 1$ and $-(1-\beta)n\zeta\eta \ll 1$, then the Taylor series expansion is approximated by the first two terms, i.e., for small x, $\mathbf{e}^x = 1 + x$, and this yields the Ohm's law−like relation for the exchange current and charge transfer resistance,

$$i = i_0 n\zeta\eta \;\; \rightarrow \;\; i_0 = \frac{1}{(n\zeta)}\frac{i}{\eta} = \frac{1}{(n\zeta)}\frac{1}{R_{ct}} = nFAk_0 \left[C_R\right]^{(1-\beta)} \left[C_{Ox}\right]^{\beta} \tag{2.49}$$

With $n = 1$, $C_R = \Theta_{3pb}^{H} \left[O_O^{2-}\right]$, Θ_{3pb} from (2.33), and $C_P = \left[OH_O^{-}\right](1 - \Theta_{3pb})$,

$$i_0 = \frac{1}{\zeta}\frac{1}{R_{ct}} = FAk_0 \left(\mathbf{K}_{mt}\, p\mathrm{H}_2^{1/2}(1 - \Theta_{3pb})[O_O^{2-}]\right)^{(1-\beta)} \left(\left[OH_O^{-}\right](1 - \Theta_{3pb})\right)^{\beta} \tag{2.50}$$

which with the concentrations of $[O_O^{2-}] \approx 1$ and $[OH_O^{-}] \ll$ and constant, and by incorporating the other constants (ζ, F, A, k_0 and $\mathbf{K}_{mt}$) into $\mathbf{K}_{ct}$, simplifies to,

$$\frac{1}{R_{ct}} = \mathbf{K}_{ct}\, pH_2^{\frac{1-\beta}{2}}(1 - \Theta_{3pb}) \tag{2.51}$$

Then the inverse charge transfer resistance (conductance) is proportional to the product of the rate constant, $\mathbf{K}_{ct}$, the symmetry coefficient scaled $p\mathrm{H}_2$ dependency derived from mass transfer, and the activity of vacant adsorption sites at the 3pb, $(1 - \Theta_{3pb})$.

The total polarization resistance

Though the thermodynamics of hydrogen adsorption and dissociation are entirely chemical in nature, they are inherently coupled with the factors affecting electrode reaction rates and the resulting electrochemical current [56]. At steady state, such as characterized by impedance spectroscopy at low frequencies, charge transfer is slowed by coupled mass transfer processes. The rates of charge transfer and mass transfer are then the same, and the magnitude of the current is dependent upon the rate limiting step. The reaction sequence comprises the total polarization resistance as the sum of the mass and charge transfer processes. (The following treatment is adapted from Bard

and Faulkner, "Electrochemical Methods", pp. 23-34 [56].) To clarify the nature of the total polarization response, consider these anodic process represented as an electrical circuit, as shown in Fig. 2.5, where the gas phase diffusion resistance would precede mass

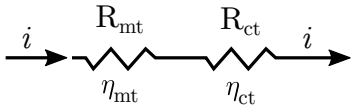

Figure 2.5: The electrode polarization resistance, composed of reaction the processes of mass and charge transfer, represented as an electrical circuit. Adapted from [56]

transfer, and charge transfer is followed by the electrolyte resistance and the cathodic branch. The sum of these terms gives rise to the measured polarization resistance, which can be mathematically elucidated through the Butler-Volmer equation by incorporating mass transfer terms. When conducting investigations using impedance spectroscopy, an alternating current oscillates between positive and negative values of the specified amplitude, and thus periodically alters the concentrations of reactants at the metal-electrolyte interface. In this case, the coverage at the 3pb (Θ^{H}_{3pb}) is either more or less than the coverage on the overall electrode surface ($\Theta^{H_{2/x}}_{ads}$) and the net rate of mass transport to the 3pb is given by (2.31) and (2.32) [56],

$$r_{mt} = \frac{i}{nFA} = -D_H \frac{\Theta^{H}_{3pb} - \Theta^{H_{2/x}}_{ads}}{\Delta x} \tag{2.52}$$

For convenience, the mass transfer coefficient is now defined as $m_\Theta = {}^{D_H}/_{\Delta x}$ (in units of $\mathrm{cm}^3\ \mathrm{s}^{-1}\ \mathrm{cm}^{-2}$), then (2.52) is rewritten as,

$$\frac{i}{nFA} = m_\Theta(\Theta^{H_{2/x}}_{ads} - \Theta^{H}_{3pb}) \tag{2.53}$$

Next, consider that at the instantaneous maximum positive AC amplitude, the largest rate of mass transfer occurs such that $\Theta^{H}_{3pb} \ll$ and may be neglected,

$$\frac{i}{nFA} = m_\Theta(\Theta^{H_{2/x}}_{ads}) \tag{2.54}$$

then the anodic limiting current is then obtained,

$$i_{\ell,a} = nFA\, m_\Theta \Theta^{H_{2/x}}_{ads} \tag{2.55}$$

By substituting (2.55) into (2.53) the expression for Θ^{H}_{3pb} is,

$$\Theta^{H}_{3pb} = \Theta^{H_{2/x}}_{ads}\left(1 - \frac{i}{i_{\ell,a}}\right) \tag{2.56}$$

Using (2.45) with the previous definitions of C_R and C_P, and the concentrations of $[O^{2-}_{O}]$, $(1 - \Theta_{3pb})$ and $[OH^{-}_{O}]$,

$$E = E^0 + \frac{1}{\zeta}\ln\left(\frac{1}{\Theta^{H}_{3pb}}\right) \quad \Rightarrow \quad E - E^0 = \frac{1}{\zeta}\ln\left(\Theta^{H_{2/x}}_{ads}\right) + \frac{1}{\zeta}\ln\left(1 - \frac{i}{i_{\ell,a}}\right) \tag{2.57}$$

Here $\Theta^{H}_{ads} \gg \Theta^{H}_{3pb}$ and thus is neglected as $\lim(\ln[\Theta^{H}_{ads}])_{\Theta^{H}_{ads}\to 1} = 0$, then

$$E - E^0 = \frac{1}{\zeta}\ln\left(1 - \frac{i}{i_{\ell,a}}\right) \tag{2.58}$$

then by defining the concentration overpotential as $\eta_{conc} = E - E^0$,

$$\eta_{conc} = \frac{1}{\zeta}\ln\left(1 - \frac{i}{i_{\ell,a}}\right) \tag{2.59}$$

Where upon exponentiating the terms, and once again with $\mathbf{e}^x = 1 + x$ for small x,

$$1 - \frac{i}{i_{\ell,a}} = \mathbf{e}^{-\zeta\eta_{conc}} \Rightarrow 1 - \zeta\eta_{conc} \tag{2.60}$$

Then through further simplifications, the Ohm's law-like relationship is obtained for the limiting current and inverse mass transfer resistance. For small deviations of the potential E from E_{eq}, the i-η_{conc} characteristics are linear, and with units of resistance (Ω), we may define a "small signal" mass transfer resistance as [56],

$$\frac{i}{\eta_{conc}} = \zeta i_{\ell,a} = \frac{1}{R_{mt}} = \mathbf{K}_{ads}\, p\mathrm{H}_2^{1/x}(1 - \Theta_{ads}) \tag{2.61}$$

It is proposed that this relationship may be extended to the exchange current, as when performing impedance spectroscopy, the mass transfer response is observed at very low frequencies which may constitute a "small signal" response. Thereby, the measured total resistance at DC, R_p, is the sum of R_{ct} and R_{mt}.

Temperature dependencies

In the preceding sections, equations (2.51) and (2.61) were derived to describe the $p\mathrm{H}_2$ dependencies of the charge and mass transfer conductances. Temperature dependencies, such as seen in Eq. 2.30 and in $\zeta = F/RT$, were incorporated into the rate constants $\mathbf{K}_{mt}$ and $\mathbf{K}_{ct}$. Fig. 2.6 shows a characteristic surface that combines the $p\mathrm{H}_2$ and temperature dependencies of the inverse charge transfer resistance, and emphasizes that electrode reaction kinetics are strong functions of temperature. The general equa-

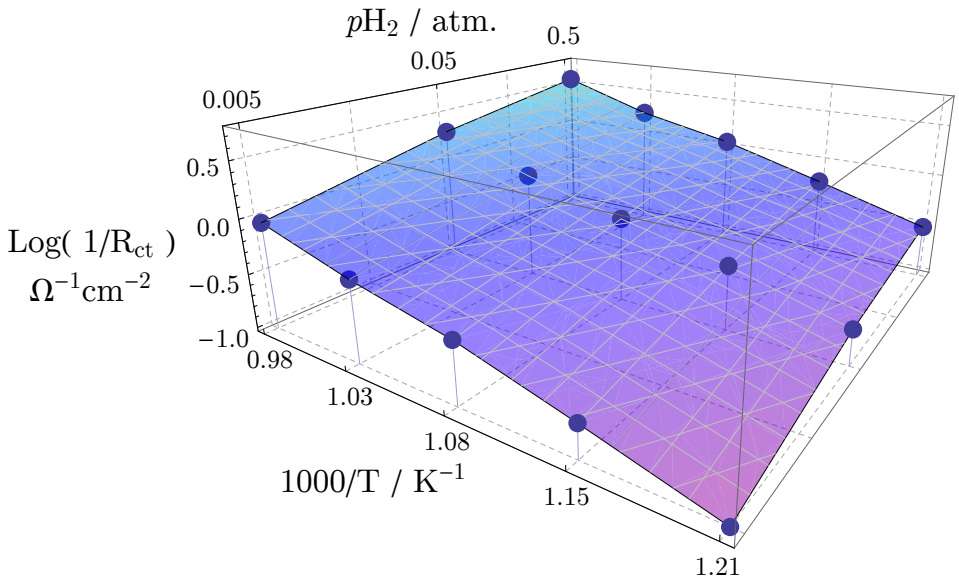

Figure 2.6: Charge transfer conductance, as obtained for a Cu-Co infiltrated backbone electrode, plotted as a function of both the $p\mathrm{H}_2$ and inverse temperature.

tion for thermally activated electrode reaction kinetics is of Arrhenius form, and must also be expressed as a function of the concentrations of reactants and their respective reaction orders [55, 56, 98]. It is proposed, based on empirical results obtained through impedance spectroscopy, that the charge and mass transfer conductances can, to a first approximation, be expressed as,

$$\frac{1}{R} = A_0 \left(pH_2\right)^n \left(pH_2O\right)^m \mathbf{e}^{-\frac{\Delta H}{k_b T}} \tag{2.62}$$

where k_b is Boltzman's constant and A_0 is the pre-exponential factor. Most thermally activated parameters are included in the activation enthalpies, which are beneficial in identifying reaction mechanisms and the rate limiting process. However, both the $p\mathrm{H}_2$ and $p\mathrm{H}_2\mathrm{O}$ dependencies, n and m, as well as the rate constants and some material properties, likely have a small temperature dependency.

Charge transfer pre-exponential

The charge transfer pre-exponential, $A_{0,ct}$, is often under-reported, and is a parameter representative of material specific properties such as the interfacial resistivity, as well as geometric factors. Numerous attempts have been made to try and determine an analytic relationship between the charge transfer resistance and geometric aspects of the three phase boundary region [99–103]. The 3pb region has been recognized to exist with finite dimensions, rather than as a singularity, having an effective width, ω, and thickness, δ, possibly such as shown in Fig. 2.7, The dimension δ is likely on the order

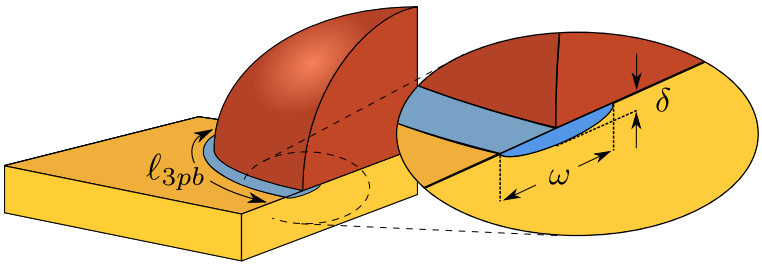

Figure 2.7: Possible geometry of the 3pb at the metal-electrolyte interface, with length ℓ_{3pb}, width ω and thickness δ.

of angstroms, while ω, as a function of bias, is thought to be on the orders of angstroms to microns, thus these lengths are not easily measurable [102–105]. The most relevant and widely sought geometric factor is the 3pb length, ℓ_{3pb}, often reported in length per unit area for the planar metal-electrolyte interface [102, 104]. In terms of the material specific charge transfer resistivity of the 3pb gas-electrode-electrolyte interface, ρ'_{ct} (with units of $\Omega\,\mathrm{cm}$), the inverse charge transfer resistance is,

$$\frac{1}{R_{ct}} = \frac{\omega\,\ell_{3pb}}{\rho'_{ct}\,\delta} \tag{2.63}$$

The thickness, δ, is the dimension across which charge transfer occurs, through the area defined by the width, ω, and 3pb length, ℓ_{3pb}. However, because the parameters ω and δ are somewhat obscure, it is useful to define the 3pb geometric resistivity as,

$$\rho_{ct} = \frac{\rho'_{ct}\delta}{\omega} \tag{2.64}$$

and then the inverse of the measured charge transfer resistance becomes,

$$\frac{1}{R_{ct}} = \frac{\ell_{3pb}}{\rho_{ct}} \tag{2.65}$$

Eq. (2.65) states that the charge transfer conductivity of the metal-electrolyte interface is inversely proportional to the 3pb geometric resistivity, and will increase with the length of the 3pb. This equation mathematically illustrates why small electrodes such as point-contacts have high resistances, while electrodes with extended 3pb lengths, such as Ni-cermets as state of the art electrodes, have low resistances.

By comparing (2.62) and (2.65), it is seen that with temperature, $p\mathrm{H}_2$ and $p\mathrm{H}_2\mathrm{O}$ independence, A_0 is directly proportional to ℓ_{3pb}, and inversely proportional to the geometric resistivity, ρ_{ct},

$$A_0 \propto \frac{\ell_{3pb}}{\rho_{ct}} \propto \frac{\omega\,\ell_{3pb}}{\rho'_{ct}\,\delta} \tag{2.66}$$

It is proposed that if ℓ_{3pb} is known or can be estimated, then the corresponding charge transfer pre-exponential can be compared to the A_0 of another electrode with similar composition, and used to estimate the unknown ℓ_{3pb}.

It is reasonable to assume that the three phase boundary length, ℓ_{3pb}, is constant with bias. Eq. (2.66) then implies that variations in A_0 with bias are likely due to changes in the dimensions ω and δ, or possibly in the resistivity ρ'_{ct}. The parameter δ is thought to be related to the concentration of protons in the outermost atomic layers of the electrolyte, and thus to any bias dependent electrode-electrolyte space charge layer that may exist. The effective width of the 3pb, ω, also has potential variability, and has been modelled as a function of bias by O'Hayre et al. [104].

The material specific geometric resistivity describes the electronic structure of the unique metal-electrolyte interface, and may be thought of in terms of the Fermi level alignment between the metal and the oxide, and as such is also possibly a function of bias [106]. In simpler terms, ρ_{ct} defines the resistivity to the charge transfer process: the coupled proton-electron delocalization with simultaneous proton transfer to an oxide ion in the electrolyte, and electron transfer to the metal. It is a parameter that is also likely to be temperature dependent, as with increasing temperature electrical resistivity increases, and ionic resistivity decreases. Hence, these interfacial material specific and dimensional parameters are all functions of bias, and may offer explanations for the increases in the charge transfer pre-exponential, A_0, as well as the associated activation enthalpies.

3 Synthesis

3.1 Electrolytes

The electrode studies in this thesis were performed using dense BZCY72 electrolyte pellets, as well as tubular 65 wt% Ni-BZCY72 cermet-electrode supported membranes.

Electrolyte pellets were fabricated from both commercial BZCY72 nanopowder (Cerpotech AS) and reactive-sintered precursor oxide powders such as BaO, ZrO_2, CeO_2 and Y_2O_3 (Sigma-Aldrich, Alfa Aesar). The powders were first mixed in a planetary ball mill with 1 wt% binder, either polyvinylpyrrolidone (PVP) or polyvinylbuterol (PVB), and a sintering aid, such as 1 wt% ZnO or 0.5 to 1.0 wt% NiO. After the powders were dried, pellets were uniaxially pressed in a 25 mm die, typically to a pressure of 3 tons. The firing profile was varied depending upon both the starting powders and the type of sintering aid used, if any. After sintering, the resultant pellets were nominally of greater than 95% of the theoretical density of BZCY72.

The 65 wt% Ni-BZCY72 cermet electrode supported tubes were obtained in both the pre-sintered and green-bodied forms (Coors Tek Inc, Golden, CO. USA, and CMS, Oslo, Norway). The support tubes obtained from the USA were fabricated by slip casting, while the ones received from Norway were made by extrusion. After production of the green bodied support tubes, the BZCY72 membrane precursors were applied via atomizing spray coating. Further details specific to this process have been described in previous literature and will not be elaborated upon further here [29, 107, 108].

3.2 Backbone Microstructures

Ni-cermet electrodes are widely acknowledged to be the best hydrogen anodes due to the longer tpb length of the metal-electrolyte interface and the catalytic activity of Ni metal towards the HOR. As an extension of the electrolyte, the ceramic phase of the multi-phase cermet composition plays multiple roles. Aside from being the mechanically supporting architecture, it is also the ionic phase of the charge transfer interface. When independent from the metal phase, it has often been referred to as the "backbone" of a cermet electrode. Many researchers have utilized such microstructures to develop electrodes that would not otherwise survive at the high sintering temperatures of materials such as Ni-BZCY cermets. This has been accomplished by introducing different compositions into the backbone through methods such as infiltration and electrodeposition. Despite all of these efforts, there is not much detail in existing literature as to what the optimal backbone consists of. On one hand, a small grained microstructure provides a large surface area, but comes with a higher number of grain boundaries and is less mechanically robust. The effective thickness of the backbone would then be diminished

due to a higher total grain boundary resistance, resulting in diminished performance. Alternatively, a backbone consisting of much larger grains and fewer grain boundaries will be more mechanically robust and have a lower total grain boundary resistance, but will also have a significantly smaller surface area. Numerous backbones were developed during the course of the research performed for this thesis, and due to the variability of the different electrolytes required as many different backbone synthesis procedures. However, no experiments were performed explicitly aimed at examining the performance characteristics of microstructure variation.

Example morphologies

Three examples of some of the backbone morphologies produced in this work are presented in Fig. 3.1, with a brief description of their synthesis is provided below.

A) The backbone shown in Fig. 3.1A was produced from commercial BZCY72 nanopowder (Cerpotech AS, Trondhiem, NO) calcined at 1000 °C for 12 h. The calcined powder was mixed with 50 wt.% graphite, yielding a calculated porosity of approximately 70%. Using a pre-sintered electrolyte pellet of the same composition but containing 1 wt% ZnO sintering aid, it was fired at 1500 °C for 4 h. The average grain size of the resulting microstructure was sub-μm, and though it was well sintered to the electrolyte, it was fragile and not mechanically robust.

B) The backbone shown in Fig. 3.1B was fabricated from BZY15 precursor oxides and was co-sintered with the electrolyte. Precursor BZY15 powders containing 0.25 wt% NiO were calcined at 1525 °C for 12 h. Then 1.5 g of the calcined powder and 0.5 g of the 0.25 wt% NiO precursors were then mixed in the planetary mill with 4 g of graphite; this composition was then made into an ink. Four coats of the backbone ink were painted onto symmetric areas of a pellet pressed from precursor oxides and dried at 50 °C for 30 min between coats. The coated pellet was then sintered at 1625 °C for 8 h, producing the observed microstructure with grain sizes up to 2.5 μm in diameter.

C) The SEM images in Fig. 3.1C show a backbone that was co-sintered onto green-bodied membrane coated NiO-cermet electrode supported tube, obtained pre-coated from CMS AS. The same backbone ink synthesis as above was used here, however the precursors were first calcined at 1650 °C. This firing profile varied considerably from that used for other backbones. The high temperature dwell was modified due to the formation of the Ni-eutectic phase, and the cooling phase also necessitated a different approach due the thermal expansion mismatch between

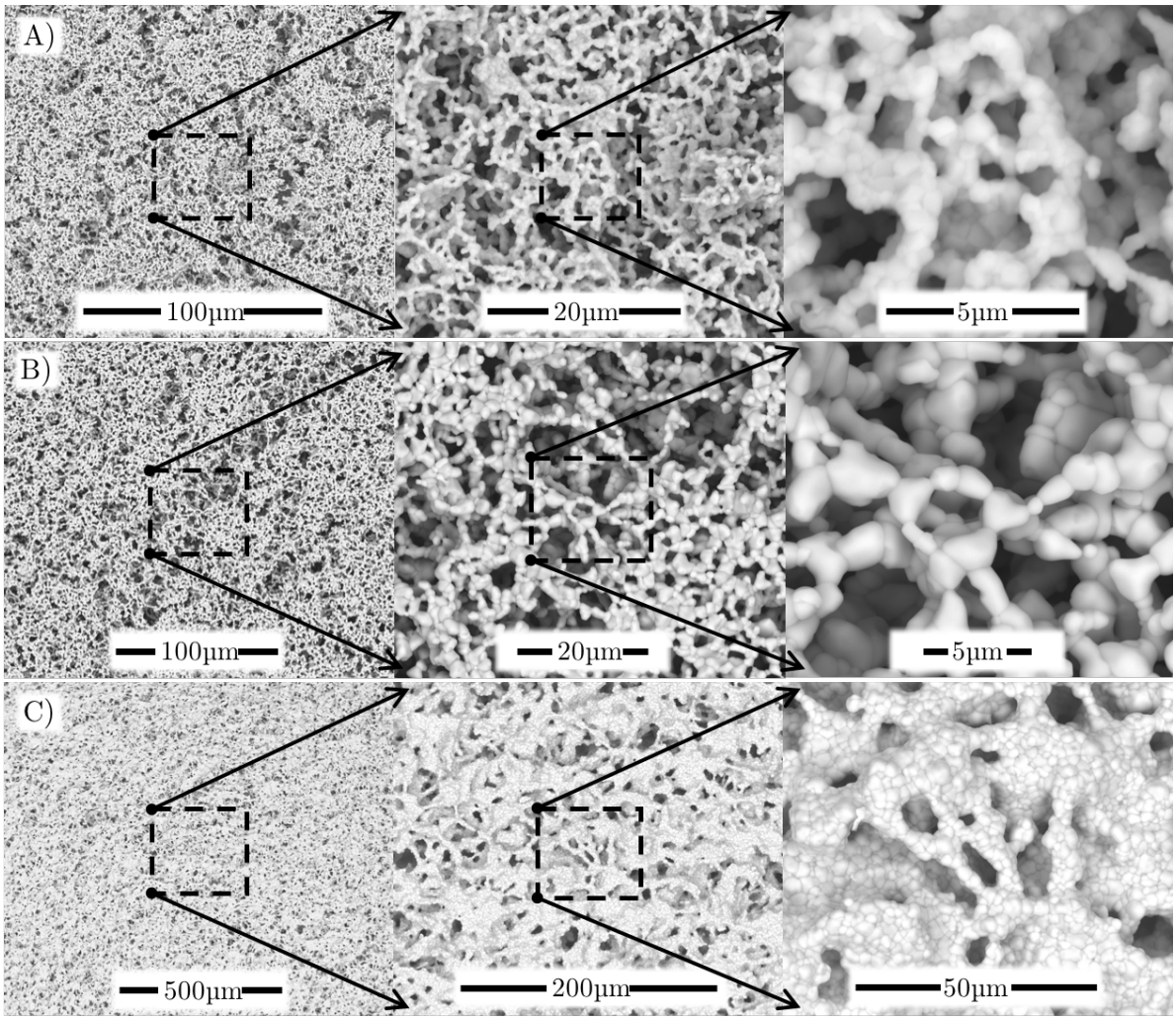

Figure 3.1: Backbone microstructures: A) BZCY72 Cerpotech based backbone, B) BZY15 precursor based co-sintered backbone, C) BZCY72 precursor based backbone co-sintered on a tubular 65 wt% NiO-BZCY72 cermet electrode supported electrolyte.

BZCY72 and the NiO-cermet. This produced backbones with grains up to 5 µm in diameter, but was not easily reproducible.

3.3 Infiltrations

Infiltration has become a widely used method of both enhancing the performance of existing electrodes, as well as to create new novel electrode morphologies [109–119]. Numerous researchers have used this technique to fabricate multi-phase Cu-based electrode microstructures for SOFC applications. The process is illustrated in Fig. 3.2, where panel A) shows the initial backbone structure. An infiltration solution is then applied, B), and results in two morphologies that depend on the composition of the infil-

trated solution, as well as the post-infiltration treatment. Panel C) shows an infiltration used for particle deposition, and panel D) shows a thin film coating. Aqueous copper

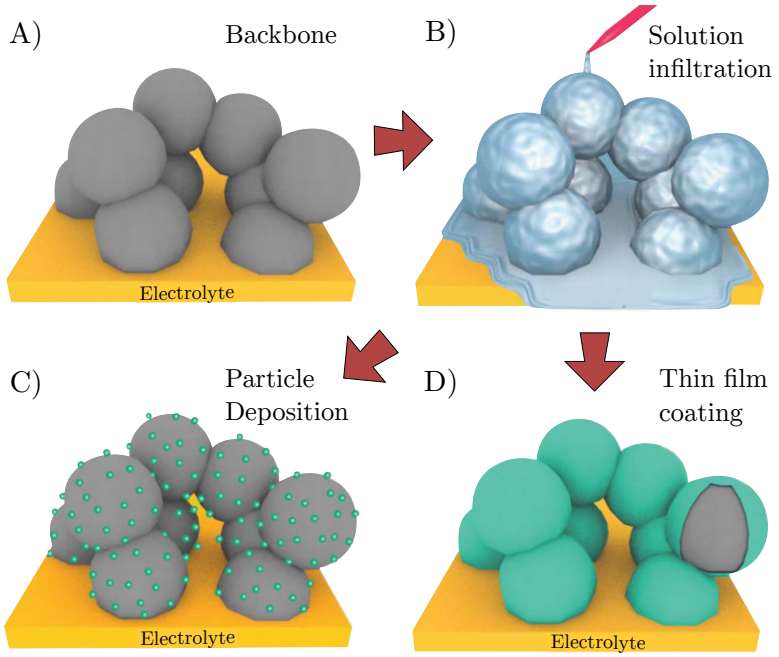

Figure 3.2: Illustration of the backbone infiltration process resulting in two different morphologies, a thin film coating and particle deposition, adapted from Ding et al. [110].

nitrate solutions are typically employed to introduce Cu into a backbone structure. Despite numerous attempts, this method did not form a homogeneous distribution of Cu. Aqueous $Cu(NO_3)_2$ tends to nucleate around pre-existing existing CuO or $Cu(NO_3)_2$ particles. It was reported that the addition of urea, in a 1:1.5 metal ion to urea ratio, mitigates this effect, where upon heating to 363 K the urea-nitrate solution hydrolizes and forms a coating of copper hydroxide [115]. This method improved results, but however the coating was still not uniform and portions of the backbone remained bare. Even with repeated attempts a complete coating was not obtained, although this may have due to an unreported aspect of the process, such as the possible addition of a wetting agent or other surfactant, or to experimental error. The urea-nitrate solution has high viscosity even at low concentrations, indicated by the high contact angle of a drop of solution on the surface of a glass slide. Additionally, due to the high surface tension, this infiltration solution was also not able to penetrate into the entire depth of a finely porous backbone microstructure. To enhance the quality of the infiltration, citric acid was added as a surfactant, however the coating was still not uniform.

Organic solvents typically have low viscosities and surface tensions combined with high vapor pressures, and all of these characteristics make them preferable to aqueous

based solutions. Thus, as an alternative, solvent based infiltration solutions were also explored.

Solvent based solutions

Of the readily available solvents, $Cu(NO_3)_2 \cdot 3\ H_2O$ had the highest solubility in acetone. It has been reported that when certain nitrates are dissolved in acetone, with the appropriate complexing agents such as a non-ionic surfactant containing a polyethylene oxide chain, it will produce a metalloligand complex, forming a nitrate "oil" composed of a metal center surrounded by coordination polymers [120, 121]. Acetone is also thought to shift the equilibria in competitive complexation reactions when combined with aqueous metal ions [122]. Here, Triton-X (Sigma-Aldrich) was used as the non-ionic surfactant and helped to promote the formation of a uniform layer of the deposited metal nitrates. The solution wetting also benefitted by the addition of a small amount of deionized H_2O, which may have acted as a complexing agent.

Applying this nitrate solution to a surface results in a thin oily film of the metal nitrate components that displays light interference diffraction patterns, indicating the thickness of the film is approximately equivalent to the wavelengths of visible light, approximately 400 to 600 nm. The films are then decomposed at 300 °C, producing a well distributed layer of the metal oxides, which upon reduction in hydrogen forms a porous network of the metal phases. The thickness and porosity of the layers can be tailored by changing the molar concentration of the solution or the number of coatings. Fig. 3.3 shows a glass microscope slide that was coated with 3 layers of a 0.15 M $Cu(NO_3)_2 \cdot 3\ H_2O$ nitrate-acetone solution. Each coating was decomposed for 5 min at

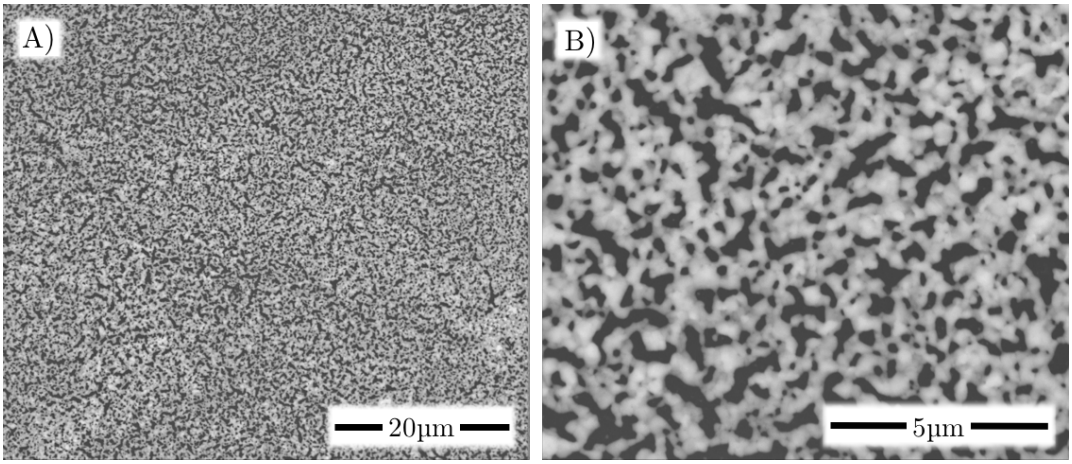

Figure 3.3: SEM images of the nitrate-acetone infiltration solution applied to a glass microscope slide. Three coatings of the solution were first decomposed at 300 °C, and then reduced in flowing 5% H_2 in Ar at 400 °C for 60 min.

300 °C to produce CuO, then the slide was exposed to flowing 5% H_2 in Ar at 400 °C for 60 min to reduce the CuO to Cu metal. The estimated thickness of the Cu network is 500 nm to 1 μm, and the resistance across approximately 4 cm was on the order of 0.01 Ω, the detection limit of the hand held multi-meter.

Thermal stabilization

Cu is a transition metal with unusually high mobility at elevated temperatures, and in order to use Cu as an electrode for applications with proton-conducting electrolytes, this effect must be mitigated. To suppress coarsening, other researchers have combined Cu with materials such as Ta, Cr and Co [68, 70, 123, 124]. Of these, Co seems to be the most successful, and was thus used in this work. Following the approach used by the Gorte group at the University of Pennsylvania, porous backbones were infiltrated with the Cu nitrate-acetone solution and thermally stabilized with Co. Two methods of introducing Co to the electrode were used in this work, electrodeposition and co-ionic infiltration.

Electrodeposition was performed according to Gross et al. [68]. The electroplating solution, as described, consisted of 100 g/L of $CoCl_2 \cdot 6\ H_2O$ and 60 g/L H_3BO_3 in deionized water, and HCl was slowly added to adjust the pH to 2. Using a Co wire as the anode and a tubular Cu infiltrated backbone with an area of 3 cm^2 as the cathode, a 10±5 mA plating current was applied for 30 min, producing approximately 1 $mg\,cm^{-2}$ of a Co coating. After rinsing with deionized water, the Cu color of the electrode had noticeably changed.

The cell was installed in a ProboStat^{TM} (NORECS, Norway) and heated to 750 °C in flowing 5% H_2. A constant frequency 10 kHz impedance measurement was used to monitor the thermal stability of the Cu electrode. The measured resistance increased by orders of magnitude over a 24 h period, indicating a loss of tpb length due to the coarsening of the infiltrated composition. Fig. 3.4 shows an example of this, where the final image shows a significantly coarsened metal phase, revealing the initial backbone microstructure. Numerous samples were electroplated for different times and at different plating currents, and in most cases, the deposition of Co was non-uniform due to the evolution of Cl gas from the plating solution and its subsequent entrapment within the backbone. Overall, the electrodeposition of Co will thermally stabilize the Cu microstructure, however, the technique did not reliably produce thermally stable Cu films within the backbone structure.

Due to the continued coarsening of Cu thin film coatings on backbone microstructures, an alternative approach of entirely filling the porosity of the backbone with a multi-phase composition was proposed. Cu-Co nitrate-acetone infiltration solutions

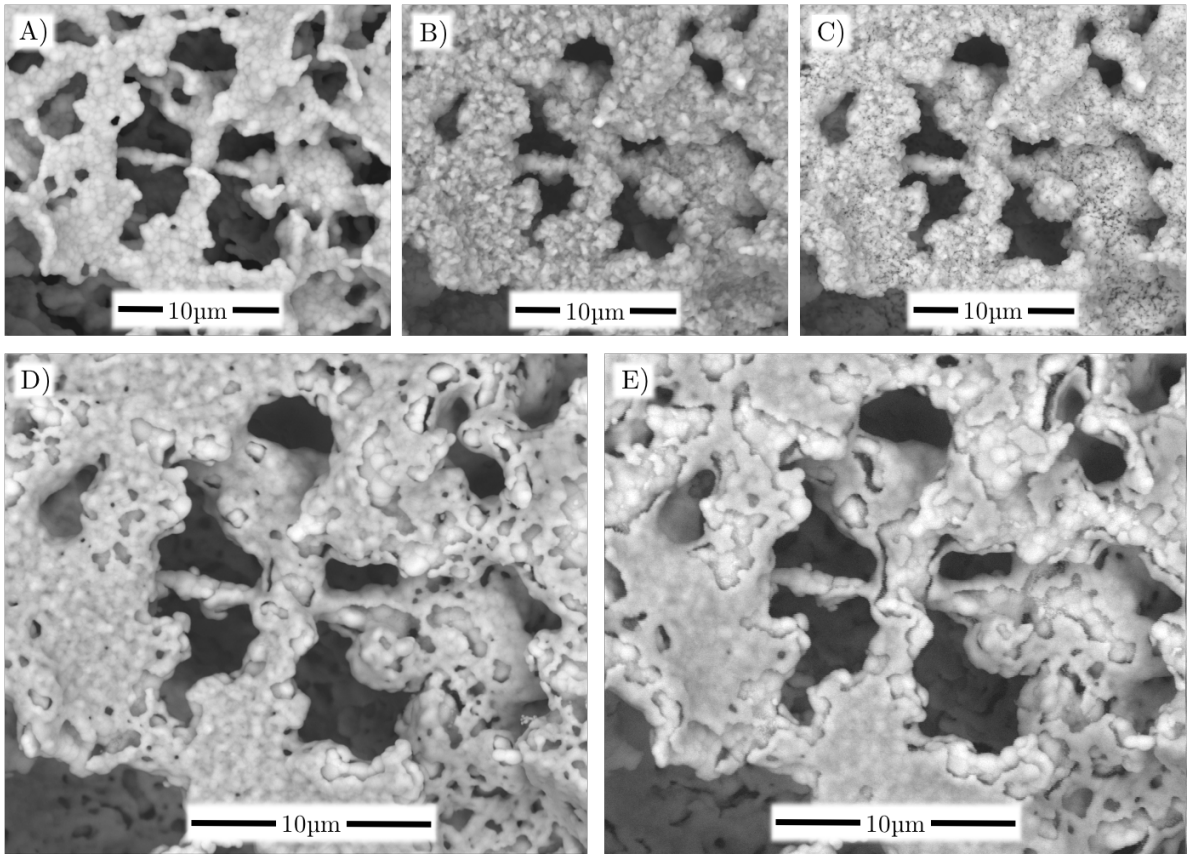

Figure 3.4: Electroplated backbone microstructure: (A), BZCY72 Cerpotech based backbone on an unreduced NiO-cermet supported membrane, (B), CuO coating after infiltration and nitrate decomposition, (C), CuO coating reduced to conductive Cu metal prior to Co plating, (D), Co plated coating after annealing at 750 °C for 2 h, (E), Post testing electrode showing continued coarsening after 6 h at 750 °C.

were prepared from $Cu(NO_3)_2 \cdot 2.5\ H_2O$ with 25% $Co(NO_3)_2 \cdot 6\ H_2O$, as described in the previous section. This solution was then applied to both the bare surfaces of full length tubular Ni-BZCY72 electrode supported membranes as well as to sections of the tubes with backbones.

Catalytic modification

The key characteristics which are helpful in understanding the catalytic properties of an oxide are its redox properties and variable oxidation states [125]. The reducibility of an oxide is a defining characteristic of its chemical reactivity, as most often it only becomes an active catalyst after the generation of oxygen vacancies [126]. Cu-Co bimetallic compositions are known to have a higher catalytic activity than Cu alone, however in order to increase the reactivity further, CeO_2 was investigated as an electrocatalyst [67]. CeO_2 is well known for exhibiting numerous catalytic properties, and

as such has been the subject of considerable research [127–129]. It will reduce from CeO_2 to $CeO_{2-\delta}$ by forming oxygen vacancies, but can only be reduced to pure metal at temperatures greater than 1200 °C [128–131]. The morphology and surface orientation of the deposited Ce has a significant impact on its catalytic activity as well. Calcining in an oxidizing atmosphere at high temperature will cause considerable grain growth, which in turn decreases its catalytic activity [132]. Reduced ceria will remain smaller particle sizes with higher catalytic activity, thus it is advantageous to anneal in a reducing atmosphere, [129]. When used in combination with a transition metals, such as Cu and Co, electronic interactions between the metal and the oxide can also give rise to interesting catalytic properties [130]. Specific to the Cu-Ce system, in many cases it is CeO_2 that acts as the support for Cu and CuO [133–135]. As an inverse catalyst, CeO_2 has been applied to the surface of Cu electrodes with much success [63, 71, 115, 126, 136]. This is the approach taken in this work, where the low catalytic activity and slow HOR kinetics of Cu-Co electrodes have been enhanced with Ce.

4 Experimental Methodology

4.1 Test System

All measurements were done using a ProboStat™ sample holder and gas mixer (NORECS, Norway). Fig. 4.1 shows the ProboStat™ sample holder, with both tubular Ni-cermet supported BZCY72 membrane with a Cu-based anode and metal point-

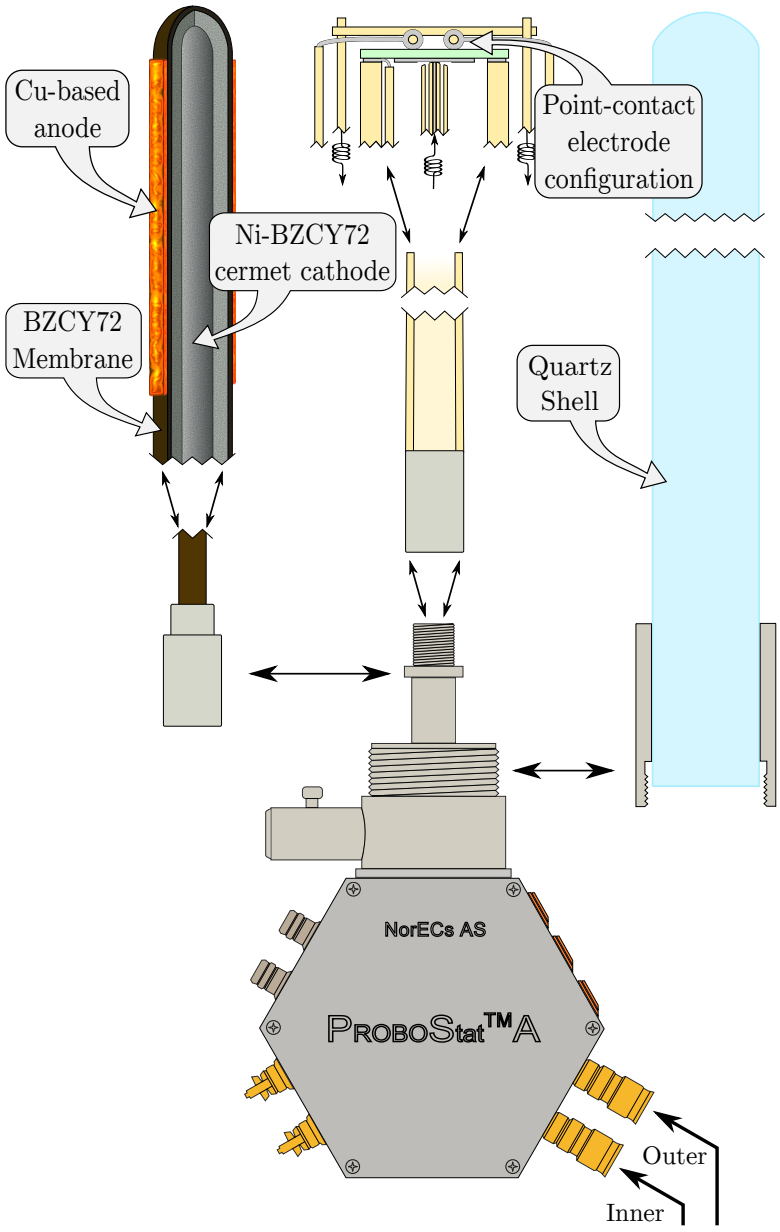

Figure 4.1: The NORECS ProboStat™ sample holder and the test configurations used in this work: a Cu-based anode applied to the surface of a Ni-BZCY72 cermet supported membrane and a metal BZCY72 point-contact electrode.

contact electrode test configurations (not to scale). Gas composition was controlled with a gas mixer, similar to that shown in Fig. 4.2, by diluting pure or mixed gases with a carrier gas, typically He or Ar. Water-vapor was controlled by passing the gas stream

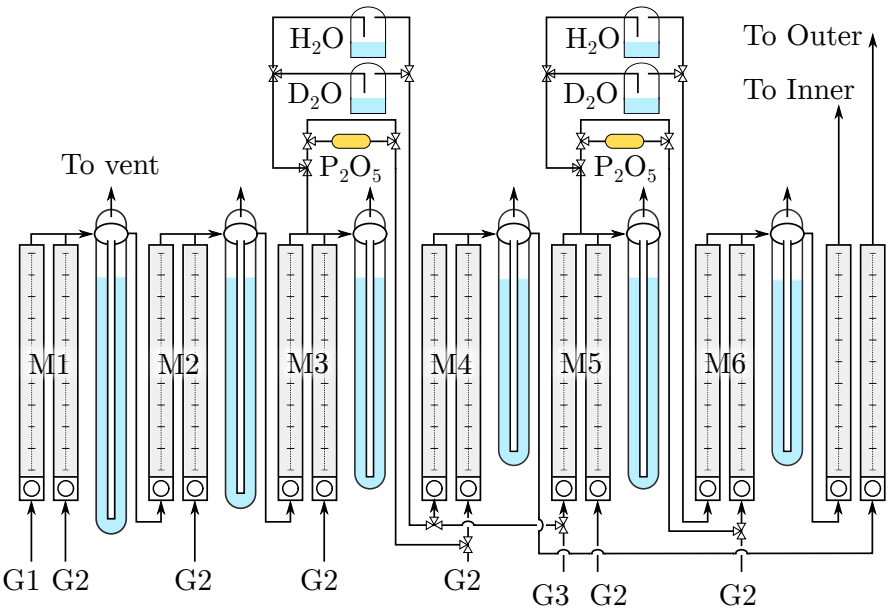

Figure 4.2: NORECS ProboStat^{TM}, showing a tubular Ni-cermet supported Cu-based electrode and point-contact electrode configurations, with a 4 and 2 stage gas mixer for the feed and sweep streams, respectively.

through a KBr saturated H_2O bubbler at room temperature, providing a nominal water vapor content of $pH_2O = 0.027$ atm. The flow rates were controlled with manual flow meters (Brooks) and partial pressures were calculated using the Gasmix software (NORECS, Norway). Here, the gas mixer is shown with both H_2O and D_2O wetting stages, as well as a P_2O_5 drying stage. G1 and G3 are typically the feed and sweep gases, respectively, while G2 is the diluent. The sequentially smaller glass bubbler tubes are in place to maintain a constant back pressure in the feed and sweep gas lines.

4.2 Configurations

Point-contact electrodes

Electrode studies in solid state electrochemistry often utilize porous Pt or other noble metals, however this is highly dependent on the electrode microstructure and may suffer due to delamination or other reactions with the electrolyte [137]. Point-contact electrodes are better configurations with which to obtain detailed information about the reaction kinetics at the metal-electrolyte interface. The simplified geometry removes variables such as porosity and microstructure, and reduces the complexities of

composite electrodes, restricting the length of the 3pb to the perimeter of the electrode contact area. Originally derived from aqueous electrochemistry, Newmans formula, (4.1), has been used by numerous researchers to calculate both the perimeter and the area of a point-contact electrode [42, 138–143].

$$r = \frac{\pi}{4\,\sigma_k\,R_j} \tag{4.1}$$

The calculation yields the radius of the footprint (assumed to be circular) of the point-contact electrode, and is inversely proportional to the measured electrolyte resistance (R_j) and known electrolyte conductivity (σ_k). This relationship is experimentally valid only when two conditions are met: 1) the thickness of the electrolyte must be greater than 5 times the diameter of the working point-contact electrode, and 2), the polarization resistance of the working electrode must be much larger than that of the counter electrode, so that the measured resistance is entirely dominated by the working electrode [137]. The working principle of a Cu point-contact electrode on a solid state electrolyte is shown in Fig. 4.1, where the equipotential surfaces of the working and counter electrodes produce a potential gradient across the electrolyte. The point-contact electrode

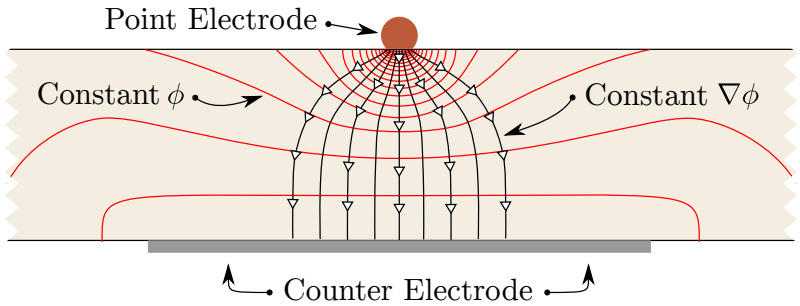

Figure 4.3: Illustration of a point-contact metal-electrolyte interface, showing the equipotential surfaces (red lines) of the working point electrode and the counter electrode.

configuration used in MI was composed of Cu and Pt wires bent around an alumina support, and pressed against the electrolyte surface. More complex configurations have also been used to investigate the characteristics of composite electrodes, such an approach was accomplished by machining conical architectures with well defined points, and pressing the point directly against the electrolyte surface [137].

Ni-cermet supported membranes

The typical tubular Ni-cermet supported electrode membrane morphology is shown in Fig. 4.4. The ceramic phase of the cermet microstructure is similar to that of the po-

rous backbones described in the previous section and seen in Fig. 3.1, where instead, here the open porosity is filled with Ni-metal. The susceptibility of Ni to carbon deposition and sulphur poisoning removes these electrodes as candidate anodes for low $p\mathrm{H_2O}$ applications in hydrocarbon containing fuels. This however does not preclude the Ni-cermet supported membrane architecture from use in developing other novel electrode architectures. The same principle as for the point-contact electrode applies; with the Ni-cermet electrode as a counter electrode, the polarization resistance of the working electrode is assumed to dominate EIS spectra. These tubes were thus used in small sections to test infiltrated backbones, however one of the limitations is that when the working electrode exhibits high performance, there is a question of whether or not the Ni-cermet contributes to the observed spectra.

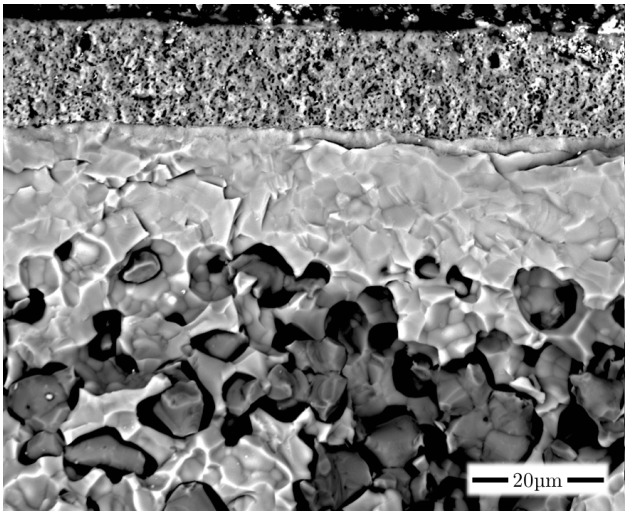

Figure 4.4: SEM image of a Ni-cermet supported BZCY72 membrane with a painted LSCF elelctrode, corresponding to the configuration used in Manuscript V.

4.3 Electrochemical Measurements

Impedance spectroscopy

Electrochemical impedance spectroscopy (EIS) is a method of studying the electrochemical properties of bulk materials and their interfaces, where the basic approach is to apply an electrical stimulus and record the response. This is depicted schematically in Fig. 4.5, where the current, i(t), is measured as a function of voltage, v(t). Typically, a small voltage, $v(t) = v_a \sin(\omega t)$, is applied and the resulting current is recorded, $i(t) = i_m \sin(\omega t + \theta)$, measuring the change in amplitude and phase, θ, of the applied signal. In the time domain, the differential equations for capacitive and inductive elements can prove to produce an intractable problem, so analysis is typically carried out in the frequency domain. Through Fourier transforms, the more simplified voltage-current relations are similar to Ohm's law, and defined in terms of angular frequency, ω, impedance is expressed as a complex number,

$$Z(j\omega) = Z' - jZ'' \tag{4.2}$$

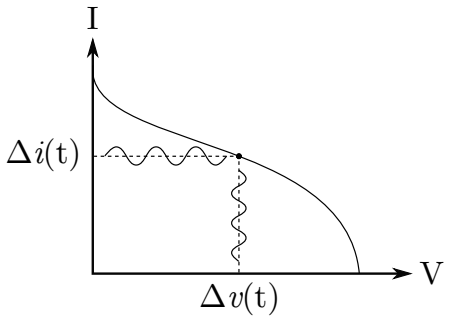

Figure 4.5: The principle of impedance spectroscopy, a sinusoidal electrical stimulus is applied and the change in amplitude and phase of the resulting signal is measured as a function of frequency. (Adapted from [144])

The magnitude is referred to as the modulus,

$$|Z| = \sqrt{(Z')^2 + (Z'')^2} \tag{4.3}$$

with real and imaginary components,

$$Z' = |Z|\cos(\theta) \qquad Z'' = |Z|\sin(\theta) \tag{4.4}$$

that are related by the phase angle, $\theta = \tan^{-1}(Z''/Z')$. By plotting impedance as a planar vector using both rectangular and polar coordinates in an Argand diagram, shown in Fig. 4.6, we can visualize the relationship between the modulus and phase angle.

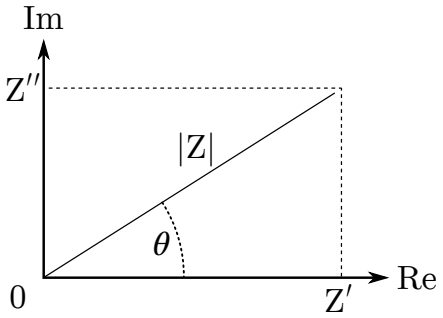

Figure 4.6: Impedance plotted as a planar vector using both cartesian and polar coordinates, showing the relationship between the modulus $|Z|$ and phase angle θ. (Adapted from [144])

Deconvolution of impedance spectra

At interfaces between different materials there are likely to be significant changes in the physical properties that, in part, define the conductivity of a system. Each interface

can result in both the accumulation and depletion of charge, resulting in resistive (R) and capacitive (C) contributions to an impedance spectra. Resistive contributions to interfacial impedance are frequency independent and are simply $Z_R = R$, while capacitive contributions are inversely proportional to frequency as, $Z_C = 1/(j\omega C)$. Polycrystalline electrolytes have many interfaces, and combined with metallic, composite or multi-phased electrodes contacting the surrounding gaseous phase, make solid-state electrochemical systems considerably more complex than their aqueous counterparts [144]. Each interface exhibits a different polarization response that is dependent upon both the presence of charged species and the microstructures of the electrolyte and electrodes. Lower frequency responses are characteristic to chemical reactions and charge transfer, and high frequency responses are attributed to faster phenomena such as ionic transport. Fig. 4.7 shows a Nyquist diagram, plotted as Z′ vs. Z″ (Ω), of an impedance spectra that contains primarily lower frequency electrode contributions. EIS data is

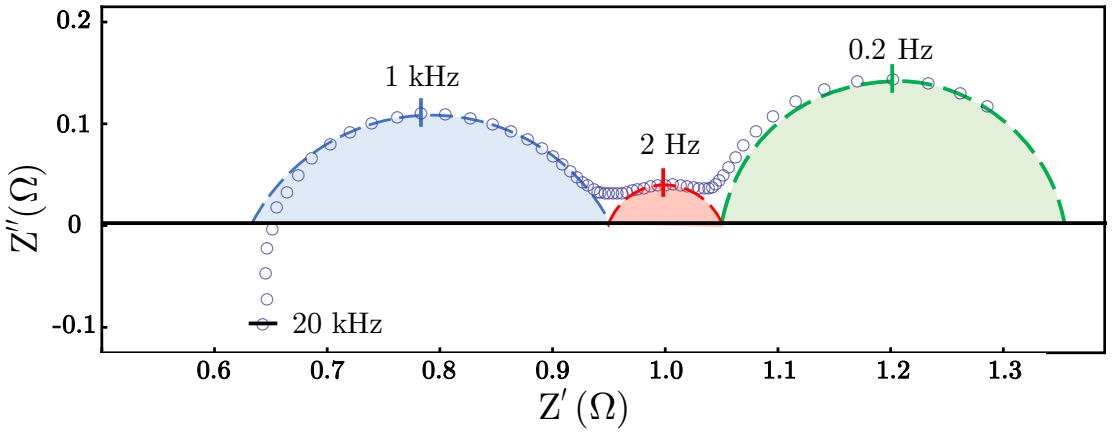

Figure 4.7: Impedance spectra showing the peak frequencies of contributions attributed to charge (1 kHz) and mass transfer (2 Hz), and gas phase diffusion (0.2 Hz).

analyzed using an equivalent circuit model, where various circuit elements are used to describe the different characteristics of an impedance spectra. Responses such as those seen in Fig. 4.7 typically have peak frequency time constants of,

$$\tau = RC = 1/(2\pi f) \tag{4.5}$$

which yield semi-circles with peak frequencies of f. Ideally, these contributions would be represented by parallel RC elements, however, the arcs are depressed from the x-axis, indicating a distribution of time constants. This is due to the way that material defects and different morphological orientations effect electrochemically active interfaces. As

a result, such relaxation rates are better characterized by a statistical distribution of time constants, represented by a constant phase element. There are multiple forms of constant phase elements; the one which was utilized in this work is the QPE introduced by Boukamp et al. [145]. The QPE has strictly empirical origins, and is an an effort to account for this distribution of time constants in the analysis of impedance spectra data [144]. The impedance of a QPE of this form is given by,

$$Z_{QPE} = \frac{1}{(Y_0\, j\omega)^n} \tag{4.6}$$

with the capacitance of the parallel R-QPE combination given by,

$$C_{QPE} = Y_0 R^{\frac{1}{n}-1} \tag{4.7}$$

In Eqs. (4.6) and (4.7), R is the resistance of the parallel R-QPE combination. The parameter n is typically between 0.25 and 1 and is related to the phase angle and radius of the impedance arc, and it describes the depression of the center of the arc below the horizontal axis. If $n = 1$, Y_0 gives pure capacitance with no resistive behavior. The spectra shown in Fig. 4.7 is typical for the impedance measurements obtained during this work, and the equivalent circuit model used for its deconvolution is shown in Fig. 4.8. The third R-QPE element seen in Fig. 4.8, R_{gpd}, represents gas phase diffusion,

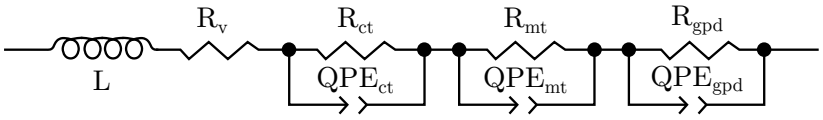

Figure 4.8: An equivalent circuit composed of an inductor, resistor and 3 RQ elements that was used to deconvolute spectra such as seen in Fig. 4.7.

a process that occurs at very low frequencies,where the QPE may become ill defined. Often a Gerischer impedance element is more appropriate in this circumstance, where a diffusion step is coupled to a chemical reaction [146]. The Gerischer impedance is,

$$Z_G = \frac{1}{Y_0\sqrt{k + j\omega}} \tag{4.8}$$

It is apparent that it has a finite value at DC, when $\omega = 0$, then the term k represents the effective transfer rate of the chemical reaction. Because Z_G is frequency dependent, it is best to utilize it only after higher frequency circuit elements have been fixed, then it strictly accounts for low frequency diffusion related contributions and can be added to the mass transport resistance.

4.4 Data Analysis

For each experimental test matrix, as the deconvolutions of the impedance spectra were conducted, the data was recorded in a spreadsheet. During this iterative process the spreadsheet plotted the $p\mathrm{H}_2$ and temperature dependencies of the charge and mass transfer conductances, as well as the QPE capacitances. The linearity of the QPE capacitances, with Log plots of the $p\mathrm{H}_2$ and temperature dependencies, helped to identify and correct outliers, and thus to evaluate the general trends in the data. Error due to the deconvolutions, experimental uncertainty (e.g. thermocouples, flow rates, etc.) as well as possible measurement error was accounted for with a 2.5 % variability.

Error in fitting

Fit parameters such as $p\mathrm{H}_2$ dependencies and activation enthalpies, extracted from the linearizations of temperature dependencies, have a statistical error associated with the goodness of fit. Often times, error in fitting is not reported, though it may be significant at times. This is accounted for through the use of the mean square predictor error, which is calculated as,

$$MSPE = \frac{1}{n}\sum_{i=1}^{n}(\hat{Y}_i - Y_i)^2 \tag{4.9}$$

where $\hat{Y}_i$ are the predicted values and Y_i are the actual values on which the fitting is based. For a large dataset where there are multiple $p\mathrm{H}_2$ and temperature dependencies, the means and standard deviations can be used to calculate the propagated error based on the MSPE.

Uncertainty

In extracting A_0 from a large set of experimental data, the mean and standard deviations of the activation enthalpies, ΔH, hydrogen pressure and water vapor pressure dependencies, n and m respectively, must all be taken into account. The relative uncertainty due to the standard deviations of these quantities should then be incorporated into the distribution of values obtained for A_0 prior to taking the logarithm, however, this process does not include any potential error introduced through deconvolution. As an example, consider the function $z = f(x, y)$ subject to small perturbations, δx and δy, that lead to δz,

$$\delta z = \frac{\partial z}{\partial x}\delta x + \frac{\partial z}{\partial y}\delta y \tag{4.10}$$

This perturbation in z is used to calculate the standard deviation for the N values of z, which is given by,

$$S_z = \sqrt{\frac{\sum(\delta z)^2}{N}} \tag{4.11}$$

Based on experimental data error analysis, and by using the definition of the standard deviations in x and y, it follows that,

$$(S_x)^2 = \frac{1}{N}\sum(\delta x)^2 \qquad\qquad (S_y)^2 = \frac{1}{N}\sum(\delta y)^2 \tag{4.12}$$

where δx and δy must be independent perturbations,

$$\sum(\delta x \delta y) = 0 \tag{4.13}$$

Then the uncertainty resulting from perturbations δx and δy,

$$S_z = \sqrt{\left(\frac{\partial z}{\partial x}\right)^2 (S_x)^2 + \left(\frac{\partial z}{\partial y}\right)^2 (S_y)^2} \tag{4.14}$$

If z is a function of more than two variables, this result can be extended by adding similar terms, and is also how the MSPE may incorporated into uncertainties of more than one type. In order to obtain the uncertainty in A_0, (2.62) becomes,

$$A_0 = \frac{1}{R}(pH_2)^{-n}(pH_2O)^{-m}\,\mathbf{e}^{\frac{\Delta H}{k_b T}} \tag{4.15}$$

and the derivatives of the respective terms for which there are standard deviations (n, m and ΔH) are obtained, i.e. $A_0 = f(n, m, \Delta H)$. It can then be shown that,

$$dA_0 = \frac{1}{R}(pH_2)^{-n}(pH_2O)^{-m}\,\mathbf{e}^{\frac{\Delta H}{k_b T}}(-\ln(pH_2) + (-ln(pH_2O) + \frac{1}{k_b T}) \tag{4.16}$$

Here the terms,

$$\left(\frac{\partial f}{\partial n}\right) = \left(\frac{\partial f}{\partial m}\right) = \left(\frac{\partial f}{\partial \Delta H}\right) = \frac{1}{R}(pH_2)^{-n}(pH_2O)^{-m}\,\mathbf{e}^{\frac{\Delta H}{k_b T}} = A_0 \tag{4.17}$$

can be taken outside of the square root. The remaining terms inside the root are,

$$(S_n)^2 = (\delta n)^2 = (-\ln(pH_2))^2 \tag{4.18}$$

$$(S_m)^2 = (\delta m)^2 = (-\ln(pH_2O)^2 \tag{4.19}$$

$$(S_{\Delta H})^2 = (\delta \Delta H)^2 = (\frac{1}{k_b T})^2 \tag{4.20}$$

for which there are standard deviations based on the distributions of ΔH, n and m. Then the relative uncertainty in A_0 based on using the mean values of these quantities is expressed as,

$$S_{A_{0,R}} = \frac{S_{A_0}}{A_0} = \sqrt{(S_n)^2 + (S_m)^2 + (S_{\Delta H})^2} \tag{4.21}$$

By solving (2.62) for each experimental condition, for each metal electrode, a small distribution of values for A_0 was obtained. The relative uncertainty in A_0 was included in the total uncertainty as $A_{0,i} \pm S_{A_{0,R}}$ with the mean and standard deviations calculated as,

$$\overline{A_{0,t}} = \frac{\sum A_{0,i}}{N} \tag{4.22}$$

and so,

$$S_{A_{0,t}} = \sqrt{\frac{2\sum(\overline{A_{0,t}} - A_{0,i})^2}{(N-1)}} \tag{4.23}$$

4.5 Hydrogen Flux

Flux calculations require knowledge of the concentrations of H_2 and He gas, χ_{H_2} and χ_{He}, as well as the total volumetric flow rate, $\dot{V}$, of a gas stream. Here, He is used for leak detection, and is typically near the same concentration of H_2. Both the GC and MS require calibration for each gas, while the flow rate can be measured and calculated directly with a simple algebraic formula. In principle, the methods of calibrating a gas chromatograph (GC) and mass spectrometer (MS) are the same, however, because the ways in which the instruments collect data, analysis may be fundamentally different. Both instruments relate a measured signal to a known concentration. GC's quantify measurements based on the area beneath the signal curve, and each molecule will have a characteristic peak retention time with an associated window width. The area under the curve is then calibrated to the known concentration, and then the concentration of an unknown gas is given directly by the user interface. An MS operates based on the ionization of a molecule at the filament, and the time of flight to the detector. The time of flight is dependent upon the charge to mass ratio of the respective ion. For example, water vapor will produce a primary signal at 18 a.m.u. but will also have secondary signals at 17, 16, 2 and 1 a.m.u. The intensity of the signal at each a.m.u. is then calibrated to a known concentration of the input gas. When testing the electrodes reported in MII, an Agilent 3000 μ-GC was used, and in MV, an MKS Cirrus atmospheric MS was used.

Volumetric flow rate measurements were conducted using a standard 100 mL soap film bubble meter (Agilent). An outlet gas line from the ProboStat^{TM} was first sampled by the μ-GC, then fed either to vent or through the bubble meter. Due to low flow

rates when using the μ-GC, the flow rate measurement was coordinated with the GC sampling rate and total run time. The MS maintained a constant flow into the chamber, and this was easily accounted for by measuring the downstream flow rate both with the MS online and without MS sampling. The final flux density calculation based on the above parameters is,

$$J_{H_2} = \frac{\dot{V}}{A}\left(\chi_{H_2} - \frac{p\mathrm{H}_2}{p\mathrm{He}}\chi_{He}\right) \tag{4.24}$$

where A is the electrode area, and $p\mathrm{H}_2$ and $p\mathrm{He}$ are the inlet pressures of H_2 and He, respectively.

Faradaic efficiency

The Faradaic rate of an electrochemical cell is the theoretical correlation between current and the rate at which a species is oxidized or reduced. The equivalency that describes the rate of an electrode reaction is,

$$\frac{dN}{dt} = \frac{1}{nF}\frac{dQ}{dt} = \frac{i}{nF} \tag{4.25}$$

where, N is moles, n is the number of electrons, F is Faraday's constant, Q is coulombs and i is current. Heterogeneous electrode reactions are more complex than chemical reactions, and typically occur only at the electrode-electrolyte interface. They are subject to mass transfer and kinetic limitations and are thus usually described with area specificity [56]. The Faradaically predicted flux density, J_F, of the electrochemical reaction is then given by,

$$J_F = \frac{1}{A}\frac{dN}{dt} = \frac{i}{nFA} = \frac{j}{nF} \tag{4.26}$$

where A is the electrode area and j is current density. The Faradaic efficiency of a solid-state proton-conducting electrochemical cell is then defined for electrolytic or galvanic operation, where when connected to an external circuit the hydrogen flux is equivalent to the total current, as in Eq. (2.18) in section 2.2. Faradaic efficiency is then the ratio of the measured flux, as in Eq. (4.24), to the theoretical flux, Eq. (4.26), and is,

$$\eta_F = \frac{J_{\mathrm{H}_2}}{J_F} = \frac{\dot{V}\left(\chi_{H_2} - \frac{p\mathrm{H}_2}{p\mathrm{He}}\chi_{He}\right)}{\frac{i}{nF}} \tag{4.27}$$

5 Manuscripts

Manuscript I:

Comparison of Cu and Pt point-contact electrodes on proton conducting $BaZr_{0.7}Ce_{0.2}Y_{0.1}O_{3-\delta}$

Shay Robinson, Christian Kjølseth, Truls Norby
Solid State Ionics, 2017 **306** 38−47

I

Solid State Ionics 306 (2017) 38–47

Contents lists available at ScienceDirect

Solid State Ionics

journal homepage: www.elsevier.com/locate/ssi

Comparison of Cu and Pt point-contact electrodes on proton conducting $BaZr_{0.7}Ce_{0.2}Y_{0.1}O_{3-\delta}$

Shay Robinson[a,*], Christian Kjølseth[b], Truls Norby[a]

[a] Centre for Materials Science and Nanotechnology, Department of Chemistry, University of Oslo, FERMiO, Gaustadaléen 21, NO-0349 Oslo, Norway
[b] CoorsTek Membrane Sciences AS, Gaustadaléen 21, NO-0349 Oslo, Norway

I

ARTICLE INFO

Article history:
Received 21 November 2016
Received in revised form 13 February 2017
Accepted 16 February 2017
Available online 8 March 2017

Keywords:
Point-contact electrode
Hydrogen oxidation
Platinum
Copper
Proton ceramic

ABSTRACT

The hydrogen oxidation kinetics of Cu and Pt point contact-electrodes on proton conducting $BaZr_{0.7}Ce_{0.2}Y_{0.1}O_{3-\delta}$ (BZCY72) were studied over a range of temperatures and hydrogen pressures using impedance spectroscopy. Characteristic capacitances were used to identify process contributions as charge and mass transfer, then Langmuir adsorption theory and Butler-Volmer charge transfer formalism were used to propose a hydrogen oxidation model to describe the experimental data. The charge transfer hydrogen pressure dependencies were $pH_2^{3/4}$ for Cu, attributed to a high occupancy of adsorbed oxygen at three-phase boundary sites in the water-vapor containing atmosphere, and $pH_2^{-1/4}$ for Pt, corresponding to a hydrogen saturated interface. The Cu and Pt point contact electrodes exhibit similar temperature dependencies for charge transfer, with activation enthalpies of 0.82 and 0.93 eV, and pre-exponentials of approximately 160 and 1000 $\Omega^{-1}cm^{-1}$, respectively. Mass transfer dominated the total polarization resistance of both metal point contact electrodes, exhibiting a $pH_2^{1/2}$ hydrogen pressure dependency. The activation enthalpies are 1.21 eV for Cu and 0.73 eV for Pt, reflecting the higher catalytic activity generally expected for Pt. Pre-exponentials for mass transfer of approximately 10,000 $\Omega^{-1}cm^{-1}$ for Cu and 2.6 $\Omega^{-1}cm^{-1}$ for Pt, indicate that Cu utilizes a much larger active interface. Cu may be a suitable candidate electrode material for use in carbonaceous atmospheres, but the results of this work indicates that it suffers from a high activation enthalpy for mass transfer in the hydrogen oxidation reaction.

1. Introduction

1.1. Background

The bulk properties, stability and performance of many different ABO_3 perovskite proton conductors, such as $BaZr_{0.9-x}Ce_xY_{0.1}O_{3-\delta}$ (BZCY), have been extensively investigated for more than three decades [1–15]. However, mixed ionic-electronic conducting electrodes that are suitable for hydrocarbon utilization in BZCY electrochemical devices have not been reported. Such electrodes are subject to a number of constraints. First, the electrode must be chemically and mechanically compatible with the carbonaceous gas phase, the electrolyte, and the interconnects. This emphasizes a resistance to carbon deposition, which would reduce the number of three-phase boundary (3pb) sites and subsequently deactivate the electrode. Both Cu and BZCY exhibit a resistance to carbon deposition [16–20], and this makes these materials attractive for the development of industrial applications with hydrocarbons using proton ceramics. Second, it is also desirable that the electrode provides catalytic activity towards the hydrogen oxidation reaction (HOR) at the anode of any electrochemical device. Many researchers have studied Cu as a suitable metal for application as an electrode in solid oxide fuel cells, and though Cu is an excellent electronic conductor, it suffers from poor HOR kinetics due to a lack of catalytic activity [21–24]. Thus, better characterization and understanding of the HOR kinetics at the Cu-BZCY interface is necessary in order to develop an electrode suitable for applications such as fuel cells and membrane reactors in carbon containing atmospheres.

1.2. Approach

In this work, metal point-contact electrodes were used to directly compare the HOR kinetics of Cu and Pt at the metal-BZCY72 ($x = 0.2$) electrolyte interface. Pt is well researched, and known to have good catalytic activity towards the HOR [25,26]; thus it is a valuable metal with which to compare the kinetic behavior of Cu. An

* Corresponding author.
E-mail address: s.a.robinson@smn.uio.no (S. Robinson).

http://dx.doi.org/10.1016/j.ssi.2017.02.014
0167-2738/

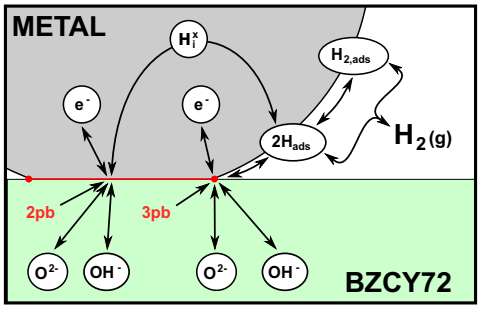

Fig. 1. Possible reaction paths at the point-contact metal-BZCY72 interface: associative ($H_{2,ads}$) and dissociative adsorption ($2H_{ads}$), with surface diffusion to the 3pb or interstitial diffusion (H_i^x) to the 2pb, and finally proton transfer to an oxide ion (O^{2-}).

HOR model, based on Langmuir adsorption theory and Butler-Volmer charge transfer formalism, is proposed to interpret experimental data obtained through electrochemical impedance spectroscopy (EIS). The HOR model was used to identify and explain hydrogen pressure (pH_2) dependencies, and temperature dependencies were used to extract activation enthalpies and pre-exponentials in order to compare the reaction kinetics of the two metals.

1.3. Point-contact electrode architecture

Point-contact electrodes are useful configurations with which to obtain detailed information about the reaction kinetics at the metal-electrolyte interface. The simple geometry of point-contact electrodes removes variables such as porosity and microstructure, and simplifies the complexities of composite electrodes, significantly reducing the length of the 3pb. Newman's formula, Eq. (1), has been used by numerous researchers in similar point-contact electrode studies [27–33].

$$r = \frac{1}{4\,\sigma_k\,R_j} \tag{1}$$

The calculation yields the radius (r) of the point-contact electrode area (assumed to be circular) and is inversely proportional to the measured electrolyte resistance (R_j) and known electrolyte conductivity (σ_k). For point-contact electrode configurations, the 3pb is restricted to the perimeter of the contact area of the metal-electrolyte interface.

1.4. Hydrogen oxidation reaction pathways

Fig. 1 schematically depicts the metal point-contact electrode to electrolyte interface and suggests potential reaction paths, which may progress in multiple steps and possibly through competing mechanisms.

The proposed reaction paths first involve the adsorption of H_2 onto the metal electrode surface. This can occur associatively, leading to the physisorption of molecular hydrogen, $H_{2,ads}$. Associatively physisorbed species must then overcome an additional energy barrier in order to dissociate and become chemisorbed atomic hydrogen, H_{ads} [26,34–36]. Dissociative adsorption of hydrogen is favorable on Pt surfaces due to the catalytic activity of the metal, leading directly to atomic chemisorbed H_{ads}. Then there are then two possible paths H_{ads} may take before the charge transfer step. H_{ads} may diffuse on the metal surface to the 3pb, where charge transfer then takes place. Or, after dissociation neutral hydrogen may dissolve interstitially as H_i^x and diffuse through the Cu metal to the two-phase boundary (2pb) of the metal-electrolyte interface. Hydrogen permeability in Cu is non-negligible, and has been reported at temperatures as low as 325 °C [37–40]. Thus, depending upon operating conditions hydrogen may potentially be incorporated into the electrolyte via both mechanisms.

2. Experimental

2.1. Methods and materials

Electrolyte pellets were prepared from spray pyrolyzed BZCY72 nanopowder (CerPoTech) containing 1 wt% ZnO (Sigma Aldrich). ZnO has been shown to be an effective sintering aid to achieve uniform grain growth and high density in BZY [41,42]. The powders were ball milled in a yttrium stabilized zirconia (YSZ) jar with isopropyl alcohol, and then hand mixed with 1 wt% PVB (Sigma Aldrich) binder. After drying overnight at 120 °C, the powder was uniaxially cold pressed into discs at 500 MPa, and sintered at 1500 °C for 10 h. The sintered pellets were approximately 95% of the theoretical density of BZCY72 [43].

One side of the sintered pellet was polished to a high finish for the point-contact electrode interface, and the other side was polished moderately to facilitate adhesion of the Pt counter electrode. Pt ink was applied to two concentric regions, as shown in Fig. 2, to serve as the counter and reference electrodes, and then fired at 1100 °C for 2 h.

A point-contact electrode assembly was constructed by wrapping 0.5 mm Pt wire (Thermocouple quality, K.A. Rasmussen, Hamar, Norway) or 0.5 mm Cu wire (Alfa Aesar #10973, 99.999%) around small diameter alumina tube. The point electrode assembly was then

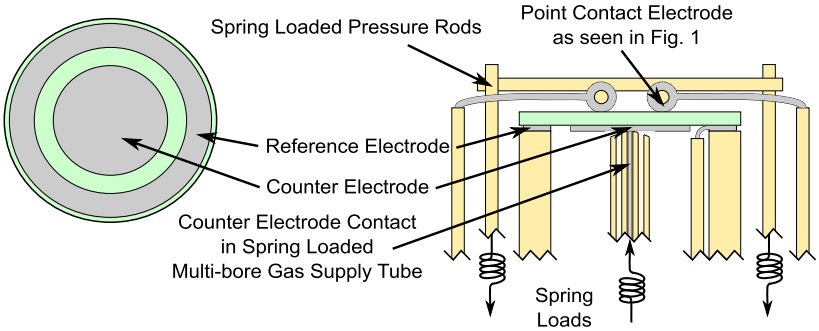

Fig. 2. Point contact electrode schematic.

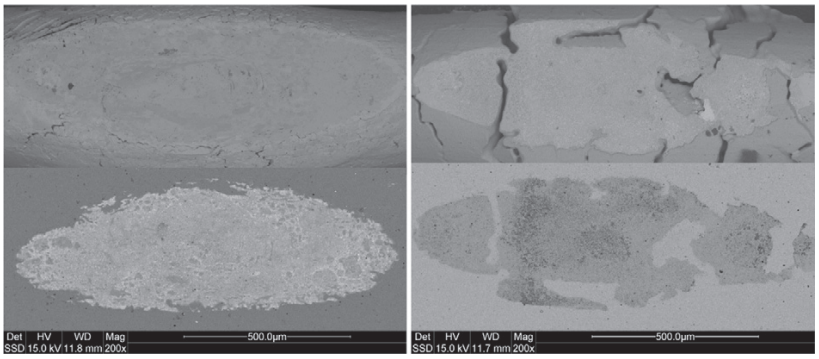

Fig. 3. Post testing SEM images of the Pt (ℓ) and Cu (r) point-contact electrode to electrolyte interfaces, showing the metal electrodes (*top*) and the electrolyte (*bottom*) surface. Images have been enhanced to show the contrast of the interface.

secured on the top of the polished surface of the electrolyte with spring loaded alumina rods. A second identical sintered pellet was also prepared for a standard conductivity measurements. After polishing, symmetric Pt electrodes of ~0.8 cm diameter were painted on each side of the second pellet and then also fired at 1100 °C for 2 h, corresponding to the counter electrode in Fig. 2.

2.2. Procedure

EIS measurements were conducted every 25 °C while decreasing the temperature from 600 to 450 °C. Hydrogen and water vapor pressures were changed systematically; pH_2 was tested at 0.5, 0.05, and 0.005 atm, for each pH_2O of 0.027 and 0.0027 atm. Once reaching equilibrium, as determined by a 10 kHz impedance measurement, frequency sweeps were performed in the range 1 MHz to 10 mHz with a 50 mV AC amplitude, using a Gamry REF-3000.

EIS measurements were also performed on the symmetric Pt electrode pellet in order to obtain the electrolyte conductivity, σ_k, for use in Newman's formula. The impedance measurements were taken from 600 °C to 150 °C in a $pH_2 = 0.05$ and $pH_2O = 0.027$ atmosphere. All impedance spectra deconvolutions were done using the analysis software Z-View.

3. Results

3.1. Point-contact electrode-electrolyte interface

Using the electrolyte conductivity, σ_k, in combination with the measured electrolyte resistance, R_j, for the Cu and Pt point electrodes, the radius of the contact area of each electrode was calculated with Eq. (1). The activation energy at the lowest temperatures, obtained from the regression of $\ln(\sigma T)$ vs. 1/T, was calculated to be $E_a = 0.48$ eV, which is in agreement with literature [41,44] for the proton conductivity of BZCY materials. The mean values of the radii were $r_{Cu} \approxeq 0.027$ cm and $r_{Pt} \approxeq 0.028$ cm, yielding contact areas of $A_{Cu} \approxeq 0.0026\,cm^2$ and $A_{Pt} \approxeq 0.0033\,cm^2$, and perimeters of $P_{Cu} \approxeq 0.17$ cm and $P_{Pt} \approxeq 0.18$ cm, for the Cu and Pt point electrodes, respectively. SEM images of the Pt and Cu point-contact electrode-electrolyte interfaces are shown in Fig. 3.

The detailed perimeters of each of the point contact electrodes, seen in Fig. 3, were traced using graphics software. A correlation with the scale bars in the SEM images was established and used to estimate the length of each perimeter, yielding 0.58 cm for the Cu point contact and 0.50 cm for the Pt point contact. The software also estimated each of the contact areas as 0.0028 and 0.0032 cm^2 for

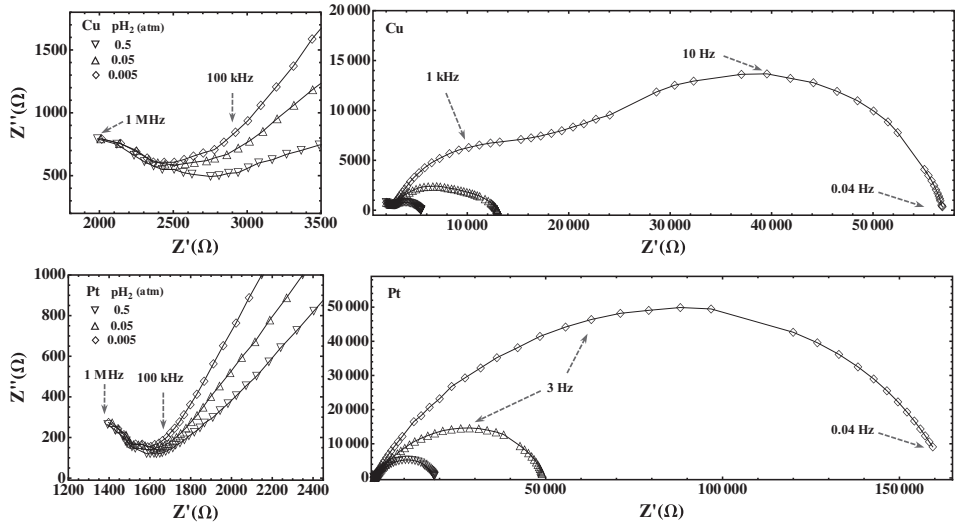

Fig. 4. Representative impedance spectra (noise removed) for the Cu (*top*), and Pt (*bottom*) point electrodes, showing high (*left*) and low (*right*) frequency components. Spectra were obtained at 600 °C by varying pH_2 in a $pH_2O = 0.0027$ atm.

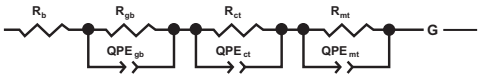

Fig. 5. R-QPE equivalent circuit used in the deconvolution of point-contact electrode and electrolyte conductivity data.

Cu and Pt, respectively. Based on the correlation between the calculated and estimated contact areas, the software generated perimeters are considered to be better estimates of each of the point-contact 3pb lengths than those obtained with Eq. (1) due to the irregular perimeter of the actual contact area, as seen in Fig. 3.

3.2. Representative impedance spectra and data analysis

Representative impedance spectra are shown in Fig. 4, and are composed of multiple overlapping arcs.

Spectra deconvolutions were performed in the software Zview using an equivalent circuit composed of a resistor, a series of parallel resistor and constant phase element (R-QPE) components, and a Gerischer element, as shown in Fig. 5. The Gerischer element was used due to the asymmetric shape of the low frequency response, and was applied only once higher frequency parameters had been fixed.

Point-contact electrodes exhibit capacitances that are much smaller than those typically observed for disc samples, however, it is the difference in magnitude of each characteristic that allows it to be assigned to a specific process [45,46]. In Fig. 4, the arcs at the high frequency response near 1 MHz have calculated *area specific* QPE capacitances in the order of 10^{-11} F cm^{-2}; thus these contributions were attributed to electrolyte grain boundary resistance, R_{gb}. This contribution appears to be larger for the Cu point electrode, possibly due to the migration of Cu into grain boundaries near the surface of the electrolyte. The higher frequency intercept of each grain boundary arc (not seen) was attributed to electrolyte bulk resistance, R_b. The grain boundary, R_{gb}, and bulk, R_b, resistances were summed into an electrolyte volume resistance, R_v.

The intermediate frequency response is commonly attributed to charge transfer, and in the Cu point-contact electrode spectra shown in Fig. 4 (*top*), is apparent from approximately 100 kHz to 500 Hz. This same frequency range in the Pt point-contact electrode spectra, Fig. 4 (*bottom*), is barely visible in comparison. The lowest frequency arc was attributed to electrode mass transfer processes. The sum of the low frequency R-QPE resistance and the Gerischer contribution was attributed to mass transfer, and defined as R_{mt}.

Raw capacitance values for charge transfer and mass transfer, that are seen in Fig. 6, are of the order 10^{-8} F and 10^{-7} F for Cu, and 10^{-7} F and 10^{-6} F for Pt. The above values are independent of temperature and subject to assumptions of a dominant process path: charge transfer can be subject to 2pb contact area (cm^{-2}) or 3pb length (cm^{-1}) specificity, while mass transfer can be based on 2pb contact area, 3pb length or electrode volume (cm^{-3}) specificity. Table 1 reports these values, as outlined above, by taking the mean values with hydrogen pressure, as seen in Fig. 6, and the lengths and areas reported in the previous section. The electrode volume was calculated using the wire diameter as length, yielding 3.9×10^{-4}cm^3.

In the following sections, charge and mass transfer conductances are treated using 3pb length specific assumptions.

3.3. pH_2 dependencies

Deconvolutions of the impedance spectra data were plotted as Log$(1/R_i)$ vs. pH$_2$, and are shown in Fig. 7. The average slope is shown at the bottom of each plot for electrolyte volume, charge and mass transfer at pH$_2$O = 0.027 atm and pH$_2$O = 0.0027 atm. For both the Cu and Pt point-contact electrodes, the electrolyte conductance $1/R_v$, is observed to be nearly pH$_2$ independent, as expected for the BZCY72 electrolyte.

The charge transfer resistance makes up the most significant difference between the two electrode materials. For Cu, the charge transfer conductance, $1/R_{ct}$, exhibits a $p\mathrm{H}_2^{3/4}$ dependence, while for

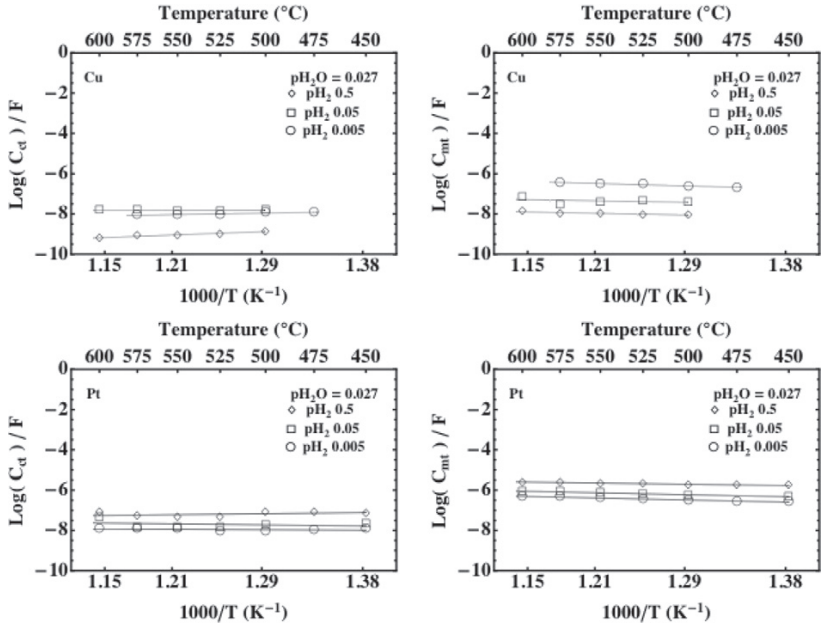

Fig. 6. Raw QPE capacitances for charge transfer (*left*) and mass transfer (*right*) for both Cu (*top*) and Pt (*bottom*) at pH$_2$O = 0.027 atm.

Table 1
The mean capacitance for charge (ct) and mass transfer (mt), with 3pb length, contact area and volume specificity.

Process specificity	Cu (F)	Pt (F)
ct unspecific	9.6×10^{-9}	4.7×10^{-8}
ct (cm^{-1})	5.6×10^{-9}	2.4×10^{-8}
ct (cm^{-2})	2.7×10^{-11}	1.5×10^{-10}
mt unspecific	2.1×10^{-7}	1.5×10^{-6}
mt (cm^{-1})	1.2×10^{-7}	7.5×10^{-7}
mt (cm^{-2})	5.9×10^{-10}	4.8×10^{-9}
mt (cm^{-3})	8.2×10^{-11}	5.9×10^{-10}

Pt, $1/R_{ct}$ exhibits a $pH_2^{-1/4}$ dependence. The mass transfer conductance, $1/R_{mt}$, exhibits a $pH_2^{1/2}$ dependence for both metal electrode materials.

3.4. pH_2O dependencies

The data shown in Fig. 7 was plotted vs. pH_2O, and selected graphs are shown in Fig. 8.

The Cu point-contact electrode has a slight pH_2O dependence of the charge transfer resistance at $pH_2 = 0.5$, but the pH_2O dependence of the charge transfer conductance is negligible at $pH_2 = 0.05$ and 0.005 (not shown). The pH_2O dependencies of the mass transfer conductance is negligible for all measured hydrogen pressures and are also not shown.

The Pt point-contact electrode shows a slight pH_2O dependence at lower hydrogen concentrations, with the effects being more pronounced at low temperature. At $pH_2 = 0.5$ the pH_2O dependence of the charge transfer conductance is negligible, as is the pH_2O dependence of the mass transfer conductance for all hydrogen pressures and temperatures (not shown). The average pH_2O dependence is given at the bottom of each of the plots shown in Fig. 8.

3.5. Temperature dependencies

The temperature dependencies of $1/R_{ct}$ and $1/R_{mt}$ for Cu and Pt are shown in Fig. 9.

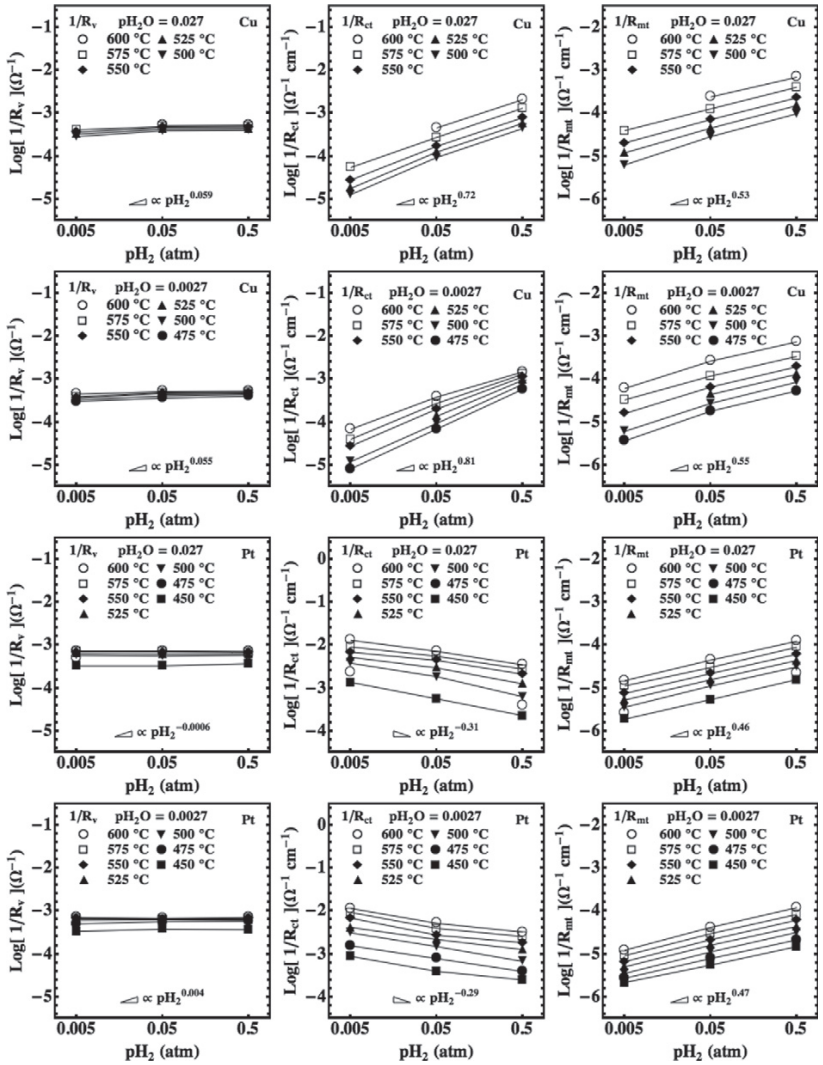

Fig. 7. Cu (*top*) and Pt (*bottom*) point-contact electrode conductance: electrolyte volume (*left*), charge transfer (*middle*), and mass transfer (*right*), plotted as Log(1/*R*) vs. Log(pH_2) for $pH_2O = 0.027$ (*above*) and $pH_2O = 0.0027$ (*below*).

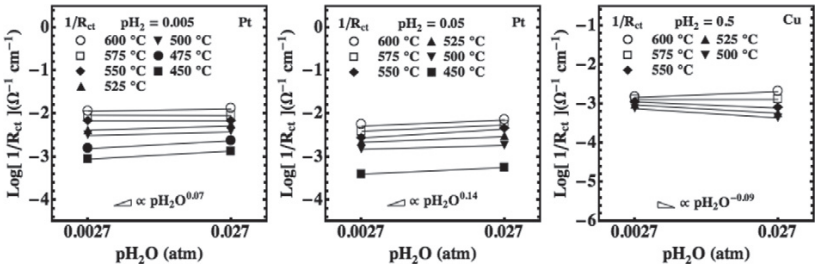

Fig. 8. Selected charge transfer conductances, plotted as Log($1/R$) vs. Log($p\mathrm{H_2O}$) for Pt at $p\mathrm{H_2} = 0.005$ and 0.05 (*left*), and Cu at $p\mathrm{H_2} = 0.5$ (*right*).

The conductance in the studied temperature range can, to a first approximation, be expressed as,

$$\frac{1}{R} = A_0\,(p\mathrm{H_2})^n\,(p\mathrm{H_2O})^m\,\mathbf{e}^{-\frac{\Delta H}{k_b T}} \tag{2}$$

where n and m are the $p\mathrm{H_2}$ and $p\mathrm{H_2O}$ dependencies, respectively. ΔH is the activation enthalpy and k_b is the Boltzmann constant. Log-linear regressions of Eq. (2) were performed on the plots in Fig. 9, and the activation enthalpies were extracted. Table 2 reports the means and standard deviations of the pre-exponential A_0, n and m from Sections 3.3 and 3.4, respectively, as well as the activation enthalpy, ΔH.

Pre-exponentials depend significantly upon geometric factors, concentrations of species and vibrational attempt rates. The difference in the charge transfer pre-exponential of approximately 160 $\Omega^{-1}\mathrm{cm}^{-1}$ for Cu, compared to 1000 $\Omega^{-1}\mathrm{cm}^{-1}$ for Pt, indicates that Cu has fewer available sites for charge transfer to take place. However, the activation enthalpy for charge transfer is lower for Cu than for Pt, indicating the reaction takes place more readily on Cu. Charge transfer reactions on Cu have been reported to have different activation enthalpies for different surface orientations, from approximately 0.5 to 1 eV [37,47–49]. This variation is possibly due to competitive adsorption of H_2 and O_2 vs. H_2O at preferential sites, though this could also be due to the diffusion of hydrogen through the bulk copper lattice at high $p\mathrm{H_2}$. Hydrogen has been previously reported to accumulate just below the surface of Cu and Cu-based metal alloys, forming small hydrogen bubbles [39,50]. Indications of this were also obtained in this study, as seen in Fig. 10, though it is unknown to what extent this contributed to the measured resistance of the Cu-BZCY27 interface.

In a recent DFT study of the Pd-BZY 3pb interface [51] the activation energy for the proton transfer step of the charge transfer reaction was calculated to be near 1 eV, independent of the type of metal electrode used, which is in reasonable agreement with the experimental results for both Cu and Pt, as obtained in this study.

The pre-exponential for mass transfer for Cu is almost 4000 times greater than that of Pt, approximately 10,000 vs. 2.6 $\Omega^{-1}\mathrm{cm}^{-1}$, respectively. The higher activation enthalpy for mass transfer on Cu combines that of hydrogen adsorption, dissociation and surface diffusion, and is within literature values of approximately 1.1 to 1.4 eV [37,48,52–55]. Hydrogen dissociation on Pt surfaces is reported to be nearly non-activated, and the activation enthalpies obtained here are those of hydrogen adsorption, in agreement with literature reports of approximately 0.65 to 0.76 eV [37,56–61]. For Cu, the combination of a higher pre-exponential and activation enthalpy indicates that mass transfer processes are less favorable and use more of the Cu metal surface adjacent to the 3pb for adsorption and dissociation to occur. With a lower pre-exponential and activation enthalpy, mass transfer on Pt is much more favorable, and thus needs less area to complete the process.

4. Discussion

4.1. Hydrogen oxidation reaction model and pH_2 dependencies

An HOR model was developed to explain the characteristics of the data presented in previous sections. Langmuir adsorption theory and Butler-Volmer charge transfer formalism have previously been used to describe electrochemical redox processes on solid-state oxide electrolytes [62,63]. Here, it is assumed that associative adsorption will be predominant, such as the case for Cu, and occur first. However, on Pt, dissociative adsorption is more favorable. Using Langmuir theory, associative and dissociative adsorption are often lumped together, and along with diffusion, are commonly used to describe mass transfer as a single process.

H_2 oxidation half-cell model:

$$1-\text{adsorption}:\ \mathrm{H_2}(g) + v_{ads} \Longleftrightarrow \mathrm{H}_{2,ads} \tag{3}$$

$$2-\text{diffusion}:\ \mathrm{H}_{2,ads} + v_{ads} \Longleftrightarrow 2\mathrm{H}_{ads} \tag{4}$$

$$3a-\text{surface diffusion}:\ \mathrm{H}_{ads} + v_{3pb} \Longleftrightarrow \mathrm{H}_{3pb} + v_{ads} \tag{5}$$

$$3b-\begin{cases}\text{dissolution into metal}:\ \mathrm{H}_{ads} + v_i \Longleftrightarrow \mathrm{H}_i^x + v_{ads}\\ \text{interstitial diffusion}:\ \mathrm{H}_i^x + v_{2pb} \Longleftrightarrow \mathrm{H}_{2pb} + v_i\end{cases} \tag{6}$$

$$4-\text{charge transfer}:\ \mathrm{H}_{pb} + \mathrm{O}_\mathrm{O}^{2-} \Longleftrightarrow \mathrm{OH}_\mathrm{O}^- + e^- + v_{pb} \tag{7}$$

After adsorption onto a vacant surface site, v_{ads}, and the subsequent dissociation, H_{ads} transports to the phase boundary (pb). This may happen via two paths, on the metal surface to the 3pb, or via dissolution into and interstitially through the bulk metal to the 2pb. Charge transfer then takes place at the pb, with proton transfer to an available oxygen ion in the electrolyte, and electron transfer to the metal. Using Langmuir adsorption theory to describe mass transfer processes, and Butler-Volmer formalism for charge transfer, the rate equations according to the proposed HOR model are,

$$r_1 = k_1^+ p\mathrm{H_2}\,(1-\Theta_{ads}) - k_1^-\,\Theta_{ads}^{H_2} \tag{8}$$

$$r_2 = k_2^+\,\Theta_{ads}^{H_2}\,(1-\Theta_{ads}) - k_2^-\left(\Theta_{ads}^{H}\right)^2 \tag{9}$$

$$r_{3s} = k_{surf.}^+\,\Theta_{ads}^{H}\,(1-\Theta_{3pb}) - k_{surf.}^-\,\Theta_{3pb}^{H}\,(1-\Theta_{ads}) \tag{10}$$

$$r_{3i} = \begin{cases}k_{\mathrm{diss}}.^+\Theta_{ads}^{H}\,(1-\Theta_i) - k_{\mathrm{diss}}.^-\Theta_i^{H}\,(1-\Theta_{ads})\\ k_{\mathrm{diff}}.^+\Theta_i^{H}\,(1-\Theta_{2pb}) - k_{\mathrm{diff}}.^-\Theta_{2pb}^{H}\,(1-\Theta_i)\end{cases} \tag{11}$$

$$r_4 = k_4^+\,\Theta_{pb}^{H}\left[\mathrm{O}_0^{2-}\right]\exp^{\beta\zeta(E-E_0)} - \ldots$$
$$\ldots k_4^-\left[\mathrm{OH}_0^-\right](1-\Theta_{pb})\exp^{-(1-\beta)\zeta(E-E_0)} \tag{12}$$

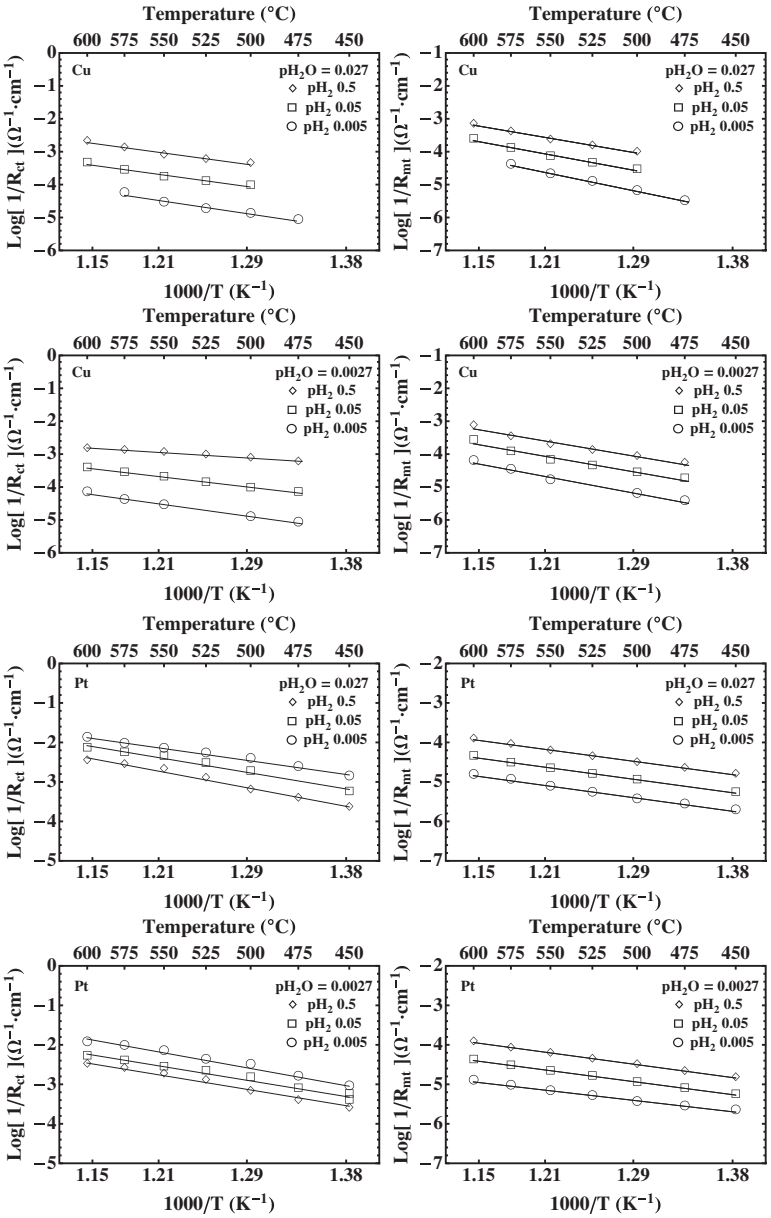

Fig. 9. Plots of Log($1/R_i$) vs. 1000/T for charge transfer (*left*) and mass transfer (*right*) for the Cu (*top*) and Pt (*bottom*) point-contact electrodes at $pH_2O = 0.027$ and 0.0027.

The terms k^+ and k^- are the forward and backward rate constants, respectively. The symbol Θ denotes site fraction and is equivalent to the activity of H; the superscript indicates the H species, and the subscripts *ads*, *i*, 2*pb* and 3*pb* indicate location as "adsorbed", "interstitial", "two-phase boundary" and "three-phase boundary", respectively. In r_3, the k subscript *surf.* is for surface, *diss*. for dissolution and *diff*. for diffusion. $(1 - \Theta)$ then represents the activity of the vacant sites. $[O_O^{2-}]$ and $[OH_O^-]$ are the concentrations of oxide ions and protons in the electrolyte, respectively. From the Butler-Volmer equation, the symmetry coefficient for electron transfer is commonly assumed to be, $\beta = 1/2$. $\zeta = F/RT$ where F is Faraday's constant, R is the universal gas constant, T is temperature. E is the cell potential and E_0 is the standard potential.

Eq. (8) describes the rate of physisorption of H_2 onto the metal surface. Eq. (9) describes the rate of dissociation and chemisorption of atomic hydrogen. Eq. (10) describes the rate of diffusion of atomic hydrogen, H_{ads}, across the metal surface to the 3pb. Eq. (11) describes the rate of dissolution and interstitial diffusion of atomic hydrogen through the bulk metal to the 2pb. Eq. (12) describes the rate of charge transfer, where pb (phase-boundary) denotes both the 2pb and 3pb. In the following treatment we will, for simplicity, assume that the surface process is predominant.

Table 2
Mean and standard deviations ($\bar{x}_i \pm \sigma_i$) of the hydrogen (n_i) and water vapor (m_i) pressure dependencies as obtained from Sections 3.3 and 3.4 for charge transfer (ct) and mass transfer (mt), the activation enthalpies (ΔH_i), as well as the derived pre-exponentials, Log($A_{0,i}$), for each of the Cu and Pt point-contact electrodes.

$\bar{x}_i \pm \sigma_i$	Cu	Pt
n_{ct}	0.77 ± 0.09	−0.30 ± 0.04
m_{ct}	−0.02 ± 0.12	0.08 ± 0.08
ΔH_{ct} (eV)	0.82 ± 0.21	0.93 ± 0.09
Log($A_{0,ct}(\Omega^{-1}\mathrm{cm}^{-1})$)	2.21 ± 0.10	3.00 ± 0.06
n_{mt}	0.53 ± 0.04	0.46 ± 0.02
m_{mt}	0.04 ± 0.04	0.01 ± 0.03
ΔH_d (eV)	1.21 ± 0.09	0.73 ± 0.05
Log($A_{0,mt}(\Omega^{-1}\mathrm{cm}^{-1})$)	4.00 ± 0.13	0.42 ± 0.04

At thermodynamic equilibrium the net rate is 0, and from Eqs. (8–11) with the mass transfer rate constant $\mathbf{K}_{mt} = \sqrt{(k_1^+/k_1^-)\,(k_2^+/k_2^-)(k_3^+/k_3^-)}$, the surface coverage of chemisorbed H at the phase boundary is,

$$\Theta_{pb}^{H} = \mathbf{K}_{mt}\, p\mathrm{H}_2^{1/2}(1-\Theta_{pb}) \tag{13}$$

Eq. (13) is then converted into current through the relation, $i = -nF\, r_{lim} = i_{anodic} - i_{cathodic}$, where r_{lim} is the rate limiting step. In equilibrium, the net current, $i = 0$, and the exchange current density, i_0, follows,

$$i_0 = i_{0,+} = i_{0,-} \tag{14}$$

where $i_{0,+} = i_{0,anodic}$ and $i_{0,-} = i_{0,cathodic}$. At open circuit, the exchange current density is inversely proportional to measured resistance through Ohm's law, $v = iR$. With the low coverage assumption, $(1-\Theta_{pb}) = 1$, the $p\mathrm{H}_2$ dependence of the mass transfer rate limiting case is,

$$i_{0,\,mt} \propto \frac{1}{R_{mt}} \propto p\mathrm{H}_2^{1/2} \tag{15}$$

Eq. (15) reflects the hydrogen pressure dependence of adsorption, dissociation and subsequent transport to the pb, and describes the experimentally observed $p\mathrm{H}_2$ dependence of mass transfer for both metals.

Next, consider rate Eq. (12) of the H_2 oxidation half-cell model. With the definition of electrochemical potential as,

$$\tilde{\mu}_i = \mu_i^0 + RT\ln(\chi_i) + zF\phi_i$$

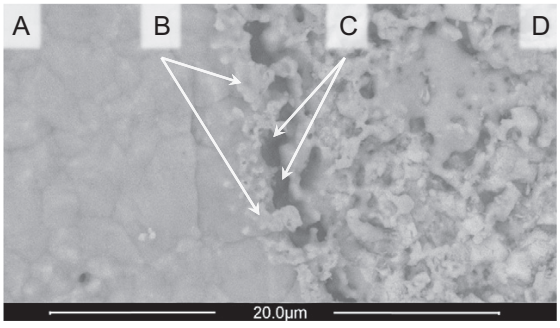

Fig. 10. Post-testing SEM image of the Cu point-contact electrode which on the left shows: A) the grains of the metal surface, with B) the 3pb interface. To the right of the 3pb interface shows: C) vacant areas under the surface of the metal, and D) the irregular 2pb metal-electrolyte interface where hydrogen bubbles may have also formed.

where μ_i^0 is the standard chemical potential, χ is activity, z is charge and ϕ_i is the electric potential of species i. Similar to other derivations of the hydrogen electrode potential [64,65], Eq. (12) then becomes,

$$\begin{aligned}\mu^0_{\Theta^H_{pb}} + RTln\left(\Theta^H_{pb}\right) + \mu^0_{O_O^{2-}} + RTln\left(\left[O_O^{2-}\right]\right) = \ldots\\ \ldots\,\mu^0_{OH_O^-} + RTln\left([OH_O^-]\right) + F\phi_{OH_O^-} + \mu^0_{e^-} - \ldots\\ \ldots F\phi_{e^-} + RTln(1-\Theta_{pb})\end{aligned} \tag{16}$$

with the changes in the cell and standard potentials as,

$$\Delta\phi = \phi_{e^-} - \phi_{OH_O^-}$$

and

$$\Delta\phi^0 = \frac{-\mu^0_{\Theta^H_{pb}} - \mu^0_{O_O^{2-}} + \mu^0_{OH_O^-} + \mu^0_{e^-}}{F} \tag{17}$$

finally yielding the half cell potential of the hydrogen electrode,

$$\Delta\phi - \Delta\phi^0 = E_{eq} - E^0 = \frac{1}{\zeta}\ln\left(\frac{[OH_O^-](1-\Theta_{pb})}{\Theta^H_{pb}[O_O^{2-}]}\right) \tag{18}$$

By defining the concentrations of products, $C_P = [OH_O^-](1-\Theta_{pb})$, and reactants, $C_R = \Theta^H_{pb}[O_O^{2-}]$. Then inserting Eq. (18) into Eq. (12) where at equilibrium the cell potential $E = E_{eq}$.

$$\begin{aligned}r_{4,eq} = k_4^0\, C_R\, \exp^{\beta\zeta\left(\frac{1}{\zeta}\ln\left(\frac{C_P}{C_R}\right)\right)} = \ldots\\ \ldots k_4^0\, C_P\, \exp^{-(1-\beta)\zeta\left(\frac{1}{\zeta}ln\left(\frac{C_P}{C_R}\right)\right)}\end{aligned} \tag{19}$$

Again using $i = -nFr$ with $n = 1$, the exchange current density is now defined in terms of both reactants and products,

$$i_0 = Fk_4^0\, C_R^{(1-\beta)}\, C_P^{\beta} \tag{20}$$

It is reasonable to assume that in a fully hydrated and protonated electrolyte, $[OH_O^-]$ is constant, and that the concentration of oxygen ions in the perovskite structure ABO_3 is approximately equal to unity, $[O_O^{2-}] \approx 1$. After simplification with C_P, C_R, Eq. (13) and the heterogeneous rate constant, $\mathbf{K}_h^0 = k_4^0\mathbf{K}_{mt}$,

$$i_{0,r_4} = F\,\mathbf{K}_h^0\, p\mathrm{H}_2^{\frac{(1-\beta)}{2}}(1-\Theta_{pb}) \tag{21}$$

or more significantly,

$$i_{0,ct} \propto \frac{1}{R_{ct}} \propto p\mathrm{H}_2^{\frac{(1-\beta)}{2}}(1-\Theta_{pb}) \tag{22}$$

The charge transfer conductance, $1/R_{ct}$, then scales as the product of the $p\mathrm{H}_2$ dependence obtained from mass transfer, the charge transfer symmetry coefficient and the activity of vacant sites at the pb.

Pt dissociatively adsorbs hydrogen, which may then segregate at the terminations of surfaces [66]. This will yield high coverage at corners and edges, such as the 3pb. By using the Langmuir isotherm describing high coverage with dissociative adsorption as $(1-\Theta_{3pb}) = p\mathrm{H}_2^{-1/2}$ in Eq. (21),

$$i_{0,ct} \propto \frac{1}{R_{ct}} \propto p\mathrm{H}_2^{-1/4} \tag{23}$$

Then the $p\mathrm{H}_2^{-1/4}$ charge transfer hydrogen pressure dependence describing the experimental results for Pt is obtained directly.

Cu is not known to have high surface coverage of hydrogen [67,68]. In the low pO_2 of the H_2–H_2O atmospheres used, Cu does not form the a stable Cu_2O phase, however, it is proposed that most of the active sites at the 3pb are occupied by adsorbed oxygen. This causes an additional step in the charge transfer reaction. At the 3pb, H_{ads} will first reduce the oxygen at a 3pb site in order to become the H_{3pb} species,

$$3H_{ads} + O_{3pb} \Longleftrightarrow H_{3pb} + H_2O(g) + 3v_{ads} \tag{24}$$

The rate equation associated with Eq. (24) is,

$$r = k^{+}\left(\Theta_{ads}^{H}\right)^{3}\Theta_{3pb}^{O} - k^{-}\Theta_{3pb}^{H}\,pH_2O\,(1-\Theta_{ads})^{3} \tag{25}$$

Which then yields the H_{3pb} coverage as,

$$\Theta_{3pb}^{H} = \mathbf{K}_{mt}\,pH_2^{3/2}\frac{\Theta_{3pb}^{O}}{pH_2O}\,(1-\Theta_{3pb}) \tag{26}$$

and with a constant proportional pH_2O and Θ_{3pb}^{O}, yields the exchange current density as,

$$i_{0,r4} = F\,\mathbf{K}_h^0\,pH_2^{\frac{3(1-\beta)}{2}}\,(1-\Theta_{3pb}) \tag{27}$$

Again with $\beta = 0.5$, and the low coverage of $(1-\Theta_{3pb}) = 1$,

$$i_{0,ct} \propto \frac{1}{R_{ct}} \propto pH_2^{3/4} \tag{28}$$

Then the $pH_2^{3/4}$ hydrogen pressure dependence is obtained, which describes the experimental results herein.

In this section pH_2 dependencies and hypotheses have been presented that describe the mass transfer and charge transfer data obtained in this metal point-contact electrode study. The mass transfer processes of hydrogen adsorption, dissociation and diffusion, emphasizing low coverage for both Cu and Pt, display a $pH_2^{1/2}$ dependency. The pH_2 dependencies derived for charge transfer are influenced by the symmetry coefficient, β, and by the coverage of atomic hydrogen at the 3pb, H_{3pb}, which may differ significantly from the overall surface coverage of the metal. First, for Pt, with high 3pb coverage, a $pH_2^{-1/4}$ dependence was derived. Second, for Cu, with the hypothesis of adsorbed oxygen at active 3pb sites due to the water-vapor containing atmosphere, and a low hydrogen coverage assumption, the $pH_2^{3/4}$ dependence was obtained.

5. Conclusions

The reaction kinetics of Pt and Cu point-contact electrodes on a BZCY72 electrolyte were studied over a range of temperatures and hydrogen pressures using impedance spectroscopy. The charge transfer hydrogen pressure dependencies were $pH_2^{3/4}$ for Cu, attributed to a high occupancy of adsorbed oxygen at three-phase boundary sites in the water-vapor containing atmosphere, and $pH_2^{-1/4}$ for Pt, corresponding to a hydrogen saturated interface. The activation enthalpies for charge transfer are similar for both metals, 0.82 eV for Cu, and 0.93 eV for Pt. Cu and Pt exhibit pre-exponentials of 160 $\Omega^{-1}cm^{-1}$ vs. 1000 $\Omega^{-1}cm^{-1}$, respectively. Mass transfer exhibited a $pH_2^{1/2}$ dependency for both metals. The activation enthalpy for mass transfer is higher for Cu than Pt, 1.21 eV vs. 0.73 eV, respectively, reflecting that mass transfer is a slower process on Cu. The pre-exponentials for mass transfer of approximately 10000 $\Omega^{-1}cm^{-1}$ for Cu and 2.6 $\Omega^{-1}cm^{-1}$ for Pt, also indicate that for Cu, this process likely takes place on a larger geometric area adjacent to the 3pb than the same process on Pt. It is concluded from this work that although Cu is a suitable candidate electrode material for hydrocarbon applications due to it's resistance to carbon deposition, pure Cu suffers from poor catalytic activity for the hydrogen oxidation reaction. In order to perform efficiently, it is suggested that Cu would benefit from modifications via alloying, or through the addition of another phase that is catalytically active towards hydrogen dissociation.

Acknowledgments

The authors gratefully acknowledge financial support from the Research Council of Norway through the program NANO2021, RoMA, project number 219194. We also thank Drs. Nahum M. Carcases, Ragnar Strandbakke, Einar Vøllestad, and Min Chen for valuable contributions.

References

[1] H. Iwahara, T. Esaka, H. Uchida, N. Maeda, Proton conduction in sintered oxides and its application to steam electrolysis for hydrogen production, Solid State Ionics 3/4 (1981) 359–363.
[2] H. Iwahara, H. Uchida, S. Tanaka, High temperature type proton conductor based on $SrCeO_3$ and its application to solid electrolyte fuel cells, Solid State Ionics 9-10 (1983) 1021–1026.
[3] H. Iwahara, Proton conducting ceramics and their applications, Solid State Ionics 86-88 (1996) 9–15.
[4] K.D. Kreuer, Proton-conducting oxides, Annu. Rev. Mater. Res. 33 (1) (2003) 333–359.
[5] Y. Larring, T. Norby, Protons in rare earth oxides, Solid State Ionics 77 (1995) 147–151.
[6] Y. Larring, T. Norby, The equilibrium between water vapour, protons, and oxygen vacancies in rare earth oxides, Solid State Ionics 97 (1-4) (1997) 523–528.
[7] K.D. Kreuer, Aspects of the formation and mobility of protonic charge carriers and the stability of perovskite-type oxides, Solid State Ionics 125 (1-4) (1999) 285–302.
[8] N. Bonanos, Oxide-based protonic conductors: point defects and transport properties, Solid State Ionics 145 (2001) 265–274.
[9] J. Li, J.L. Luo, K.T. Chuang, A.R. Sanger, Chemical stability of Y-doped $Ba(Ce,Zr)O_3$ perovskites in H_2S-containing H_2, Electrochim. Acta 53 (10) (2008) 3701–3707.
[10] L. Kang, Ceramic Membranes for Separation and Reaction, John Wiley & Sons Ltd, England, 2007. ISBN 978-0-470-01440
[11] S. Ricote, G. Caboche, O. Heintz, Synthesis and proton incorporation in $BaCe_{0.9-x}Zr_xY_{0.1}O_{3-\delta}$, J. Appl. Electrochem. 39 (2009) 553–557.
[12] S. Ricote, N. Bonanos, G. Caboche, Water vapour solubility and conductivity study of the proton conductor $BaCe_{0.9-x}Zr_xY_{0.1}O_{3-\delta}$, Solid State Ionics 180 (14–16) (2009) 990–997.
[13] S. Ricote, N. Bonanos, M.C. Marco de Lucas, G. Caboche, Structural and conductivity study of the proton conductor $BaCe_{0.9-x}Zr_xY_{0.1}O_{3-\delta}$ at intermediate temperatures, J. Power Sources 193 (2009) 189–193.
[14] Y. Lin, R. Ran, Y. Guo, W. Zhou, R. Cai, J. Wang, Z. Shao, Proton-conducting fuel cells operating on hydrogen, ammonia and hydrazine at intermediate temperatures, Int. J. Hydrog. Energy 35 (7) (2010) 2637–2642.
[15] E. Fabbri, L. Bi, H. Tanaka, D. Pergolesi, E. Traversa, Chemically stable Pr and Y co-doped barium zirconate electrolytes with high proton conductivity for intermediate-temperature solid oxide fuel cells, Adv. Funct. Mater. 21 (2011) 158–166.
[16] K. Ryu, S. Haile, Chemical stability and proton conductivity of doped $BaCeO_3$ - $BaZrO_3$ solid solutions, Solid State Ionics 125 (1999) 355–367.
[17] E. Fabbri, A. D'Epifanio, E. Di Bartolomeo, S. Licoccia, E. Traversa, Tailoring the chemical stability of $BaCe_{0.8-x}Zr_xY_{0.2}O_{3-\delta}$ protonic conductors for intermediate temperature solid oxide fuel cells (IT-SOFCs), Solid State Ionics 179 (15–16) (2008) 558–564.
[18] M.D. Gross, J.M. Vohs, R.J. Gorte, A study of thermal stability and methane tolerance of Cu-based SOFC anodes with electrodeposited Co, Electrochim. Acta 52 (5) (2007) 1951–1957.
[19] S.W. Jung, J.M. Vohs, R.J. Gorte, Preparation of SOFC anodes by electrodeposition, J. Electrochem. Soc. 154 (12) (2007) B1270–B1275.
[20] O. Costa-Nunes, R.J. Gorte, J.M. Vohs, Comparison of the performance of Cu-CeO_2-YSZ and Ni-YSZ composite SOFC anodes with H_2, CO, and syngas, J. Power Sources 141 (2005) 241–245.
[21] V.K. Venkatesan, S. McIntosh, R.J. Gorte, J.M. Vohs, Measurement of electrode overpotentials for direct hydrocarbon conversion fuel cells, Solid State Ionics 166 (1 - 2) (2004) 191–197.
[22] S. Park, J.M. Vohs, R.J. Gorte, Direct oxidation of hydrocarbons in a solid-oxide fuel cell, Nature 404 (6775) (2000) 265–267.
[23] R.J. Gorte, S. Park, J.M. Vohs, C. Wang, Anodes for direct oxidation of dry hydrocarbons in a solid-oxide fuel cell, Adv. Mater. 12 (19) (2000) 1465–1469.

I

[24] R.J. Gorte, J.M. Vohs, S. McIntosh, Recent developments on anodes for direct fuel utilization in SOFC, Solid State Ionics 175 (1 - 4) (2004) 1–6.
[25] S.J. Gentry, J.G. Firth, A. Jones, Catalytic oxidation of hydrogen over platinum, J Chem Soc, Faraday Trans 1 70 (1974) 600–604.
[26] S.P. Jiang, S.P.S. Badwal, Hydrogen oxidation at the nickel and platinum electrodes on yttria? Tetragonal zirconia electrolyte, J. Electrochem. Soc. 144 (11) (1997) 3777–3784.
[27] D. Kek, N. Bonanos, Investigation of hydrogen oxidation reaction on a metal/perovskite proton conductor interface by impedance spectroscopy, Vacuum 61 (2001) 453–457.
[28] D. Kek, N. Bonanos, M. Mogensen, S. Pejovnik, Effect of electrode material on the oxidation of H_2 at the metal - $Sr_{0.995}Ce_{0.95}Y_{0.05}O_{2.970}$ interface, Solid State Ionics 131 (2000) 249–259.
[29] T. Horita, N. Sakai, H. Yokokawa, M. Dokiya, T. Kawada, Characterization of ceria coated YSZ by a platinum point electrode in H_2-H_2O atmosphere, Solid State Ionics 86 - 88, Part 2 (1996) 1259–1266.
[30] T. Jacobsen, B. Zachau-Christiansen, L. Bay, M.J. Jørgensen, Hysteresis in the solid oxide fuel cell cathode reaction, Electrochim. Acta 46 (7) (2001) 1019–1024.
[31] F. Mauvy, C. Lalanne, S. Fourcade, J.M. Bassat, J.C. Grenier, Impedance spectroscopy study of $Nd_2NiO_{4+\delta}$, LSM and platinum electrodes by micro-contact technique, J. Eur. Ceram. Soc. 27 (13 - 15) (2007) 3731–3734.
[32] T. Horita, H. Kishimoto, K. Yamaji, Y. Xiong, N. Sakai, M.E. Brito, H. Yokokawa, Materials and reaction mechanisms at anode/electrolyte interfaces for SOFCs, Solid State Ionics 177 (19 - 25) (2006) 1941–1948.
[33] W.G. Bessler, M. Vogler, H. Stormer, D. Gerthsen, A. Utz, A. Weber, E. Ivers-Tiffee, Model anodes and anode models for understanding the mechanism of hydrogen oxidation in solid oxide fuel cells, Phys Chem Chem Phys 12 (2010) 13888–13903.
[34] M. Mogensen, S. Skaarup, Kinetic and geometric aspects of solid oxide fuel cell electrodes, Solid State Ionics 86–88 (1996) 1151–1160.
[35] E.J.L. Schouler, M. Kleitz, Electrocatalysis and inductive effects at the gas, Pt/stabilized zirconia interface, J. Electrochem. Soc. 134 (5) (1987) 1045–1050.
[36] B. Hammer, J.K. Nørskov, Theoretical surface science and catalysis—calculations and concepts, in: B.C. Gates, H. Knozinger (Eds.), Impact of Surface Science on Catalysis, Advances in Catalysis vol. 45, Academic Press. 2000, pp. 71–129.
[37] P.B. Rasmussen, P.M. Holmblad, H. Christoffersen, P.A. Taylor, I. Chorkendorff, Dissociative adsorption of hydrogen on Cu(100) at low temperatures, Surface Science 287-288, Part 1 (0) (1993) 79–83.
[38] T. Ishikawa, R.B. McLellan, The diffusivity of hydrogen in copper at low temperatures, J. Phys. Chem. Solids 46 (4) (1985) 445–447.
[39] H.B. Zhou, Y. Zhang, X. Ou, Dissolution and diffusion behaviors of hydrogen in copper: a first-principles investigation, Comput. Mater. Sci. 79 (2013) 923–928.
[40] H. Horinouchi, M. Shinohara, T. Otsuka, K. Hashizume, T. Tanabe, Determination of hydrogen diffusion and permeation coefficients in pure copper at near room temperature by means of tritium tracer techniques, J. Alloys Compd. 580, Supplement 1 (2013) S73–S75.
[41] P. Babilo, S.M. Haile, Enhanced Sintering of yttrium-doped barium zirconate by addition of ZnO, J. Am. Ceram. Soc. 88 (9) (2005) 2362–2368.
[42] S. Nikodemski, J. Tong, R. O'Hayre, Solid-state reactive sintering mechanism for proton conducting ceramics, Solid State Ionics 253 (0) (2013) 201–210.
[43] S. Ricote, G. Caboche, C. Estournes, N. Bonanos, Synthesis, sintering, and electrical properties of $BaCe_{0.9x}Zr_xY_{0.1}O_{3-\delta}$, J. Nanomater. 2008 (2008) 1–6.
[44] Y. Yamazaki, R. Hernandez-Sanchez, S.M. Haile, High total proton conductivity in large-grained yttrium-doped barium zirconate, Chem. Mater. 21 (13) (2009) 2755–2762.
[45] J.H. Hwang, K.S. Kirkpatrick, T.O. Mason, E.J. Garboczi, Experimental limitations in impedance spectroscopy: Part IV. Electrode contact effects, Solid State Ionics 98 (1-2) (1997) 93–104.
[46] J.T.S. Irvine, D.C. Sinclair, A.R. West, Electroceramics: characterization by impedance spectroscopy, Advanced Materials 2 (3) (1990) 132–138.
[47] M.F. Luo, D.A. MacLaren, I.G. Shuttleworth, W. Allison, Preferential sub-surface occupation of atomic hydrogen on Cu(111), Chem. Phys. Lett. 381 (5–6) (2003) 654–659.
[48] J. Strömquist, L. Bengtsson, M. Persson, B. Hammer, The dynamics of H absorption in and adsorption on Cu(111), Surface Science 397 (1–3) (1998) 382–394.
[49] M.F. Luo, D.A. MacLaren, W. Allison, Migration and abstraction of H-atoms from the Cu(111) surface, Surface Science 586 (1-3) (2005) 109–114.
[50] Å. Martinsson, R. Sandström, Hydrogen depth profile in phosphorus-doped, oxygen-free copper after cathodic charging, J. Mater. Sci. 47 (19) (2012) 6768–6776.
[51] M. Malagoli, M.L. Liu, H.C. Park, A. Bongiorno, Protons crossing triple phase boundaries based on a metal catalyst, Pd or Ni, and barium zirconate, Phys Chem Chem Phys 15 (2013) 12525–12529.
[52] P.K. Johansson, Chemisorption of molecular hydrogen on simple metal surfaces, Surface Science 104 (2) (1981) 510–526.
[53] D.J. Auerbach, C.T. Rettner, H.A. Michelsen, Interaction dynamics of hydrogen at a Cu(111) surface, Surface Science 283 (1–3) (1993) 1–8.
[54] B.E. Hayden, C.L.A. Lamont, Coupled translational-vibrational activation in dissociative hydrogen adsorption on Cu(110), Phys Rev Lett 63 (1989) 1823–1825.
[55] R.C. Mowrey, G.J. Kroes, G. Wiesenekker, E.J. Baerends, Dissociative adsorption of H_2 on Cu(100): a four-dimensional study of the effect of rotational motion on the reaction dynamics, J. Chem. Phys. 106 (10) (1997) 4248–4259.
[56] R. Lewis, R. Gomer, Adsorption of hydrogen on platinum, Surface Science 17 (2) (1969) 333–345.
[57] W.T. Lee, L. Ford, P. Blowers, H.L. Nigg, R.I. Masel, Why do heats of adsorption of simple gases on platinum surfaces vary so little with surface structure? Surface Science 416 (1–2) (1998) 141–151.
[58] B. Klötzer, E. Bechtold, Hydrogen adsorption and the transformation of the Pt(100) surface structure, Surface Science 295 (3) (1993) 374–384.
[59] P.R. Norton, P.J. Richards, The heat of adsorption of hydrogen on platinum, Surface Science 44 (1) (1974) 129–140.
[60] W.H. Weinberg, R.P. Merrill, Crystal field surface orbital - Bond-energy bond-order (CFSO-BEBO) model for chemisorption: application to hydrogen adsorption on a platinum (111) surface, Surface Science 33 (3) (1972) 493–515.
[61] J. Andzelm, Molecular orbital study of the chemisorption of hydrogen on platinum surfaces, Surface Science 108 (3) (1981) 561–577.
[62] J.D. Kim, G.D. Kim, J.W. Moon, Y.I. Park, W.H. Lee, K. Kobayashi, M. Nagai, C.E. Kim, Characterization of LSM-YSZ composite electrode by ac impedance spectroscopy, Solid State Ionics 143 (3-4) (2001) 379–389.
[63] T. Hosoi, T. Yonekura, K. Sunada, K. Sasaki, Exchange current density of SOFC electrodes: theoretical relations and partial pressure dependencies rate-determined by electrochemical reactions, J. Electrochem. Soc. 162 (1) (2015) F136–F152.
[64] H. Gerischer, The CRC Handbook of Solid State Electrochemistry, CRC Press. 1997.
[65] R. O'Hayre, S.W. Cha, W. Colella, F.B. Prinz, Fuel Cell Fundamentals, 2 Ed. ed., Wiley. 2009.
[66] A. Pundt, R. Kirchheim, Hydrogen in metals: microstructural aspects, Annu. Rev. Mater. Res. 36 (1) (2006) 555–608.
[67] P. Sandl, U. Bischler, E. Bertel, The interaction of atomic hydrogen with Cu(110), Surface Science 291 (1) (1993) 29–38.
[68] D.R. Rossington, S.J. Holden, Equilibrium coverage of copper by chemisorbed hydrogen, Nature 199 (4893). (1963) 589–589.

6 Summarizing Discussion and Further Results

The manuscripts presented in this dissertation address both the fundamental theory of the HOR for proton conducting oxides, as well as the development of a Cu-based electrode intended for use with BZCY72 in industrial applications in carbonaceous atmospheres. Manuscript I (MI) addressed the fundamental understanding of the hydrogen oxidation reaction on proton ceramics by developing a simplified HOR model and comparing the kinetics of Cu and Pt point-contact electrodes. Manuscript II (MII) then expanded this understanding by comparing the effects of the catalytic CeO_2 surface modification on a thermally stable Cu-Co composition. Manuscripts III (MIII) and IV (MIV) reported the fabrication and performance of two different backbone architectures: a co-sintered macro-porous skeletal microstructure infiltrated with the Cu-Co composition and modified with CeO_2, and a graded porosity functional microstructure infiltrated with the multi-phase Cu-Co-CeO_2 composition.

This section will summarize the key findings and developments of this work, and aims to further discuss the individual manuscripts by connecting them in a broader context. Additionally, other results not presented in the manuscripts will also be included, as they are relevant to continued aspects of this effort.

6.1 HOR Model

$p\mathrm{H}_2$ dependencies

The simplified HOR model developed in Sec. 2.3 (and MI) describes the anodic hydrogen electrode reaction as a sequence of elementary steps. It is summarized by showing that the rate constant for the mass transfer process, $\mathbf{K}_{mt}$ (including adsorption, $\mathbf{K}_{ads}$, dissociation, $\mathbf{K}_{diss}$ and diffusion, $\mathbf{K}_{diff}$), is embedded within that of the charge transfer process, $\mathbf{K}_{ct}$. This global process, also summarized in MII, is shown in (6.1),

$$\overbrace{\mathrm{H_2\,(g)} \overset{\mathbf{K}_{ads}}{\Leftrightarrow} \mathrm{H_{2,}}_{ads} \overset{\mathbf{K}_{diss}}{\Leftrightarrow} 2\mathrm{H}_{ads} \overset{\mathbf{K}_{diff}}{\Leftrightarrow} 2\mathrm{H}_{3pb}}^{\mathbf{K}_{mt}} \overbrace{\overset{\mathbf{K}_{mt}}{\Longleftrightarrow} 2(\mathrm{H}_{3pb} + \mathrm{O}_O^{2-} \Leftrightarrow \mathrm{OH}_\mathrm{O}^- + e^-)}^{\mathbf{K}_{ct}} \tag{6.1}$$

Electrode conductances are described as functions of the hydrogen pressure, $p\mathrm{H}_2$, the availability of vacant sites, $(1-\Theta_i)$, and the rate constants, $\mathbf{K}_{mt}$ and $\mathbf{K}_{ct}$, which are related to material specific parameters.

$$\text{A)}\ \frac{1}{R_{mt}} \propto \mathbf{K}_{mt}\, p\mathrm{H}_2^{1/x}\,(1-\Theta_{ads}) \qquad \text{B)}\ \frac{1}{R_{ct}} \propto \mathbf{K}_{ct}\, p\mathrm{H}_2^{\frac{1-\beta}{2}}\,(1-\Theta_{tpb}) \tag{6.2}$$

In (6.2A), for mass transfer, $x = 1$ for processes rate limited by adsorption, and $x = 2$ for processes rate limited by dissociation. In (6.2B), the charge transfer symmetry

coefficient is often assumed to be $\beta = 0.5$. At low coverages, Θ is small and $(1-\Theta) \approx 1$, then $1/R_{mt} \propto p\mathrm{H}_2$ or $p\mathrm{H}_2^{1/2}$, for adsorption or dissociation limited cases, respectively, and then $1/R_{ct} \propto p\mathrm{H}_2^{1/4}$ for either case. At high coverage, the activity of vacant sites is approximated by (6.3),

$$(1 - \Theta_{ads}) \approx \frac{1}{\mathbf{K}_{ads}\, p\mathrm{H}_2^{1/x}} \tag{6.3}$$

Then $1/R_{mt}$ is independent of $p\mathrm{H}_2$, and $1/R_{ct} \propto p\mathrm{H}_2^{-1/4}$. This simplified HOR model was used to interpret results in MI-MIII, and described the experimentally obtained $p\mathrm{H}_2$ dependencies well. Table 6.1 first shows the predicted bounds of $p\mathrm{H}_2$ dependencies for charge and mass transfer, and then the $p\mathrm{H}_2$ dependencies as obtained in this work. All but one of the results were found to be close to the predicted values. Based on small deviations away from the thermodynamically predicted $p\mathrm{H}_2$ dependencies, certain assumptions can be made about surface and 3pb coverages. Though the $p\mathrm{H}_2$ dependencies shown in Table 6.1 fall within the bounds predicted by the model, many of them are open to different interpretations based on different coverages and adsorption mechanisms, such as in MII.

Table 6.1: The HOR model predicted range of $p\mathrm{H}_2$ dependencies for $1/\mathrm{R}_{ct}$ and $1/\mathrm{R}_{mt}$, and experimentally obtained $p\mathrm{H}_2$ dependencies as reported in MI-MIII.

HOR model predicted range of $p\mathrm{H}_2^x$ dependencies

$1/\mathrm{R}_{ct}$: $-1/4 \leq x \leq 1/4$ $\quad$ $1/\mathrm{R}_{mt}$: $0 \leq x \leq 1$

Manuscript I

Electrode	V (mV)	$1/R_{ct}$	$1/R_{mt}$
Cu	OCV	0.77±0.09	0.53±0.04
Pt		-0.30 ±0.04	0.46±0.02

Manuscript II

Electrode	V (mV)	$1/R_{ct}$	$1/R_{mt}$	Electrode	V (mV)	$1/R_{ct}$	$1/R_{mt}$
CeO_2 Coated Cu-Co	OCV	0.15±0.04	0.43±0.02	Uncoated Cu-Co	OCV	0.08±0.05	0.21±0.02
	100	0.20±0.03	0.65±0.05		100	0.10±0.04	0.31±0.03
	200	0.23±0.04	0.95±0.07		200	0.14±0.02	0.47±0.02

Manuscript III

Electrode	V (mV)	$1/R_{ct}$	$1/R_{mt}$
Cu-Co	-100	0.28±0.01	0.55±0.06
	OCV	0.27±0.02	0.57±0.05
	100	0.27±0.01	0.74±0.03

Temperature dependencies

The temperature dependencies of the electrode conductances are of Arrhenius form, and have been approximated by,

$$\frac{1}{R} = A_0 \, (pH_2)^n \, (pH_2O)^m \, \mathbf{e}^{-\frac{\Delta H}{k_b T}} \tag{6.4}$$

Activation enthalpies, ΔH, were extracted from plots of $\mathrm{Log}(1/R_i)$ ($\Omega^{-1}\,\mathrm{cm}^{-2}$) vs. 1000/T ($\mathrm{K}^{-1}$) for charge and mass transfer, providing information about the energy requirements of the different processes. Table 6.2 displays the charge and mass transfer activation enthalpies obtained in MI-MIV, where for ΔH_{mt} two groupings are observed, one from 1.16 to 1.34 eV, and another from 0.6 to 0.9 eV. Differing activation enthalpies

Table 6.2: Activation enthalpies, ΔH_i (eV), for the charge and mass transfer conductances, $1/\mathrm{R}_{ct}$ and $1/\mathrm{R}_{mt}$, from MI-MIV.

Manuscript I

Electrode	V (mV)	ΔH_{ct}	ΔH_{mt}
Cu	OCV	0.82±0.21	1.21±0.09
Pt		0.93±0.09	0.73±0.05

Manuscript II

Electrode	V (mV)	ΔH_{ct}	ΔH_{mt}	Electrode	V (mV)	ΔH_{ct}	ΔH_{mt}
CeO_2 Coated Cu-Co	OCV	0.93±0.07	0.81±0.04	Uncoated Cu-Co	OCV	1.06±0.10	0.89±0.04
	100	1.14±0.03	1.16±0.09		100	1.22±0.08	0.82±0.06
	200	1.26±0.07	1.34±0.13		200	1.30±0.04	0.86±0.04

Manuscript III

Electrode	V (mV)	ΔH_{ct}	ΔH_{mt}
Cu-Co	-100	0.78±0.02	0.75±0.11
	OCV	0.81±0.03	0.84±0.08
	100	0.87±0.03	1.01±0.06

Manuscript IV

T_{max}	ΔH_{ct}	ΔH_{mt}
725 °C (OCV)	1.07±0.02	1.34±0.02
825 °C (≤650 °C)	0.87±0.01	0.60±0.01
825 °C (≥675 °C)	1.70±0.01	

for mass transfer are indicative of different mechanisms, where the higher range reflects dissociative adsorption, and the lower range is characteristic of the dissociation of adsorbed molecular hydrogen. At OCV, the charge transfer activation enthalpies are primarily grouped around 1 eV, in agreement with the predicted energy requirement for the proton transfer step on BZY, and independent of the type of metal catalyst. As will be shown, when used in combination with $p\mathrm{H}_2$ dependencies, activation enthalpies can provide deeper insight into reaction mechanisms.

Reaction mechanisms

Central to MI, and to the development of the model therein, was the determination that the hydrogen coverage on the surface of the electrode in the region *near* the 3pb can be significantly different from that *at* electrochemically active 3pb sites. This is most apparent for the Pt point electrode, as seen in Table 6.1, where the mass transfer $p\mathrm{H}_2^{1/2}$ and charge transfer $p\mathrm{H}_2^{-1/4}$ dependencies are strong indicators of different site coverages, with low and high coverage at adsorption and 3pb sites, respectively. This effect was attributed both to the high catalytic activity of Pt metal, where hydrogen dissociation has an activation enthalpy of 0.65 to 0.76 eV, and that H species tend to segregate at edges and dislocations.

Cu-Co bimetallic anodes have a higher catalytic activity than Cu alone, and to increase the reactivity even further, $\mathrm{CeO_2}$ has been included as an electrocatalyst. This is known to lead to a significant decrease in the polarization resistance, but the effects on the hydrogen oxidation mechanism are not widely reported. MII utilized $\mathrm{CeO_2}$ at the 3pb interface to facilitate charge transfer, and investigated the effects of a surface coating of $\mathrm{CeO_2}$ on the mass transfer process of the Cu-Co composition. The results presented $p\mathrm{H_2}$ dependencies that are not straight forward to analyze. Upon casual inspection of the impedance spectra presented in MII, Fig. 3, it is observed that the polarization ASR ($\Omega\,\mathrm{cm}^2$) of the $\mathrm{CeO_2}$ electrode is roughly half of that of the uncoated electrode, and appears to be dominated by a charge transfer contribution.

At open circuit, the activation enthalpies for charge and mass transfer are equivalent between the two electrodes, and correspond to proton transfer and the dissociation of adsorbed hydrogen, respectively, and thus $p\mathrm{H_2}$ dependencies of $p\mathrm{H}_2^{1/4}$ and $p\mathrm{H}_2^{1/2}$ are predicted for charge and mass transfer, respectively. Without the preceding information, the obtained $p\mathrm{H_2}$ dependencies alone could be misleading. By comparing the $p\mathrm{H_2}$ dependencies of the coated and uncoated electrodes, it is seen that both electrodes have elevated coverages, but the lower $p\mathrm{H}_2^n$ values for the uncoated electrode indicate it has higher hydrogen coverages than the $\mathrm{CeO_2}$ coated electrode.

At a 200 mV anodic bias, the $p\mathrm{H_2}$ dependencies for the $\mathrm{CeO_2}$ coated electrode are indicative of a total process that is rate limited by dissociative adsorption, with low coverages both on the surface and at the 3pb. The $p\mathrm{H}_2^{1/2}$ dependency of the uncoated electrode is indicative of a mass transfer process that is rate limited by dissociation, and the charge transfer $p\mathrm{H}_2^{1/7}$ dependency then indicates an elevated coverage at the 3pb. This analysis is confirmed by the activation enthalpies of each electrode for both charge and mass transfer.

To summarize, $\mathrm{CeO_2}$ primarily impacts chemical mass transfer through the promotion of hydrogen dissociation. However, this effect is most evident in the charge transfer

response, where the high atomic H activity at the 3pb significantly reduces the charge transfer resistance. The lower surface catalytic activity of the uncoated electrode results in an apparent elevated hydrogen coverage at both adsorption and 3pb sites, though these sites must then be populated primarily by molecular hydrogen, as exhibited by slightly higher activation enthalpies for charge and mass transfer. A site requirement argument also supports this hypothesis; if the 3pb has a high coverage of molecular hydrogen, the neighboring sites required for dissociation are unavailable, and thus increase the ASR as observed. This supports the concept that charge and mass transfer are intimately coupled processes through reactant concentration, and inseparable even with higher frequency equilibrium perturbations.

Infiltrated backbones allow for the fabrication of otherwise thermally unstable electrode compositions in a cermet like configuration. Two different types of microstructures were used in MIII and MIV, with two different, albeit similar, infiltration compositions. In MIII, a macro-porous skeletal type backbone was co-sintered with a Ni-cermet supported BZCY72 membrane, and infiltrated with the same composition as the CeO_2 coated electrode from MII. The pH_2 dependencies for charge and mass transfer agree with the predicted low coverage cases of $pH_2^{1/4}$ and $pH_2^{1/2}$, respectively, but differ from the values reported in MII. The mass transfer activation enthalpies also differ considerably from MII as well, but however still fall within an acceptable range for adsorbed molecular hydrogen dissociation. For BZY, the charge transfer activation enthalpy of approximately 0.75 eV has been calculated for hydrogen spillover and incorporation into buried electrolyte regions near the 3pb, suggesting that this may be the mechanism observed here [147]. The differences are attributed to the low pH_2O atmosphere, where it is likely that that CeO_2 takes on a more reduced state, such as $CeO_{2-\delta}$, and is thus more catalytically active.

The simplified HOR model developed in this work has established a solid basis for fundamental understanding of the reaction kinetics of the metal-electrolyte interface for BZCY72, and has also provided a valuable tool for the interpretation of data in the effort to develop a more effective electrode. For applications incorporating significant concentrations of water-vapor, it would be beneficial to address the competitive adsorption of water-vapor or other OH intermediates.

Pre-exponentials

The charge transfer pre-exponential is representative of geometric aspects of the charge transfer interface, as described in Section 2.3 and in MII. In MII, the area specific 3pb lengths of electrodes with large active areas were estimated through SEM imaging and correlation, yielding values corresponding to the associated charge transfer pre-exponential. These pre-exponentials were then compared to those of the infiltrated backbones in MIII and MIV. The co-sintered backbone electrode from MIII and the graded backbone electrode from MIV were compared to the CeO_2 coated and uncoated electrodes from MII, respectively. Order of magnitude comparisons were conducted, and Table 6.3 gives the areas, estimated area specific 3pb lengths and polarization ASR for the electrodes from MII-MIV. The area specific 3pb length for MIII is lower than

Table 6.3: Charge transfer pre-exponentials, areas and estimated area specific tpb lengths for the Cu and Cu-Co electrodes described in Manuscripts I-IV. The polarization ASR is also shown for $p\mathrm{H}_2 = 0.5$ atm. at 700 °C for comparison.

Manuscript		$\mathrm{Log}(A_{0,ct})$	Area (cm^2)	ℓ_{3pb} ($\mathrm{m\,cm}^{-2}$)	R_p ($\Omega\,\mathrm{cm}^2$)
MII	CeO_2 coated	4.70±0.05	13	20 m	1.7
	Uncoated	5.19±0.02		23 m	2.6
MIII		4.55±0.04	4.7	20 m	1.2
MIV	725 °C	6.30±0.03	4.7	230 m	0.3
	825 °C	4.84±0.02		20 m	0.6

expected when considering the SEM images of the backbone microstructure with the large grain sizes, shown in Fig. 3.1C and in MIII. Other similar backbones have exhibited higher performance, but were subject to degradation and a full data set could not be obtained. Based on post-mortem SEM imaging, both coarsening and microstructure failure early during experimentation are responsible for the loss of 3pb length. When compared to the CeO_2 coated electrode from MII, it is observed that the pre-exponential, area specific 3pb length and polarization ASR's all agree reasonably well. Comparing the values from MIV to the uncoated electrode from MII, the pre-exponentials and ASR values are approximately one order of magnitude different, suggesting that the estimated area specific 3pb length is reasonable.

To the best of our knowledge, this is the first attempt to obtain an analytical relationship of this form between the charge transfer pre-exponential obtained from temperature dependencies, and the geometry of the 3pb region. This work has shown good correlations between A_0 and ℓ_{3pb}, and provides both a better fundamental understanding of the 3pb geometry, and a basis for further development of this methodology in the future.

6.2 Infiltrated backbones

Microstructure

The performance and mechanical stability of backbone microstructures is dependent upon the connectivity of the network, i.e. grain size, necking between grains and to the electrolyte, and upon the surface area with its related porosity. MIII reported the performance of a co-sintered skeletal backbone, and though it has a larger surface area than the as-sintered Ni-BZCY72 membranes, the stresses induced during fabrication make it vulnerable to fracture. MIV utilized a more functional graded backbone consisting of a base layer with approximately 50% porosity and an outer layer that was approximately 70% porous. This approach retained the good mechanical stability and adhesion to the electrolyte, and also yielded a greater surface area. Though the infiltration composition is slightly different between the two electrodes, the order of magnitude difference in 3pb length and the resulting ASR is attributable to the larger surface area of the functional backbone microstructure in MIV. Co-sintering of backbones with Ni-cermet supported electrolytes is difficult due to the formation of a liquid eutectic at high temperature. The eutectic phase, while desirable from a grain-growth and electrolyte conductivity perspective, is detrimental to the formation of a highly porous microstructure. Deng et al. overcame this by using a sintering suppressant, however the same effect was not observed when attempting to co-sinter a porous backbone with unfired NiO-cermet electrode supported membranes fabricated by CoorsTek [37]. As a result, it was determined through numerous iterations of backbone fabrication that in order to form an optimal backbone microstructure, the simple method of using inks with increasing porosity is the best approach. However, it is thought that the two types of backbone microstructures presented in this work may be combined, perhaps incorporating the beneficial aspects of both functional and skeletal backbones.

Combination functional-skeletal backbones

As a preliminary effort to produce a combination functional-skeletal backbone, a co-sintered backbone sample was painted with one coat of a 70 % porous backbone ink and sintered according to MIV. The result of this effort is shown in Fig. 6.1, where the functional backbone microstructure can be seen within the much thicker and more robust skeletal backbone, and gives a direct comparison of the two different types. This sample was then infiltrated with the Cu-Co-CeO_2 composition and reduced, but was short circuited and unable to be tested. However, this shows potential for porous backbone microstructures, where it may be possible to fabricate a tubular backbone supported electrolyte membrane, with a symmetric backbone on the outer surface.

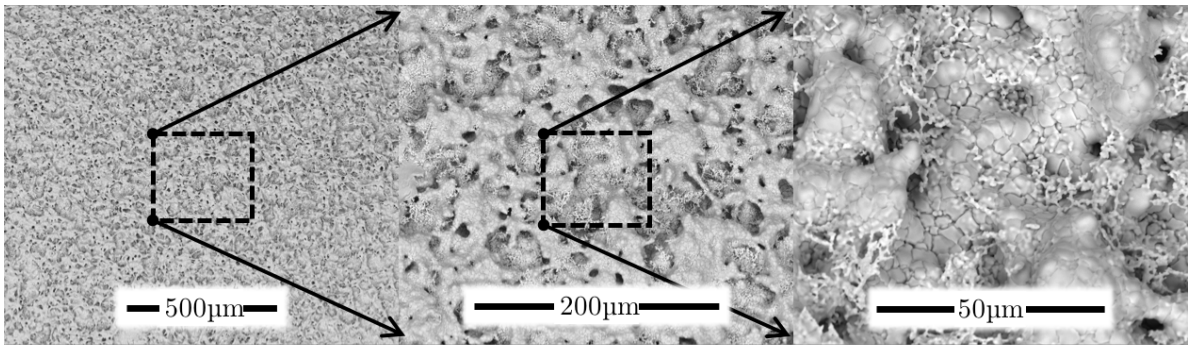

Figure 6.1: A preliminary example of a combination functional-skeletal backbone, utilizing a more robust co-sintered skeletal backbone microstructure to support a functional backbone with a potentially much larger surface area.

Infiltrations

Since the development of the solvent based infiltrations used in this work, there have been other reports of similar solvent based solutions in SOFC literature, showing further precedent for the technique [148, 149]. Both of the cited articles describe better infiltration characteristics than aqueous based solutions alone; such as have been the findings in this work. In MII, when applied to the surface of the sintered Ni-cermet supported BZCY72 tubes, the solution formed homogeneous sub-µm layers which reduced to thin percolated networks of the metals, as seen on the glass slide in Fig. 3.3. The Cu-Co-CeO_2 infiltration composition utilized in MIII provided not only a uniform coverage of the dissolved metal salts, but it was also able to fill the porosity of the backbone microstructure due to the low surface tension of the solvent based solution, as in MIII, Fig. 1B. The formation of the metalloligand type of structure may be disadvantageous if one desired complete loading of the available porosity, as it will decompose in reducing conditions at higher temperatures, however it would be beneficial in preserving better gas diffusion characteristics.

In MIV, the loss of area specific tpb length, as seen in Table 6.3, was due to the coarsening of the Cu-Co-CeO_2 infiltration composition at the 825 °C annealing temperature. This was also accompanied by an increase in the catalytic activity of the infiltrated component, indicated by the decrease in activation enthalpy for both charge and mass transfer (below 675 °C), seen in Table 6.2. The combination of the effects observed in Tables 6.2 and 6.3 suggests that the increase in catalytic activity is due to the exsolution of CeO_2 to the surface of the infiltrated bimetallic composition. This is in effect an inverse catalyst structure such as reported by Rodriguez et al. where there are altered electronic states at the metal-oxide interface [126]. It is proposed that the activity of such a structure, based on the exposure of the catalytically active CeO_2, may be tailored by careful adjustment of the annealing temperature and time.

6.3 Further Results

Further results relevant to the continued development of this work include the hydrogen pumping performance and chemical stability of the Cu-Co and CeO_2 compositions.

Hydrogen pumping

The CeO_2 coated and uncoated Cu-Co electrodes reported in MV were also tested for hydrogen pumping in two different gas compositions. The feed and sweep flow rates were measured using a soap bubble flow meter (Sigma Aldrich), and the sweep outlet composition was measured using an Agilent 3000 μ-GC. Using a sweep gas composition of 5% H_2 in Ar (pH_2O = 0.027 atm.), the bottle-dry feed gas compositions were:

1. 10 % H_2 and 5% He in Ar. (10% H_2 in Ar)
2. 10 % H_2, 5% He, 1% CO and 0.1% each ethane/ethylene in CH_4. (10% H_2 in CH_4)

• MII - CeO_2 coated Cu-Co electrode:

For both compositions 1 and 2 the feed and sweep flow rates were approximately 140 $ml\,min^{-1}$ and 70 $ml\,min^{-1}$, respectively. The low sweep flow rate was used to obtain good resolution in the GC, but limited the number of measurements at each 30 min. current density interval. The high feed flow rate was used to ensure an adequate supply of hydrogen at the anode in the large diameter ProboStat quartz shell tube. The galvanic current density was increased in increments of 10 $mA\,cm^{-2}$ up to 100 $mA\,cm^{-2}$. Each reported data point is the average of the measurements at each current density after reaching equilibrium.

Fig. 6.2 shows plots of the hydrogen pumping results obtained for both compositions 1 and 2. For composition 1, shown in Fig. 6.2 (*top*), the H_2 flux increases in agreement with Faradays law up to approximately 70 $mA\,cm^{-2}$ and 1 V. At higher current densities the rate of the flux increase slows, and the voltage increases at a faster rate, corresponding to an increase in the polarization resistance caused by the mass transfer limitations of the maximum shell flow rate. This corresponds to an increase in polarization resistance, and the faradaic efficiency decreases accordingly. In the plots for composition 2, shown in Fig. 6.2 (*bottom*), the H_2 flux also increases up to approximately 70 $mA\,cm^{-2}$, however, the flux, voltage and faradaic efficiency all behave differently than when operated with hydrogen. Above the 70 $mA\,cm^{-2}$ current density, the flux continues to increase linearly, though at a lesser rate than for composition 1. However, the voltage maintains the same slope with increasing current density. This effect is attributed to carbon deposition on the CeO_2 coated electrode surface due to the electrocatalytic decomposition of CH_4. The detrimental effect of carbon deposition is more apparent in the

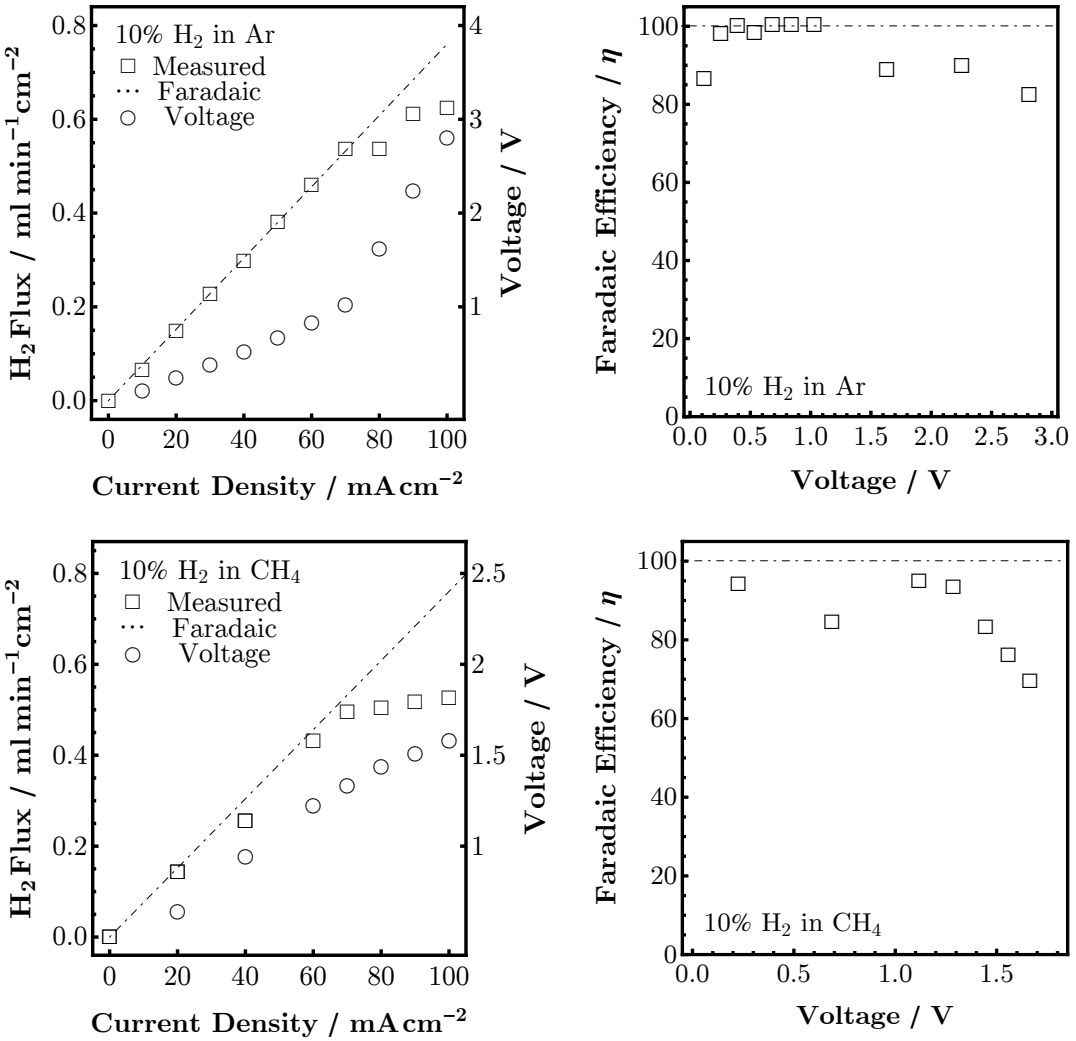

Figure 6.2: H_2 pumping results and the corresponding faradaic efficiencies for the CeO_2 coated Cu-Co electrode from MV, operated in compositions 1 and 2.

plot of faradaic efficiency, where the decrease is more precipitous than for composition 1.

- **MV - Uncoated Cu-Co electrode:**

The feed and sweep flow rates were approximately 140 ml min^{-1} and 110 ml min^{-1}, respectively, for both compositions 1 and 2. The applied current density was again increased in increments of 10 mA cm^{-2}, however only to 80 mA cm^{-2} due to lower performance. Fig. 6.3 shows plots of the hydrogen pumping results obtained for both compositions 1 and 2 using the uncoated Cu-Co electrode from MV. For composition 1, shown in Fig. 6.3 (*top*), the H_2 flux increases linearly with the potential up to a 30 mA cm^{-2} current density, with a corresponding Faradaic efficiency of over 90%. The flux continues to increase up to 40 mA cm^{-2}, however the potential rapidly increased to over 1.25 V. Above 40 mA cm^{-2}, the flux decreased with increasing potential due to an increasing polarization resistance and a lack of catalytic activity for H_2 dissociation,

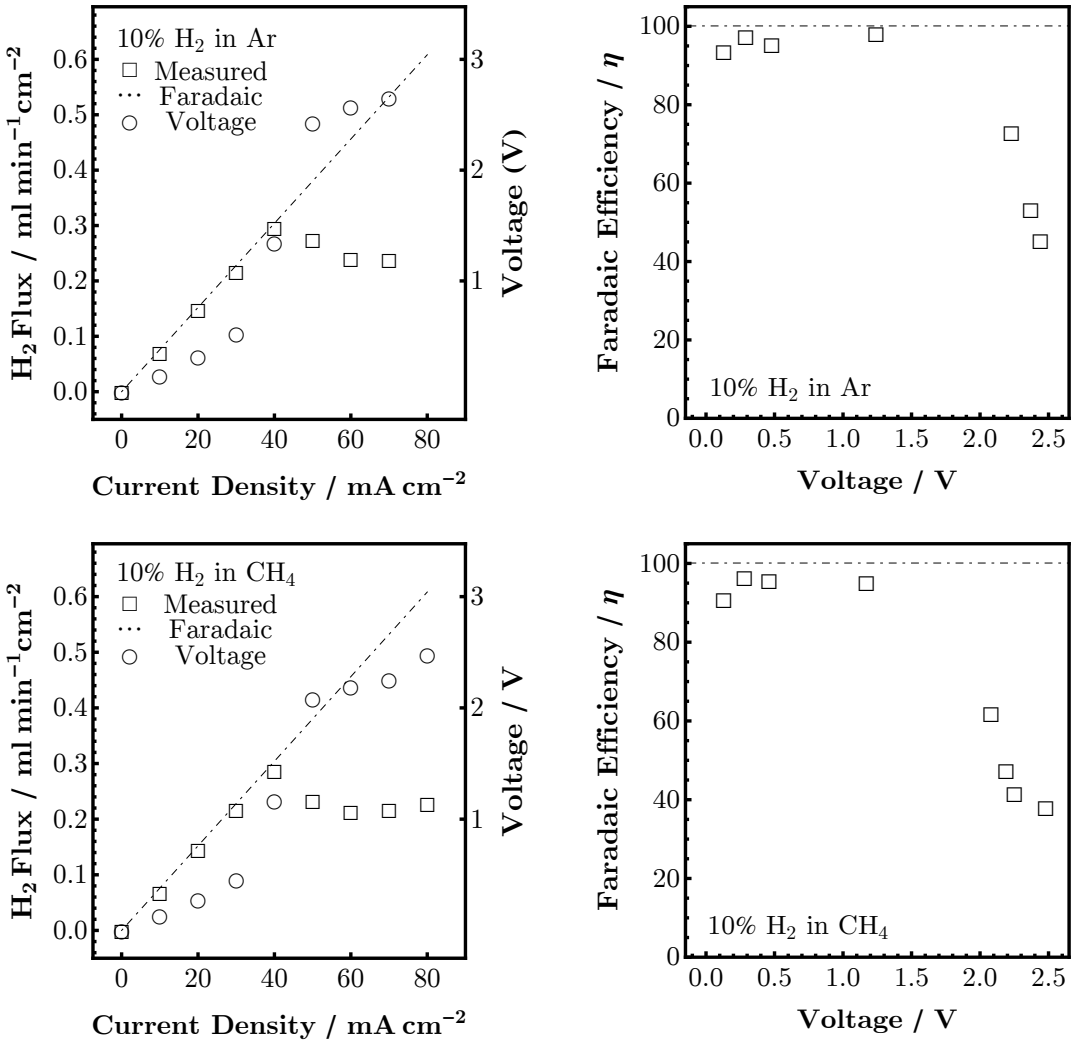

Figure 6.3: H_2 pumping results and the corresponding faradaic efficiencies for the uncoated Cu-Co electrode from MV, operated in compositions 1 and 2.

indicating the limiting current has been reached. For composition 2, shown in Fig. 6.3 (*bottom*), the same characteristics are evident, however, the Faradaic efficiencies are slightly less than for composition 1. Additionally, there is a slight increase in the H_2 flux as the current density is increased further that is likely due to the formation of carbon deposits on the layer of CeO_2 at the metal-electrolyte interface, as seen in Fig. 6.4. In contrast, the carbon deposits on the CeO_2 coated Cu-Co electrode completely covered the electrode surface, and are thus not worthwhile to display. It is not known if this is due to any particular species in gas composition 2, or if it is due to carbonaceous species in general. However, because the Cu-Co metal itself has not accumulated carbon deposits, even at a 25% Co content, it is proposed that further research could be done on that metallic composition, or on a composition incorporating CeO_2 within the metallic phase, such as utilized in MIV.

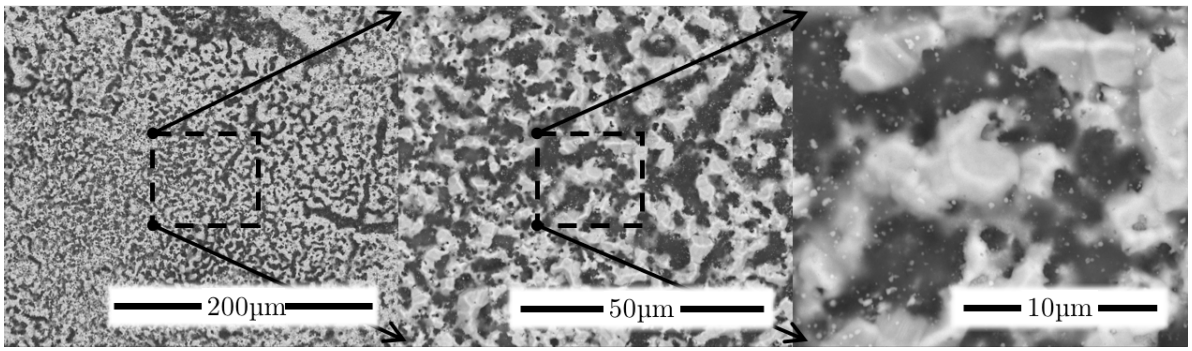

Figure 6.4: Cu-Co metal is visible between the black carbon deposits covering the thin layer of CeO_2 at the charge transfer interface of the uncoated electrode.

6.4 Current challenges

Previous studies of Cu and Cu-based electrodes seemed to be inconclusive as to the viability of the metal for electrode applications in solid state electrochemistry. The compatibility of Cu with electrolyte materials has been addressed in prior literature, and evidence that emphasizes the importance of this question was also observed in this work.

"Is YSZ stable in the presence of Cu?"

In 2008, Ruiz-Morales approached the question of, "Is YSZ stable in the presence of Cu?" [150]. It was found that when sintering Cu-YSZ cermets at temperatures above 900 °C, CuO reacts with YSZ under oxidizing conditions to form monoclinic zirconia, m-ZrO_2, decreasing the bulk conductivity considerably and destabilizing the YSZ structure. A lesser effect was observed when firing in milder reducing conditions (5 % H_2). At 700 °C, there was a darker region beneath the cermet where Cu had diffused into the electrolyte, but when firing at 950 °C that effect was much more pronounced, and Cu had diffused farther into the electrolyte structure. It had already been observed in earlier work that Cu may diffuse from the cermet anode into the electrolyte, and direct evidence of Cu diffusion along YSZ grain boundaries into the bulk had also previously been reported in superconductor literature [61, 151]. Thus, it was recommended that the infiltration method be used to surmount these obstacles, and that when operating in a reducing atmosphere a temperature of less than 700 °C be maintained, otherwise Cu or CuO would penetrate the grain boundaries of the electrolyte.

Stability of the Cu-BZCY72 system

A second Cu point-contact electrode, similar to that reported in MII, was heated to a temperature of 850 °C in order to soften the Cu metal and establish good electrical

contact with the electrolyte. Measurements were then conducted starting at 800 °C, however, the high temperature impedance spectra contained considerable noise and the resulting deconvolutions were unable to provide meaningful data. Upon cooling and subsequent SEM examination of the electrolyte surface, it was observed that Cu metal had diffused into the grain boundaries of the electrolyte, as shown in Fig. 6.5.

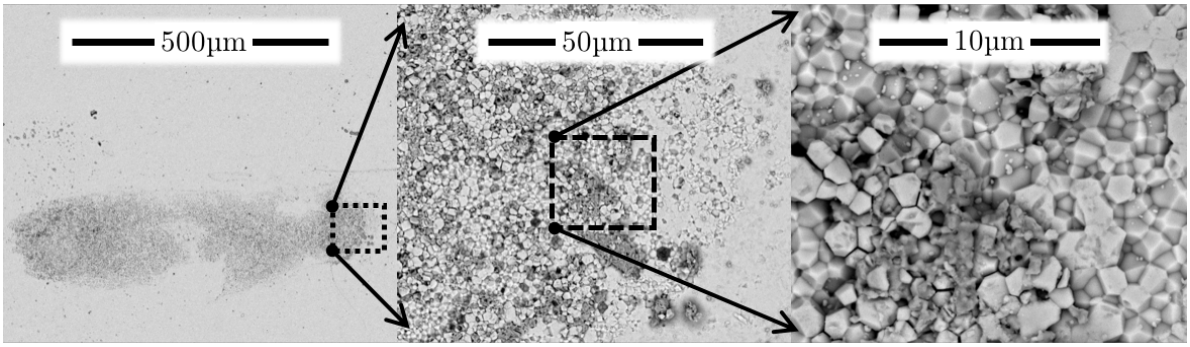

Figure 6.5: A Cu point-contact metal electrolyte interface, where Cu metal is seen to have diffused into the grain boundaries of the BZCY72 electrolyte.

As a result the grains in the region where the metal had diffused into the electrolyte were loose and dislocated, with metal agglomerates forming at the triple points of the grain boundaries. These effects are similar to those described in the previous section, where the same characteristics were observed at temperatures between 700 and 900 °C. Similar results were also observed in BZY backbones when calcining Cu-Co infiltration compositions in oxidizing atmospheres at 850 °C. Results such as this suggest that further research on the diffusivity of Cu metal into the grain boundaries of solid state electrolytes would be beneficial.

6.5 Outlook

For applications where the use of Ni-cermet electrodes is not desirable, alternative solutions are necessary. Through the use of advanced fabrication techniques, unique architectures such as symmetric backbone supported electrolytes may soon become commonplace. The infiltration of such structures with novel electrode compositions then enables the development of membrane-electrode systems which would otherwise not be stable at higher synthesis temperatures.

Cu-Co-CeO_2 anodes have been shown to be both carbon and sulphur tolerant, and are promising candidates for use in biogas and hydrocarbon applications [152, 153]. As an inverse catalyst, CeO_2 particles supported by a metallic Cu-Co phase posses many of the characteristics of excellent electrocatalysts, and can be used to promote reactions

such as the water-gas shift, methanol synthesis through CO_2 hydrogenation, as well as the steam reforming of methane and other alcohols [154–156].

Based on the results of the composition used in MIV, it may be possible to develop even better materials by incorporating Cu and Co into the flourite CeO_2 structure, forming the multi-valent $Cu_xCo_yCe_{1-x-y}O_{2-\delta}$ mixed oxide. Novel Cu-Co-CeO_2 anodes such as developed in this work could be used in combination with oxygen electrode materials, such as the high-performance BGLC (MVI), to create next-generation PCFC technology, operating on carbon containing fuels. Other electrode compositions, such as $Pr_{0.6}Ba_{0.4}Fe_{0.8}Cu_{0.2}O_{3-\delta}$, could potentially be infiltrated into porous backbones and be used in combination with Cu-Co-CeO_2 anodes to develop simultaneous processes such as methane dehydroaromatization and ammonia synthesis [46]. Such a process could utilize CH_4 and air to produce, for example, ethylene and ammonia hydroxide.

7 Concluding remarks

This dissertation has presented the development of a new and simplified hydrogen oxidation reaction model (MI), and has applied the model to the analysis of $p\mathrm{H}_2$ dependencies obtained from impedance data for point-contact, porous metal and infiltrated backbone electrodes. The applicability of the HOR model was established through a comparative study of Cu and Pt point-contact electrodes, and it was found that the hydrogen coverage at adsorption and 3pb sites is likely to be different, and thus yield different coverage terms for the $p\mathrm{H}_2$ depedencies. The model was then able to describe all but one of the $p\mathrm{H}_2$ dependencies presented in the manuscripts included in this dissertation. Such pressure dependencies have been demonstrated to be defining characteristics of rate limiting processes within the overall hydrogen oxidation reaction, and when combined with activation enthalpies, allow the process mechanisms to be identified.

It was found that solvent based Cu-Co metal nitrate solutions exhibit better coating characteristics than their aqueous counterparts, and were thus used to both fabricate porous bimetallic electrodes, and to infiltrate porous backbone microstructures. By comparing the influence of a surface coating of CeO_2 on the catalytic activity of a porous Cu-Co electrode to a second electrode without the coating (MII), it was determined through $p\mathrm{H}_2$ dependencies and activation enthalpies that CeO_2 primarily influences chemical mass transfer via hydrogen dissociation. However, the polarization resistance was dominated by charge transfer and was higher for the uncoated electrode. The HOR model based analysis of the $p\mathrm{H}_2$ dependencies identified the cause of this as a higher "apparent" coverages of molecular hydrogen on the uncoated electrode due to lower catalytic activity. Whereas the dissociative properties of the CeO_2 coating caused the 3pb to instead be populated by atomic hydrogen, thus not requiring a neighboring site for dissociation and effectively reducing the polarization resistance.

As the first of their kind, macro-porous backbones were fabricated by co-sintering with a NiO-BZCY72 supported electrolyte membrane, however, as the results have indicated, this process is far from optimized (MIII). The backbone was infiltrated with the Cu-Co composition, coated with CeO_2, and tested in a low $p\mathrm{H}_2\mathrm{O}$ atm, revealing that the lack of water vapor has a significant impact on the $p\mathrm{H}_2$ dependencies and activation enthalpies. The measured $p\mathrm{H}_2$ dependencies agreed well with the HOR model predictions for low coverage, and the lower activation enthalpies suggested that the electrocatalyst was in a highly reduced state, such as $\mathrm{CeO}_{2-\delta}$, and thus more active towards hydrogen dissociation. These results provide further validation for the proposed HOR model.

A functional backbone of graded porosity was fabricated on a pre-sintered NiO-BZCY72 supported membrane and infiltrated with a Cu-Co-CeO_2 composition. A subsequent investigation of successively higher annealing temperatures revealed changes in activation enthalpies that were attributable to the coarsening of the infiltrated composition. It was found that with a lower annealing temperature the bimetallic phase did not coarsen and extended 3pb length remained intact. The lower annealing temperature exhibited an activation enthalpy indicative of a dissociative adsorption mechanism, however with a higher annealing temperature, the 3pb length decreased and the adsorption mechanism changed to associative adsorption.

The proposed proportionality between the inverse charge transfer resistance, the pre-exponential, $A_{0\,ct}$, and the 3pb length allowed for the estimation of an unknown 3pb length based on the ratio of the A_0's for the known and unknown values. A good correlation was found between these parameters for the porous metal electrodes and the infiltrated backbones, and was further supported by the corresponding ASR values. This provides a solid basis for further development of this new empirical and analytical technique to estimate unknown 3pb lengths, and is a unique opportunity to gain deeper insight into the relatively unknown geometric dimensions of the 3pb region; this is another potential aspect of this work that is worthwhile to pursue in the future.

The CeO_2 coated and uncoated Cu-Co bimetallic electrodes used in MII were tested for hydrogen pumping in dry conditions resembling those found in membrane reactors used for methane dehydroaromatization with an MCM-22 zeolite catalyst. Stable and reasonable performance was observed up to the concentration limitations of the inlet streams, at which point the methane was electrocatalytically decomposed, resulting in significant carbon deposition on the CeO_2. It was reported that the zeolite catalyst benefitted from the co-ionic conduction of oxide ions through the electrolyte, reducing the degradation rate of the MCM-22 due to carbon deposition. To recognize that this effect would first be realized by the electrode would be a significant step forward in the industrialization of this process, however it should be noted that the rate of carbon deposition on the electrode components would ideally be less than that on the zeolite. Carbon deposition on these electrodes was not observed in the data when operating in a $pH_2O = 0.027$ atm. humidified stream of the same gas composition, implying that the CeO_2 coated Cu-Co and Cu-Co-CeO_2 are then possible candidate electrodes for reactions such as methanol or ammonia synthesis from CO_2 and CH_4, respectively, as previously mentioned. Further work could be done to verify this possibility, and if affirmative, then a possible hydrogen solution to the worlds energy needs may be within reach, accompanied by carbon neutral or even carbon negative chemical processing routes.

This dissertation has presented a new, simplified HOR model, and provided insight into the widely sought geometric parameter of the 3pb length. Novel methods for producing Cu-based electrodes have been established, and the role of the CeO_2 electrocatalyst in the hydrogen oxidation reaction on these electrodes has been clarified. Though the high temperature synthesis of Cu containing materials is not generally feasible, further optimization of infiltrated backbone electrodes shows great promise towards the eventual implementation in functional applications. As such, I have high hopes that this work, built upon the labor of the many researchers before me, may be of benefit both to the scientific community and to the world at large.

Bibliography

[1] O. Bičáková , P. Straka, "Production of hydrogen from renewable resources and its effectiveness, International Journal of Hydrogen Energy 37 (2012) 11563–11578.

[2] Q. Wang, "Hydrogen Production", New York, NY, 2012.

[3] M.E. Dry, "The Fischer-Tropsch process: 1950 - 2000", Catalysis Today 71 (2002) 227 – 241.

[4] A.B. Stiles, F. Chen, J.B. Harrison, X. Hu, D.A. Storm, H.X. Yang, "Catalytic conversion of synthesis gas to methanol and other oxygenated products", Industrial & Engineering Chemistry Research 30 (1991) 811–821.

[5] N.Z. Muradov, T.N. Veziroălu, ""Green" path from fossil-based to hydrogen economy: An overview of carbon-neutral technologies", International Journal of Hydrogen Energy 33 (2008) 6804 – 6839.

[6] H. Iwahara, "Hydrogen pumps using proton-conducting ceramics and their applications", Solid State Ionics 125 (1999) 271 – 278.

[7] H. Iwahara, T. Esaka, H. Uchida, N. Maeda, "Proton conduction in sintered oxides and its application to steam electrolysis for hydrogen production", Solid State Ionics 3/4 (1981) 359–363.

[8] A.F. Sammells, M.V. Mundschau (Ed.), "Nonporous Inorganic Membranes", ISBN: 3-527-31342-7, Wiley-VCH Verlag GmbH & Co. Weinheim, 2006.

[9] Y. Larring, T. Norby, "Protons in rare earth oxides", Solid State Ionics 77 (1995) 147 – 151.

[10] T. Norby, R. Haugsrud, "Dense Ceramic Membranes for Hydrogen Separation", in: A.F. Sammells, M.V. Mundschau (Ed.), Nonporous Inorganic Membranes, ISBN 3-527-31342-7, Wiley-VCH Verlag GmbH & Co. Weinheim, Weinheim, 2006, pp. 1–45.

[11] H. Iwahara, H. Uchida, S. Tanaka, "High temperature type proton conductor based on $SrCeO_3$ and its application to solid electrolyte fuel cells", Solid State Ionics 9-10 (1983) 1021–1026.

[12] H. Iwahara, "Proton conducting ceramics and their applications", Solid State Ionics 86-88 (1996) 9–15.

[13] K. Li, "Ceramic Membranes for Separation and Reaction", ISBN 978-0-470-01440, John Wiley & Sons Ltd, England, 2007.

[14] T. Norby, Y. Larring, "Concentration and transport of protons in oxides", Current Opinion in Solid State and Materials Science 2 (1997) 593–599.

[15] Kreuer, K. D., "Proton-conducting oxides", Annual Review of Materials Research 33 (2003) 333–359.

[16] S. Ricote, N. Bonanos, A. Manerbino and W.G. Coors, "Conductivity study of dense $BaCe_xZr_{(0.9-x)}Y_{0.1}O_{(3-\delta)}$ prepared by solid state reactive sintering at 1500°C", International Journal of Hydrogen Energy 37 (2012) 7954 – 7961.

[17] C. Sikalidis (Ed.), "Advances in Ceramics - Synthesis and Characterization, Processing and Specific Applications", Intech, Croatia, pp. 501–519.

[18] J. Guan, S.E. Dorris, U. Balachandran, M. Liu, "Transport properties of $BaCe_{0.95}Y_{0.05}O_{3\alpha}$ mixed conductors for hydrogen separation", Solid State Ionics 100 (1997) 45 – 52.

[19] K. Ryu, S. Haile, "Chemical stability and proton conductivity of doped $BaCeO_3$ - $BaZrO_3$ solid solutions", Solid State Ionics 125 (1999) 355–367.

[20] I. Antunes, G.C. Mather, J.R. Frade, J. Gracio, D.P. Fagg, "Stability of $Ba(Zr,Pr,Y)O_{3-\delta}$ materials for potential application in electrochemical devices", Journal of Solid State Chemistry 183 (2010) 2826 – 2834.

[21] E. Fabbri, L. Bi, H. Tanaka, D. Pergolesi, E. Traversa, "Chemically Stable Pr and Y Co-Doped

Barium Zirconate Electrolytes with High Proton Conductivity for Intermediate-Temperature Solid Oxide Fuel Cells", Advanced Functional Materials 21 (2011) 158–166.

[22] J. Li, J.L. Luo, K.T. Chuang, A.R. Sanger, "Chemical stability of Y-doped Ba(Ce,Zr)O_3 perovskites in H_2S-containing H_2", Electrochimica Acta 53 (2008) 3701–3707.

[23] J. Staniforth, K. Kendall, "Biogas powering a small tubular solid oxide fuel cell", Journal of Power Sources 71 (1998) 275 – 277.

[24] K. Katahira, Y. Kohchi, T. Shimura, H. Iwahara, "Protonic conduction in Zr-substituted $BaCeO_3$", Solid State Ionics 138 (2000) 91 – 98.

[25] S. Ricote, N. Bonanos, G. Caboche, "Water vapour solubility and conductivity study of the proton conductor $BaCe_{0.9-x}Zr_xY_{0.1}O_{3-\delta}$", Solid State Ionics 180 (2009) 990–997.

[26] S. Ricote, G. Caboche, O. Heintz, "Synthesis and proton incorporation in $BaCe_{0.9-x}Zr_xY_{0.1}O_{3-\delta}$", Journal of Applied Electrochemistry 39 (2009) 553–557.

[27] Y. Lin, R. Ran, Y. Guo, W. Zhou, R. Cai, J. Wang, Z. Shao, "Proton-conducting fuel cells operating on hydrogen, ammonia and hydrazine at intermediate temperatures", International Journal of Hydrogen Energy 35 (2010) 2637–2642.

[28] S. Robinson, A. Manerbino, W.G. Coors, "Galvanic hydrogen pumping in the protonic ceramic perovskite $BaCe_{0.2}Zr_{0.7}Y_{0.1}O_{3-\delta}$", Journal of Membrane Science 446 (2013) 99–105.

[29] S. Robinson, A. Manerbino, W.G. Coors, N.P Sullivan, "Fabrication and Performance of Tubular, Electrode-Supported $BaCe_{0.2}Zr_{0.7}Y_{0.1}O_{3--\delta}$ Fuel Cells, Fuel Cells 13 (2013) 584–591.

[30] J.W. Phair, S.P.S. Badwal, "Review of proton conductors for hydrogen separation", Ionics 12 (2006) 103–115.

[31] A. Vourros, V. Kyriakou, I. Garagounis, E. Vasileiou, M. Stoukides, "Chemical reactors with high temperature proton conductors as a main component: Progress in the past decade", Solid State Ionics (2017).

[32] J.D. Kim, G.D. Kim, J.W. Moon, Y.l. Park, W.H. Lee, K. Kobayashi, M. Nagai, C.E. Kim, "Characterization of LSM-YSZ composite electrode by ac impedance spectroscopy", Solid State Ionics 143 (2001) 379 – 389.

[33] M. Sahibzada, B.C.H. Steele, K. Zheng, R.A. Rudkin, I.S. Metcalfe, "Development of solid oxide fuel cells based on a Ce(Gd)O_{2x} electrolyte film for intermediate temperature operation", Catalysis Today 38 (1997) 459 – 466.

[34] V. Dusastre, J.A. Kilner, "Optimisation of composite cathodes for intermediate temperature SOFC applications", Solid State Ionics 126 (1999) 163 – 174.

[35] B.C.H. Steele, "Survey of materials selection for ceramic fuel cells II. Cathodes and anodes", Solid State Ionics 86 (1996) 1223 – 1234.

[36] W. Zhou, R. Ran, Z. Shao, "Progress in understanding and development of $Ba_{0.5}Sr_{0.5}Co_{0.8}Fe_{0.2}$-$O_{3-\delta}$-based cathodes for intermediate-temperature solid-oxide fuel cells: A review", Journal of Power Sources 192 (2009) 231 – 246.

[37] C. Duan, J. Tong, M. Shang, S. Nikodemski, M. Sanders, S. Ricote, A. Almonsoori, R. O'Hayre, "Readily processed protonic ceramic fuel cells with high performance at low temperatures", Science (2015).

[38] R. Strandbakke, E. Vøllestad, S.A. Robinson, M.L. Fontaine, T. Norby, "$Ba_{0.5}Gd_{0.8}La_{0.7}Co_2O_{6-\delta}$ Infiltrated in Porous $BaZr_{0.7}Ce_{0.2}Y_{0.1}O_3$ Backbones as Electrode Material for Proton Ceramic Electrolytes", Journal of The Electrochemical Society 164 (2017) F196–F202.

[39] E.P. Antonova, A.A. Kolchugin, E.Yu. Pikalova, D.A. Medvedev, N.M. Bogdanovich, "Devel-

opment of electrochemically active electrodes for $BaCe_{0.89}Gd_{0.1}Cu_{0.01}O_{3-\delta}$ proton conducting electrolyte", Solid State Ionics (2017) –.

[40] Z. Wang, W. Yang, S.P. Shafi, L. Bi, Z. Wang, R. Peng, C. Xia, W. Liu, Y. Lu, "A high performance cathode for proton conducting solid oxide fuel cells", J. Mater. Chem. A 3 (2015) 8405–8412.

[41] B.C.H. Steele, A. Heinzel, "Materials for fuel-cell technologies", Nature 414 (2001) 345–352.

[42] W.G. Bessler, M. Vogler, H. Stormer, D. Gerthsen, A. Utz, A. Weber, E. Ivers-Tiffee, "Model anodes and anode models for understanding the mechanism of hydrogen oxidation in solid oxide fuel cells", Phys. Chem. Chem. Phys. 12 (2010) 13888–13903.

[43] L. Bi, E. Traversa, "Steam Electrolysis by Proton-Conducting Solid Oxide Electrolysis Cells (SOECs) with Chemically Stable BaZrO3-Based Electrolytes", ECS Transactions 68 (2015) 3387–3393.

[44] I. Garagounis, V. Kyriakou, C. Anagnostou, V. Bourganis, I. Papachristou, M. Stoukides, "Solid Electrolytes: Applications in Heterogeneous Catalysis and Chemical Cogeneration", Industrial & Engineering Chemistry Research 50 (2011) 431–472.

[45] M. Zhang, J. Xu, G. Ma, "Proton conduction in $Ba_xCe_{0.8}Y_{0.2}O_{3\alpha}$ + 0.04ZnO at intermediate temperatures and its application in ammonia synthesis at atmospheric pressure", Journal of Materials Science 46 (2011) 4690–4694.

[46] R. Lan, K.A. Alkhazmi, I.A. Amar, S. Tao, "Synthesis of ammonia directly from wet air at intermediate temperature", Applied Catalysis B: Environmental 152 - 153 (2014) 212 – 217.

[47] V. Kyriakou, I. Garagounis, E. Vasileiou, A. Vourros, M. Stoukides, "Progress in the Electrochemical Synthesis of Ammonia", Catalysis Today 286 (2017) 2 – 13.

[48] G.A.Olah, A. Goeppert, G.K.S. Prakash, "Chemical Recycling of Carbon Dioxide to Methanol and Dimethyl Ether: From Greenhouse Gas to Renewable, Environmentally Carbon Neutral Fuels and Synthetic Hydrocarbons", The Journal of Organic Chemistry 74 (2009) 487–498.

[49] S.H. Morejudo, R. Zanón, S. Escolástico, I. Yuste-Tirados, H Malerød-Fjeld, P.K. Vestre, W.G. Coors, A. Martínez, T. Norby, J.M. Serra, C. Kjølseth, "Direct conversion of methane to aromatics in a catalytic co-ionic membrane reactor", Science 353 (2016) 563–566.

[50] H.H Shin, S. McIntosh, "Proton-Conducting Perovskites as Supports for Cr Catalysts in Short Contact Time Ethane Dehydrogenation", ACS Catalysis 5 (2015) 95–103.

[51] S. Liu, K.T. Chuang, J.L Luo, "Double-Layered Perovskite Anode with in Situ Exsolution of a Co–Fe Alloy To Cogenerate Ethylene and Electricity in a Proton-Conducting Ethane Fuel Cell", ACS Catalysis 6 (2016) 760–768.

[52] K.J Laidler, J.H Meiser, B.C. Sanctuary, "Physical Chemistry", Houghton Mifflin, Boston, MA, fourth edition edition, 2003.

[53] K. Christmann, "Interaction of hydrogen with solid surfaces", Surface Science Reports 9 (1988) 1 – 163.

[54] R. O'Hayre, S.W. Cha, W. Colella, F.B. Prinz, "*Fuel Cell Fundamentals*", Wiley, 2^{nd} edition, 2009.

[55] H. Gerischer, The Principles of Electrochemistry, in: H.J.M Bouwmeester, P.J. Gellings (Ed.), "The CRC Handbook of Solid State Electrochemistry", CRC Press, 1997, pp. 25–28.

[56] A.J. Bard, L.R. Faulkner, "Electrochemical methods: fundamentals and applications", Wiley New York, 2 edition, 2001.

[57] S. Park, R. Craciun, J.M. Vohs, R.J. Gorte, "Direct Oxidation of Hydrocarbons in a Solid Oxide Fuel Cell: I. Methane Oxidation", Journal of The Electrochemical Society 146 (1999) 3603–3605.

[58] R. Craciun, S. Park, R.J. Gorte, J.M. Vohs, C. Wang, W.L. Worrell, "A Novel Method for Preparing Anode Cermets for Solid Oxide Fuel Cells", Journal of The Electrochemical Society 146 (1999) 4019–4022.

[59] S. Park, J.M. Vohs, R.J. Gorte, "Direct oxidation of hydrocarbons in a solid-oxide fuel cell", Nature 404 (2000) 265–267.

[60] E.S. Putna, J. Stubenrauch, J.M. Vohs, R.J. Gorte, "Ceria-based anodes for the direct oxidation of methane in solid oxide fuel cells", Langmuir 11 (1995) 4832 – 4837.

[61] N. Kiratzis, P. Holtappels, C.E. Hatchwell, M. Mogensen, J.T.S. Irvine, "Preparation and Characterization of Copper/Yttria Titania Zirconia Cermets for Use as Possible Solid Oxide Fuel Cell Anodes", Fuel Cells Bulletin 1 (2001) 211–218.

[62] S. McIntosh, J.M. Vohs, R.J. Gorte, "An examination of lanthanide additives on the performance of Cu-YSZ cermet anodes", Electrochimica Acta 47 (2002) 3815 – 3821.

[63] S. McIntosh, J.M. Vohs, R.J. Gorte, "Impedance Spectroscopy for the Characterization of Cu-Ceria-YSZ Anodes for SOFCs", Journal of The Electrochemical Society 150 (2003) A1305–A1312.

[64] R.J. Gorte, J.M. Vohs, S. McIntosh, "Recent developments on anodes for direct fuel utilization in SOFC", Solid State Ionics 175 (2004) 1–6.

[65] J.C. Ruiz-Morales, P. Núnez, R. Buchanan, J.T.S Irvine, "Electrochemical Studies of Nickel and Copper/Yttria Titania Zirconia Ceria Cermets", Journal of The Electrochemical Society 150 (2003) A1030–A1036.

[66] A. Atkinson, S. Barnett, R.J Gorte, J.T.S Irvine, A.J. McEvoy, M. Mogensen, S.C. Singhal, J. Vohs, "Advanced anodes for high-temperature fuel cells", Nature Materials 3 (2004) 17–27.

[67] S.I. Lee, K. Ahn, J.M. Vohs, R.M. Gorte, "Cu-Co Bimetallic Anodes for Direct Utilization of Methane in SOFCs", Electrochemical and Solid-State Letters 8 (2005) A48–A51.

[68] M.D. Gross, J.M. Vohs, R.J. Gorte, "Enhanced Thermal Stability of Cu-Based SOFC Anodes by Electrodeposition of Cr", Journal of The Electrochemical Society 153 (2006) A1386–A1390.

[69] S.W. Jung, J.M. Vohs, R.J. Gorte, "Preparation of SOFC Anodes by Electrodeposition", Journal of The Electrochemical Society 154 (2007) B1270–B1275.

[70] M.D. Gross, J.M. Vohs, R.J. Gorte, "A study of thermal stability and methane tolerance of Cu-based SOFC anodes with electrodeposited Co", Electrochimica Acta 52 (2007) 1951–1957.

[71] H. He, R.J. Gorte, J.M. Vohs, "Highly Sulfur Tolerant Cu-Ceria Anodes for SOFCs", Electrochemical and Solid-State Letters 8 (2005) A279–A280.

[72] M.D. Gross, J.M. Vohs, R.J. Gorte, "Recent progress in SOFC anodes for direct utilization of hydrocarbons, J. Mater. Chem. 17 (2007) 3071–3077.

[73] F. Giannici, A. Longo, K.D. Kreuer, A. Balerna, A. Martorana, "Dopants and defects: Local structure and dynamics in barium cerates and zirconates", Solid State Ionics 181 (2010) 122 – 125.

[74] H. Zhu, S. Ricote, W.G. Coors, C. Chatzichristodoulou, R.J. Kee, "Equilibrium and transient conductivity for gadolium-doped ceria under large perturbations: II. Modeling, Solid State Ionics 268, Part A (2014) 198 – 207.

[75] N. Bonanos, "Transport properties and conduction mechanism in high-temperature protonic conductors", Solid State Ionics 53-56 (1992) 967 – 974.

[76] M. Dippon, S.M. Babiniec, H. Ding, S. Ricote, N.P. Sullivan, "Exploring electronic conduction through $BaCe_xZr_{0.9-x}Y_{0.1}O_{3-\delta}$ proton-conducting ceramics", Solid State Ionics 286 (2016) 117 – 121.

[77] V. Kyriakou, I. Garagounis, A. Vourros, E. Vasileiou, A. Manerbino, W.G. Coors, M. Stoukides,

"Methane steam reforming at low temperatures in a $BaZr_{0.7}Ce_{0.2}Y_{0.1}O_{2.9}$ proton conducting membrane reactor", Applied Catalysis B: Environmental 186 (2016) 1 – 9.

[78] T. Ishihara (Ed.), "Proton Conductivity in Perovskite Oxides", Springer US, Boston, MA, pp. 217–238.

[79] S. Tao, J.T.S. Irvine, "Conductivity studies of dense yttrium-doped $BaZrO_3$ sintered at 1325 °C", Journal of Solid State Chemistry 180 (2007) 3493 – 3503.

[80] Y. Yamazaki, R. Hernandez-Sanchez, S. M. Haile, "High Total Proton Conductivity in Large-Grained Yttrium-Doped Barium Zirconate", Chemistry of Materials 21 (2009) 2755–2762.

[81] Y. Yamazaki, F. Blanc, Y. Okuyama, L. Buannic, J.C Lucio-Vega, C.P Grey, S.M. Haile, "Proton trapping in yttrium-doped barium zirconate", Nat Mater 12 (2013) 647 – 651.

[82] W.H. Chen, P.C. Hsu, "Hydrogen permeation measurements of Pd and Pd-Cu membranes using dynamic pressure difference method", International Journal of Hydrogen Energy 36 (2011) 9355 – 9366.

[83] S. Nayebossadri, J.D. Speight, D. Book, "A novel Pd-Cu-Zr hydrogen separation membrane with a high tolerance to sulphur poisoning", Chem. Commun. 51 (2015) 15842–15845.

[84] P.K. Johansson, "Chemisorption of molecular hydrogen on simple metal surfaces", Surface Science 104 (1981) 510 – 526.

[85] W.T Lee, L. Ford, P. Blowers, H.L. Nigg, R.I. Masel, "Why do heats of adsorption of simple gases on platinum surfaces vary so little with surface structure?", Surface Science 416 (1998) 141 – 151.

[86] P. Ferrin, S. Kandoi, A.U. Nilekar, M. Mavrikakis, "Hydrogen adsorption, absorption and diffusion on and in transition metal surfaces: A {DFT} study", Surface Science 606 (2012) 679 – 689.

[87] L.K. Verheij, M.B. Hugenschmidt, B. Poelsema, G. Comsa, "Hydrogen adsorption on clean and oxygen covered Pt(111)", Catalysis Letters 9 (1991) 195–204.

[88] D.J. Auerbach, C.T. Rettner, H.A. Michelsen, "Interaction dynamics of hydrogen at a Cu(111) surface", Surface Science 283 (1993) 1–8.

[89] R. Gorte, L.D. Schmidt, "Desorption kinetics with precursor intermediates", Surface Science 76 (1978) 559 – 573.

[90] P. Nordlander, S. Holloway, J.K. Nørskov, "Hydrogen adsorption on metal surfaces", Surface Science 136 (1984) 59 – 81.

[91] A.N. Pour, Z. Keyvanloo, M. Izadyar, S.M. Modaresi, "Dissociative hydrogen adsorption on the cubic cobalt surfaces: A DFT study", International Journal of Hydrogen Energy 40 (2015) 7064 – 7071.

[92] B. Hammer, J.K. Nørskov, "Electronic factors determining the reactivity of metal surfaces", Surface Science 343 (1995) 211 – 220.

[93] P. Kratzer, B. Hammer, J.K. Nørskov, "Geometric and electronic factors determining the differences in reactivity of H_2 on Cu(100) and Cu(111)", Surface Science 359 (1996) 45 – 53.

[94] W. Dong, V. Ledentu, P. Sautet, A. Eichler, J. Hafner, "Hydrogen adsorption on palladium: a comparative theoretical study of different surfaces", Surface Science 411 (1998) 123–136.

[95] J. Strömquist, L. Bengtsson, M. Persson, B. Hammer", "The dynamics of H absorption in and adsorption on Cu(111)", Surface Science 397 (1998) 382–394.

[96] J. Harris, "Dissociation of hydrogen on metal surfaces, Langmuir 7 (1991) 2528–2533.

[97] M. Noel, K.I. Vasu, "Charge Transfer Kinetics and Diffusion", in: Cyclic voltammetry and the frontiers of electrochemistry, Aspect, 1990, pp. 158–192.

[98] H. Wendt, G. Kreysa, "Electrochemical engineering: science and technology in chemical and other industries", Springer Science &; Business Media, 1999.

[99] A. Abdelrahman, B. Abel, A. Varga, "Towards rational electrode design: quantifying the triple-phase boundary activity of Pt in solid acid fuel cell anodes by electrochemical impedance spectroscopy", Journal of Applied Electrochemistry 47 (2017) 327–334.

[100] J. Fleig, "On the width of the electrochemically active region in mixed conducting solid oxide fuel cell cathodes", Journal of Power Sources 105 (2002) 228 – 238.

[101] A. Bieberle, L.J. Gauckler, "Reaction mechanism of Ni pattern anodes for solid oxide fuel cells, Solid State Ionics 135 (2000) 337 – 345.

[102] R. Radhakrishnan, A. V. Virkar, S. C. Singhal, "Estimation of Charge-Transfer Resistivity of Pt Cathode on YSZ Electrolyte Using Patterned Electrodes", Journal of The Electrochemical Society 152 (2005) A927–A936.

[103] R. Radhakrishnan, A. V. Virkar, S. C. Singhal, "Estimation of Charge-Transfer Resistivity of $La_{0.8}Sr_{0.2}MnO_3$ Cathode on $Y_{0.16}Zr_{0.84}O_2$ Electrolyte Using Patterned Electrodes", Journal of The Electrochemical Society 152 (2005) A210–A218.

[104] R. O'Hayre, D.M. Barnett, F.B. Prinz, "The triple phase boundary a mathematical model and experimental investigations for fuel cells", Journal of the Electrochemical Society 152 (2005) A439–A444.

[105] M. Mogensen, S. Skaarup, "Kinetic and geometric aspects of solid oxide fuel cell electrodes", Solid State Ionics 86–88 (1996) 1151–1160.

[106] Q. Fu, T. Wagner, "Interaction of nanostructured metal overlayers with oxide surfaces", Surface Science Reports 62 (2007) 431–498.

[107] W.G. Coors, "Co-Ionic Conduction in Protonic Ceramics of the Solid Solution, $BaCe_xZr_{y-x}$-$Y_{1-y}O_{3-\delta}$ Part II: Co-Ionic Conduction", in: C. Sikalidis (Ed.), Advances in Ceramics - Synthesis and Characterization, Processing and Specific Applications, 2011, pp. 501–520.

[108] A.R. Manerbino, "Fabrication, characterization, and hydrogen permeation in $BaCe_xZr_{0.9-x}Y_{0.1}$-$O_{3-\delta}$ prepared by solid-state reactive sintering", Ph.D. thesis, Colorado School of Mines, 2013.

[109] S.P. Jiang, "Nanoscale and nano-structured electrodes of solid oxide fuel cells by infiltration: advances and challenges", International Journal of Hydrogen Energy 37 (2012) 449 – 470.

[110] D. Ding, X. Li, S.Y. Lai, K. Gerdes, M. Liu, "Enhancing SOFC cathode performance by surface modification through infiltration", Energy Environ. Sci. 7 (2014) 552–575.

[111] A.J. Samson, M. Søgaard, N. Bonanos, "Electrodes for Solid Oxide Fuel Cells Based on Infiltration of Co-Based Materials", Electrochemical and Solid-State Letters 15 (2012) B54–B56.

[112] F. Zhao, Q. Liu, S. Wang, F. Chen, "Infiltrated multiscale porous cathode for proton-conducting solid oxide fuel cells", Journal of Power Sources 196 (2011) 8544 – 8548.

[113] S. Klinsrisuk, J.T.S. Irvine, "Fabrication and electrochemical characterization of tape cast $BaCe_{0.5}Zr_{0.3}Y_{0.16}Zn_{0.04}O_{3-\delta}$ electrode/electrolyte structures, Solid State Ionics 181 (2010) 168 – 172. 14th International Conference on Solid State Protonic Conductors, Kyoto, Japan, 7-11 September 2008.

[114] J.T. Zhang, F.L. Liang, B. Chi, J. Pu, L. Jian, "Enhanced electrochemical performance of $BaZr_{0.1}Ce_{0.7}Y_{0.1}Yb_{0.1}O_{3-\delta}$ electrodes for hydrogen and methane oxidation in solid oxide fuel cells by Pd or Cu0.5Pd0.5 impregnation", Journal of Power Sources 200 (2012) 29 – 33.

[115] S. Jung, C. Lu, H. He, K. Ahn, R.J. Gorte, J.M. Vohs, "Influence of composition and Cu impregnation method on the performance of Cu/CeO_2/YSZ SOFC anodes", Journal of Power Sources 154 (2006) 42 – 50.

[116] A.J. Samson, M. Søgaard, N. Bonanos, "Electrochemical characterization of infiltrated $Bi_2V_{0.9}$-$Cu_{0.1}O_{5.35}$ cathodes for use in low temperature solid oxide fuel cells", Solid State Ionics 211 (2012) 74 – 79.

[117] M. Kishimoto, M. Lomberg, E. Ruiz-Trejo, N.P Brandon, "Towards the Microstructural Optimization of SOFC Electrodes Using Nano Particle Infiltration", ECS Transactions 64 (2014) 93–102.

[118] S. Ovtar, M. Chen, A.J. Samson, R. Kiebach, "In-situ formed $Ce_{0.8}Gd_{0.2}O_{1.9}$ barrier layers on yttria stabilized zirconia backbones by infiltration - A promising path to high performing oxygen electrodes of solid oxide cells", Solid State Ionics 304 (2017) 51 – 59.

[119] T.X. Sholklapper, C.P. Jacobson, S.J. Visco, L.C. De Jonghe, "Synthesis of dispersed and contiguous nanoparticles in solid oxide fuel cell electrodes", Fuel Cells 8 (2008) 303–312.

[120] K. Roztocki, D. Matoga, J. Szklarzewicz, "Copper(II) complexes with acetone picolinoyl hydrazones: Crystallographic insight into metalloligand formation", Inorganic Chemistry Communications 57 (2015) 22–25.

[121] Y. Chu, Z. Yang, M.T. Rodgers, "Solvation of copper ions by acetone. Structures and sequential binding energies of Cu+(acetone)$_x$, x = 1-4 from collision-induced dissociation and theoretical studies", Journal of the American Society for Mass Spectrometry 13 (2002) 453–468.

[122] K. Brajter, I. Miazek, "Investigations on the effect of aqueous acetone medium on separation of metal ions on Chelex 100 ion-exchanger", Talanta 28 (1981) 759 – 764.

[123] J.W Bae, J.W Lim, K. Mimura, M. Isshiki, "Agglomeration of Copper Thin Film in Cu/Ta/Si Structure", Materials Transactions 45 (2004) 877–879.

[124] C.Y Yang, J.S. Chen, "Investigation of Copper Agglomeration at Elevated Temperatures", Journal of The Electrochemical Society 150 (2003) G826–G830.

[125] M.A. Barteau, "Organic Reactions at Well-Defined Oxide Surfaces", Chemical Reviews 96 (1996) 1413–1430.

[126] J.A. Rodríguez, J. Hrbek, "Inverse oxide/metal catalysts: A versatile approach for activity tests and mechanistic studies", Surface Science 604 (2010) 241–244.

[127] Special Issue, "Catalysis by ceria", Catalysis Today 253 (2015) 1–218.

[128] A. Trovarelli, "Catalytic Properties of Ceria and CeO_2-Containing Materials", Catalysis Reviews 38 (1996) 439–520.

[129] D.R. Mullins, "The surface chemistry of cerium oxide", Surface Science Reports 70 (2015) 42 – 85.

[130] M.S. Hegde, P. Bera, "Noble metal ion substituted CeO_2 catalysts: Electronic interaction between noble metal ions and CeO_2 lattice", Catalysis Today 253 (2015) 40–50.

[131] A. Laachir, V. Perrichon, A. Badri, J. Lamotte, E. Catherine, J.C. Lavalley, J. El Fallah, L. Hilaire, F. Le Normand, E. Quemere, G.N. Sauvion, O. Touret, "Reduction of CeO_2 by hydrogen. Magnetic susceptibility and Fourier-transform Infrared, Ultraviolet and X-ray photoelectron spectroscopy measurements", J. Chem. Soc., Faraday Trans. 87 (1991) 1601–1609.

[132] F. Dvořák, O. Stetsovych, M. Steger, E. Cherradi, I. Matolínová, N. Tsud, M. Škoda, T. Skála, J. Mysliveček, V. Matolín, "Adjusting Morphology and Surface Reduction of CeO_2(111) Thin Films on Cu(111)", The Journal of Physical Chemistry C 115 (2011) 7496–7503.

[133] S. Wang, M. Zheng, M. Li, X. Wu, C. Xia, "Synergistic effects towards H_2 oxidation on the Cu-CeO_2 electrode: a combination study with DFT calculations and experiments", J. Mater. Chem. A 4 (2016) 5745–5754.

[134] G. Avgouropoulos, T. Ioannides, "Kinetics of CO and H_2 oxidation over CuO-CeO_2 and CuO

catalysts", Chemical Engineering Journal 176-177 (2011) 14 – 21.

[135] F. Tonelli, O. Gorriz, A. Tarditi, L. Cornaglia, L. Arrua, M.C. Abello, "Activity and stability of a CuO/CeO_2 catalyst for methanol steam reforming", International Journal of Hydrogen Energy 40 (2015) 13379–13387.

[136] O. Costa-Nunes, R.J. Gorte, J.M. Vohs, "Comparison of the performance of Cu-CeO_2-YSZ and Ni-YSZ composite SOFC anodes with H_2, CO, and syngas", Journal of Power Sources 141 (2005) 241–245.

[137] H.L. Frandsen, P.V Hendriksen, S. Koch, K.K. Hansen, "Determination of the Resistance of Cone-Shaped Solid Electrodes", Journal of The Electrochemical Society 164 (2017) E3035–E3039.

[138] D. Kek, N. Bonanos, "Investigation of hydrogen oxidation reaction on a metal/perovskite proton conductor interface by impedance spectroscopy", Vacuum 61 (2001) 453 – 457.

[139] D. Kek, N. Bonanos, M. Mogensen, S. Pejovnik, "Effect of electrode material on the oxidation of H_2 at the metal - $Sr_{0.995}Ce_{0.95}Y_{0.05}O_{2.970}$ interface", Solid State Ionics 131 (2000) 249 – 259.

[140] T. Horita, N. Sakai, H. Yokokawa, M. Dokiya, T. Kawada, "Characterization of ceria coated YSZ by a platinum point electrode in H_2-H_2O atmosphere", Solid State Ionics 86 - 88, Part 2 (1996) 1259 – 1266.

[141] T. Jacobsen, B. Zachau-Christiansen, L. Bay, M.J. Jørgensen, "Hysteresis in the solid oxide fuel cell cathode reaction", Electrochimica Acta 46 (2001) 1019 – 1024.

[142] F. Mauvy, C. Lalanne, S. Fourcade, J.M. Bassat, J.C. Grenier, "Impedance spectroscopy study of $Nd_2NiO_{4+\delta}$, LSM and platinum electrodes by micro-contact technique", Journal of the European Ceramic Society 27 (2007) 3731 – 3734.

[143] T. Horita, H. Kishimoto, K. Yamaji, Y. Xiong, N. Sakai, M.E. Brito, H. Yokokawa, "Materials and reaction mechanisms at anode/electrolyte interfaces for SOFCs", Solid State Ionics 177 (2006) 1941 – 1948.

[144] J.R. Macdonald, E. Barsoukov (Ed.), Impedance Spectroscopy: Theory, Experiment, and Applications, John Wiley & Sons Ltd, 2005.

[145] D. Johnson, "ZView: A Software Program for EIS Analysis, Version 2.8", Scribner Associates, Inc., Southern Pines, NC, 2008.

[146] B.A. Boukamp, H.J.M. Bouwmeester, "Interpretation of the Gerischer impedance in solid state ionics", Solid State Ionics 157 (2003) 29 – 33.

[147] M. Malagoli, M. L. Liu, H. C. Park, A. Bongiorno, "Protons crossing triple phase boundaries based on a metal catalyst, Pd or Ni, and barium zirconate", Phys. Chem. Chem. Phys. 15 (2013) 12525–12529.

[148] M.C. Tucker, "Development of High Power Density Metal-Supported Solid Oxide Fuel Cells", Energy Technology 5 (2017) 1–8.

[149] S. Lee, K. Gerdes, "Functional Nanostructure Engineering of SOFC Cathode by Solution Infiltration", ECS Electrochemistry Letters 4 (2015) F17–F20.

[150] J.C. Ruiz-Morales, J. Canales-Vazquez, D. Marrero-Lopez, J. Pena-Martinez, A. Tarancon, J.T.S. Irvine, P. Nunez, "Is YSZ stable in the presence of Cu?", J. Mater. Chem. 18 (2008) 5072–5077.

[151] A.L. Vasiliev, E. Olsson, J. Boikov, T. Claeson, N.A. Kiselev, "Interfacial interactions of YBa_2-Cu_3O_{7x} thin films on Si substrates with polycrystalline Y stabilized ZrO_2 buffer layers", Physica C: Superconductivity 253 (1995) 297 – 307.

[152] A. Al-Musa, M. Al-Saleh, A. Al-Zahrani, N. Kaklidis, G.E. Marnellos, "Electro-Catalytic and Fuel Cell Studies in an Internal Reforming Iso-Octane Fed SOFC Using Cu/CeO2 Composites

As Anodic Electrodes", ECS Transactions 66 (2015) 125–136.

[153] A. Fuerte, R.X. Valenzuela, M.J. Escudero, L. Daza, "Study of a SOFC with a bimetallic Cu-Co-ceria anode directly fuelled with simulated biogas mixtures", International Journal of Hydrogen Energy 39 (2014) 4060 – 4066.

[154] J.A. Rodriguez, P. Liu, J. Graciani, S.D. Senanayake, D.C. Grinter, D. Stacchiola, J. Hrbek, J. Fernández-Sanz, "Inverse Oxide/Metal Catalysts in Fundamental Studies and Practical Applications: A Perspective of Recent Developments", The Journal of Physical Chemistry Letters 7 (2016) 2627–2639.

[155] S.D. Senanayake, P.J. Ramírez, I. Waluyo, S. Kundu, K. Mudiyanselage, Z. Liu, Z. Liu, S. Axnanda, D.J. Stacchiola, J. Evans, J.A. Rodriguez, "Hydrogenation of CO_2 to Methanol on CeO_x/Cu(111) and ZnO/Cu(111) Catalysts: Role of the Metal–Oxide Interface and Importance of Ce^{3+} Sites", The Journal of Physical Chemistry C 120 (2016) 1778–1784.

[156] J.A. Rodriguez, D.C. Grinter, Z. Liu, R.M. Palomino, S.D. Senanayake, "Ceria-based model catalysts: fundamental studies on the importance of the metal-ceria interface in CO oxidation, the water-gas shift, CO_2 hydrogenation, and methane and alcohol reforming", Chem. Soc. Rev. 46 (2017) 1824–1841.

8 Appendix

Manuscript V

Galvanic hydrogen pumping in the protonic ceramic perovskite $\mathbf{BaZr_{0.7}Ce_{0.2}Y_{0.1}O_{3-\delta}}$

Shay Robinson, Anthony Manerbino, W. Grover Coors
Journal of Membrane Science, **446** 99-105 2013

Journal of Membrane Science 446 (2013) 99–105

Contents lists available at ScienceDirect

Journal of Membrane Science

journal homepage: www.elsevier.com/locate/memsci

Galvanic hydrogen pumping in the protonic ceramic perovskite $BaCe_{0.2}Zr_{0.7}Y_{0.1}O_{3-\delta}$

Shay Robinson [a], Anthony Manerbino [a,b], W. Grover Coors [b,*]

[a] Colorado Fuel Cell Center, Department of Mechanical Engineering, Colorado School of Mines, Golden, CO 80401, USA
[b] CoorsTek Inc., Golden, CO 80401, USA

ARTICLE INFO

Article history:
Received 21 March 2013
Received in revised form
8 June 2013
Accepted 18 June 2013
Available online 26 June 2013

Keywords:
Protonic ceramics
Hydrogen membranes
Hydrogen pumping
Membrane reactor

ABSTRACT

A series of experiments were performed on tubular $BaCe_{0.2}Zr_{0.7}Y_{0.1}O_{3-\delta}$ (BCZY27) protonic ceramic hydrogen diffusion membranes in which hydrogen flux was obtained using a tube-in-shell test apparatus with a 22-cm^2 membrane active area and hermetic glass seals. This was accomplished by measuring permeate composition using a mass spectrometer and bubble-meter measurement of outlet flow rates over a broad range of current densities and furnace temperatures. A maximum current efficiency of 98.6% was achieved at 775 °C at 800 mA cm^{-2}, producing over 6 nmL cm^{-2} min^{-1} of hydrogen at virtually 100% selectivity. The data generated through these experiments has been valuable in the evaluation of fabrication methods and hermetic sealing techniques required for large area membranes that are suitable for commercialization. Applications include hydrogen separation, ammonia synthesis and gas-to-liquids fuel processing via methane dehydrogenation. Additionally, the experiments provided valuable insight into the charge-transport processes in BCZY27 membranes where multiple charge carrier species are involved.

1. Introduction

Rare earth-doped perovskites continue to be developed as proton-conducting electrolyte membranes for fuel cells, electrolyzers, membrane-reactors and associated applications where galvanic hydrogen separation is involved [1–6]. The stability of many of these materials under reducing atmospheres and their high protonic conductivity at intermediate temperatures of around 600–700 °C, makes them well-suited for these purposes. Solid solutions of yttrium-doped barium cerate and barium zirconate, such as the $BaCe_{0.2}Zr_{0.7}Y_{0.1}O_{3-\delta}$ (BCZY27) described herein, have been shown to exhibit the desirable characteristics of high protonic conductivity and long-term chemical and mechanical stability [7,8]. Galvanic hydrogen pumping using proton-conducting ceramics has previously been described using button-type cells with active areas of only about 1 cm^2 [1–3,9,10]. This present work describes devices fabricated in a tubular architecture having a 22-cm^2 active-area format. The large active-area membrane tubes have a much smaller seal-to-area ratio than buttons cells, making it possible to measure hydrogen permeation fluxes more precisely. In this study, closed-one-end (COE) hermetic membrane tubes with double-floating glass seals were developed, and hydrogen flux resulting from a combination of galvanic hydrogen pumping and ambipolar diffusion is reported. The tubular COE BCZY27 membranes of interest are characterized through the measurement of a galvanic hydrogen flux evolved by imposing an external electric potential gradient across the BCZY27 membrane, as shown in Fig. 1. This was accomplished over a wide range of current densities, and a wide range of furnace temperatures. The results of this work are intended to quantify hydrogen flux as a function of current density and furnace temperature, as well as to help improve understanding of the operation and performance of protonic ceramic materials and devices.

2. Experimental

2.1. Membrane electrode assembly fabrication

$BaCe_{0.2}Zr_{0.7}Y_{0.1}O_{3-\delta}$ (BCZY27) tubular membranes were used (CoorsTek Inc., Golden, CO, USA). These were slip-cast, closed-one-end, 65 wt.% NiO-35 wt.% BCZY27 cermet electrode supported tubes, spray-coated with a dense electrolyte membrane of BCZY27 and co-fired in air at 1585 °C. Fired dimensions of the tubes were 10 mm OD, 8.5 mm ID, and 25 cm in length. The membrane thickness was approximately 25 μm. A 7 cm long band of porous $La_{0.6}Sr_{0.4}Fe_{0.8}Co_{0.2}O_{3-\delta}$ (LSCF) (ESL Electroscience, 4421-A) was hand-painted on the exterior surface of a 12 cm length of tubular membrane, producing an active area of 22 cm^2. The LSCF shell electrode was subsequently sintered in air at 1000 °C for 30 min.

* Corresponding author. Tel.: +1 303 385 7771.
E-mail address: grover.coorstek@me.com (W. Grover Coors).

0376-7388/$ - see front matter © 2013 Elsevier B.V. All rights reserved.
http://dx.doi.org/10.1016/j.memsci.2013.06.026

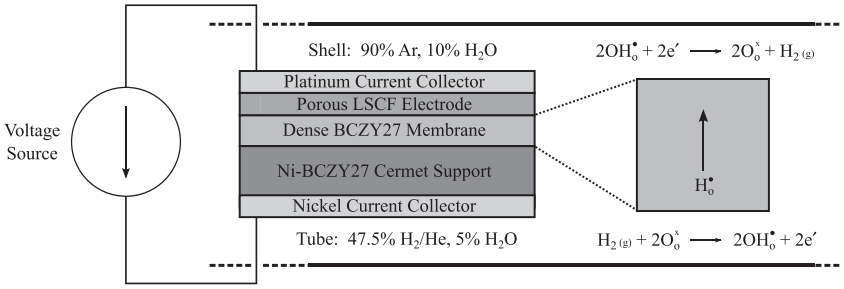

Fig. 1. Principle of galvanic operation for the protonic ceramic hydrogen pump.

The tube electrode current collector was fabricated using a 50 cm length of 4-bore alumina tubing (CoorsTek-65685). A 60 cm length of 1 mm diameter (dia.) silver wire (Alfa-Aesar) was fed through one bore of the four-bore alumina tube to serve as the anode current collector. Sections of nickel mesh, a 7×5 cm of 40-mesh (0.13 mm dia. wire) and a 7×8 cm of 70-mesh (0.11 mm dia. wire, Ed Fagan Inc. Los Angeles, CA, USA), were sequentially wrapped around the 4-bore alumina tube. Two 60 cm lengths of 0.5 mm silver wire were interlaid between the varying grades of Ni mesh as it was wrapped around the alumina rod to serve as the voltage sense wires for a four-point DC connection. This Ni-mesh was then lightly coated with nickel-oxide paste (ESL Electroscience, 4410) and fed into the inside of the cell, seated directly beneath the shell electrode, and counter rotated to expand the mesh and secure the tube current collector in place.

The shell electrode active area was painted with platinum paste (ESL Electroscience, 5542), wrapped with platinum mesh and secured in place with a 1 mm platinum wire (Alfa-Aesar), which also served as the shell electrode current collector. A 0.5 mm platinum wire served as the voltage sense wire and also helped to secure the shell current collector in place. The voltage sense wire was insulated from the active area of the shell electrode using a small alumina tube, completing the four point DC measurement configuration of the membrane electrode assembly (MEA).

2.2. Seal fabrication

The MEA was mounted into a riser-sleeve assembly consisting of two Al_2O_3 (CoorsTek AD-998) ceramic tubes. The riser consisted of a 27 cm length of 9.53 mm outer diameter (OD, CoorsTek-65660) alumina tube; the sleeve was a 2.5 cm length of 12.7 mm OD (CoorsTek-65664) alumina tube. Initially, the sleeve was 9.53 mm inner diameter (ID), however 1 cm of the 2.5 cm length was ID ground to 10.5 mm to accommodate the thermal expansion of the unreduced 65Ni-BCZY27/BCZY27 tubular MEA during heating. Ceramic cement (Resbond FS-989) was used to bond the sleeve to the riser tube, leaving the ID ground portion of the inside of the sleeve exposed. Prior to inserting the cell into place, a small amount of ceramic cement was applied to the top of the riser tube to bond the MEA into position. A thin layer of glass paste (Schott G018-354) was applied to the cell, and it was inserted into place. The remaining open space between the 10.5 mm ID grind of the alumina sleeve and the 10 mm OD cell was filled with glass paste. Once dry, a protective ceramic cap was applied to the top of the joint using ceramic cement.

A second collar, 2 cm long and 15.88 mm OD alumina tube (CoorsTek- 65677) was then fastened over the sleeve, leaving 1 cm of the collars 12.7 mm ID exposed. The resulting open space between the 10 mm cell OD and the 12.7 mm collar ID was also filled with glass paste and capped with ceramic cement. A hemispherical alumina cap, 10 mm ID, was partially coated with glass paste, and fastened to the top of the closed-one-end tubular cell. These involved procedures were found to be necessary to ensure that the seals remained hermetic to helium above 600 °C. A post-testing image of the completed cell assembly is shown in Fig. 2.

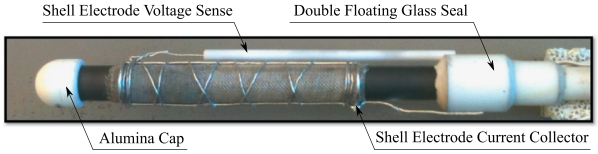

Fig. 2. Post-testing image of the membrane electrode assembly (MEA) and glass seal.

2.3. Test device and tube-in-shell test stand

The completed test cell was installed in the tube-in-shell fixture, shown in Fig. 3. This fixture used a 25 mm OD tubular quartz shell (Quartz Scientific Inc.). Vacuum compression fittings (Swagelok Ultra-Torr) were used at each end to ensure sealing from the ambient atmosphere outside of the furnace hot zone. Shell electrode connections were made using a vacuum feed-through (Kurt J. Lesker). A hot zone thermocouple was placed in the permeant flow stream directly adjacent to the shell electrode. The assembled test device was then installed in the test furnace, with the compression seals located outside of the hot zone.

The tube and shell gases were controlled using mass flow controllers (Alicat Scientific). Humidification for each gas feed was produced using a μL-flow pump (Global FIA Milligat) to inject deionized water through 0.1 mm ID capillary tubing. The water was injected in co-flow with the gas streams through 1.6 mm stainless steel tubing into a stainless steel cylinder heated to 200 °C. All stainless steel tubing was kept at approximately 200 °C using heat rope (Omega) to prevent water vapor condensation. Outlet gas composition on both the feed and permeate sides were measured using an atmospheric pressure Cirrus 2 mass spectrometer, capable of water vapor measurements, directly at the outlet of the test device. The outlet gases then passed through a Nafion drying unit (Perma-Pure MD Series) prior to measurement with a residual gas analyzer (SRS RGA 200).

For the tests described in these experiments, a 5 V power supply was used to provide the potential necessary to drive the desired current density in galvanistatic. An electronic load (Chromaload 6310) was used to monitor voltage and to control the current. In the case of positive potentials between the open circuit potential (V_{oc}) and 0 V (concentration cell), the current flux was driven by the electrochemical Nernst potential of the hydrogen partial pressure gradient across the membrane. The power supply was used for negative potentials only. This applied voltage reversed the polarity of the cell in order to maintain the specified current density, and thus a galvanic potential was applied across the cell electrodes. Cell potential, current density and power

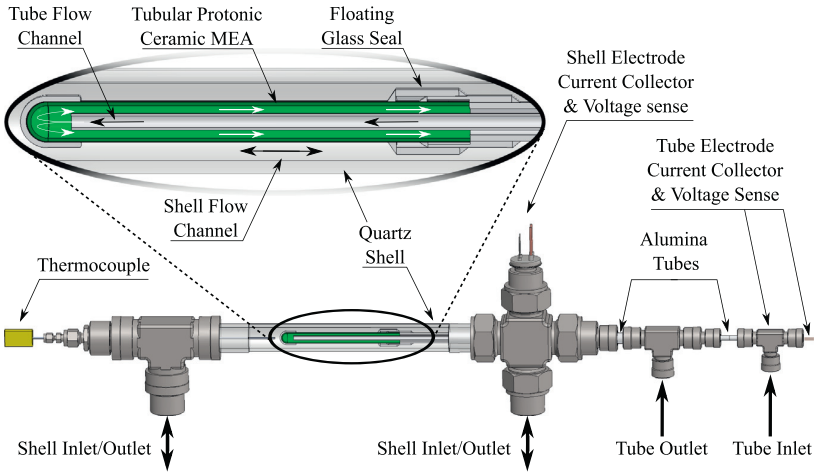

Fig. 3. Model of the assembled tube-in-shell test device to be installed in the test stand.

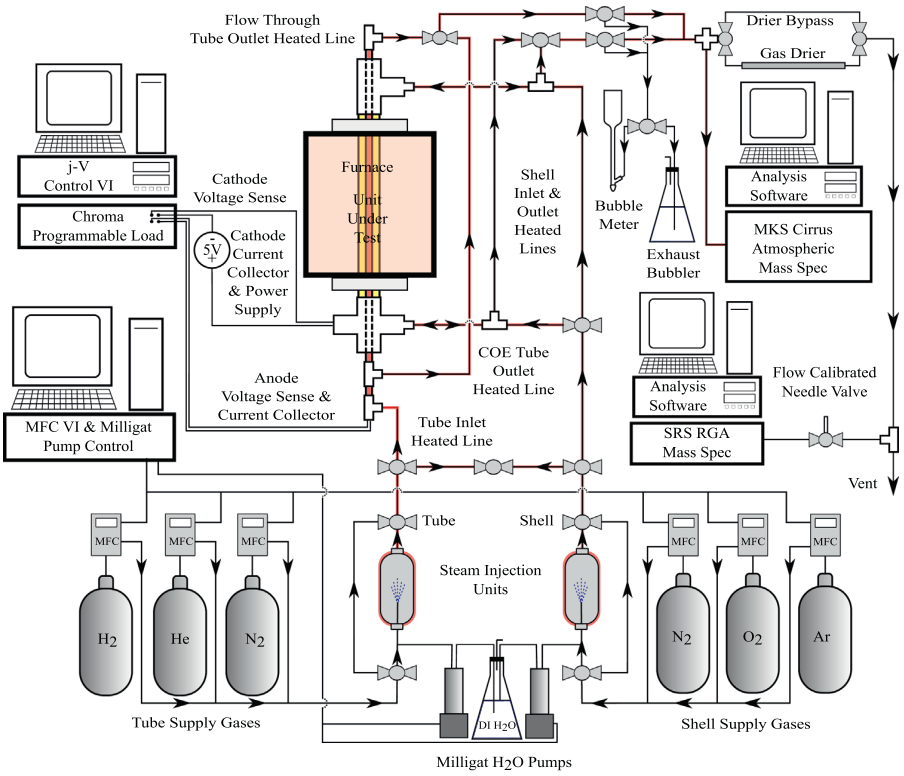

Fig. 4. Tube-in-shell test stand process flow diagram.

density were recorded using a LabView data acquisition program. The complete test stand process flow diagram is shown in Fig. 4. The test stand was designed to test both cast closed-one-end and extruded flow-through tubes with steam concentrations of up to 50%, utilizing co- or counterflow sweep gas directions.

2.4. Sealing and reduction

The furnace was heated to 900 °C at 60 °C h^{-1} with 50 nmL min^{-1} of dry ultra-high purity (UHP) helium and argon

Table 1
Hydrogen pumping test matrix.

Inlet flow rates held constant at 300 mL/min			
Tube composition	47.5% He	47.5% H_2	5% H_2O
Shell composition	90% Ar	10% H_2O	
Current density varied at each temperature			
Temperature	Varied 650 °C to 800 °C		
Current density (A/cm^2)	0, 0.1, 0.2, 0.4, 0.6, 0.8, 1.0		

V

(General Air) in the tube and shell, respectively. Shell outlet gases were continuously monitored for the presence of He with a leak detector (SRS RGA Mass Spectrometer). The integrity of the glass seals was confirmed once the He leak rate fell below 10 ppm prior to in-situ MEA reduction. Once sealing was confirmed and any leak was below the He detection limit in the RGA, the furnace temperature was decreased to 800 °C. Flow rates were slowly increased to 100 nmL min^{-1} and the shell stream hydration was slowly increased to 5%. A dry 2% H_2 balance He mixture was then introduced to the tube stream to reduce the NiO to Ni. Upon complete in-situ reduction, the tube and shell gas compositions were slowly changed to the prescribed test conditions, as seen in Table 1. Current density was varied from 0 to 1 A cm^{-2} in 0.2 A cm^{-2} increments, including 0.1 A cm^{-2}. Temperature was varied 700–800 °C in 25 °C increments, including 650 °C. Flow rates of both the tube and shell gases were measured at each current density for all temperatures using a 100 mL bubble meter (Bubble-O-Meter). Gas volumes were corrected for atmospheric pressure at high altitude and were subsequently averaged to calculate the flow rate for a particular condition. The hydrogen mole fraction was determined from measurements with the Cirrus 2 mass spectrometer, and corrected by subtracting the negligible helium mole fraction (equivalent to noise), assuming that any leak rates of the two gases were equivalent, as shown in Eq. (1).

$$\chi_{H_{2,Actual}} = \chi_{H_{2,Measured}} - \chi_{He} \quad (1)$$

All gases were accounted for using the mass spectrometer with a complete mass balance obtained on both the feed (tube) and permeate (shell) side for each operating condition. The only source of oxygen was water, no molecular oxygen was observed. However, due to the high pH_2 on both sides of the membrane, water-splitting cannot be ruled out.

3. Results and discussion

3.1. Hermeticity of glass seals and electrolyte membrane

Sealing was accomplished using the double floating glass seal described in Section 2.2. Prior to reduction, the cermet support tube was a fully dense ceramic. Glass seals are impermeable between the crystallization temperature and the transformation (softening) temperature, and are also known to be chemically stable and thermally compatible due to modifiable composition [11–14]. After the test device was installed in the furnace, UHP He and Ar were introduced to the tube and shell flow streams, respectively. During heating to 900 °C, the shell outlet composition was monitored continuously with the SRS RGA mass spectrometer. Once the melting temperature of the glass sealant was reached, the He signal dropped below the detection limit (< 10 ppm) of the instrument, verifying the hermeticity of the seals.

Fig. 5a shows an SEM micrograph of the membrane-electrode assembly (MEA) obtained after more than 1000 h of operation in moist hydrogen. The approximately 25 μm thick LSCF shell electrode exhibits excellent porosity and adhesion to the BCZY27 membrane surface. A bright field TEM image of the electrolyte membrane grain boundaries is shown in Fig. 5b. A slight interphase reaction between the BCZY27 membrane and the LSCF electrode was observed, as shown in Fig. 6. This reaction zone appears to be approximately 2–3 μm thick and remain isolated to the membrane surface grains. Although EDS confirmed lanthanum migration into the BCZY, no apparent increase in polarization resistance was observed over the duration of the experiment. These characteristics were consistent across all fracture surfaces examined. The thickness of the membrane was consistently 25 μm thick for all specimens. The tube electrode, with percolation of both the Ni and BCZY27 phases, shows open porosity of about 30%. Solid state reactive sintering [15] enables the preparation of a fully dense membrane with defect free grain boundaries and without pinholes. Such a microstructure is required for hermetic operation in hydrogen atmospheres. These images show the outstanding chemical and mechanical stability of both the cermet anode support and the electrolyte membrane.

3.2. Galvanic hydrogen flux

Area specific hydrogen flux was inferred by measuring the tube and shell flow rates as well as the mole fractions of the same streams using the Cirrus 2 mass spectrometer. Flux density, J_{H_2} (nmL cm^{-2} s^{-1}), was calculated by multiplying the Cirrus 2 mass spectrometer measured hydrogen mole fraction, $\chi_{H_{2,Actual}}$ (%), with the corresponding shell flow rate, $\dot{v}_{shell}$ (nmL/min), and dividing by

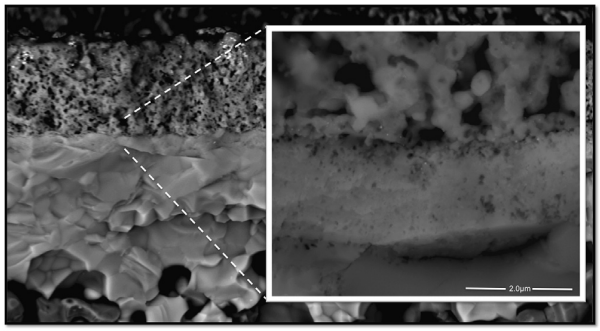

Fig. 6. Phase reaction between the LSCF electrode and the BCZY27 membrane.

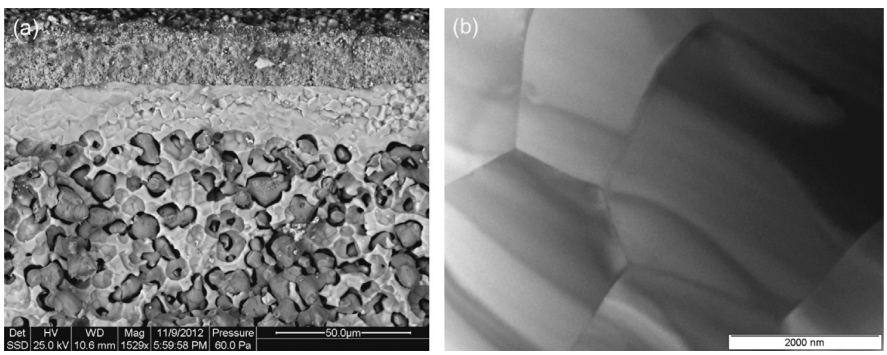

Fig. 5. (a) Post-testing SEM of the Ni-BCZY27 cermet, BCZY27 membrane and LSCF cathode after 1000+ h of operation and (b) bright field TEM image of the BCZY27 membrane.

the active area, A (cm^2), shown in Eq. (2).

$$J_{H_2} = \frac{\chi_{H_2,Actual}\,\dot{V}_{shell}}{A} \tag{2}$$

The theoretical Faradaic flux for each current density was also calculated as in Eq. (3). Here, i is the current density ($A\,cm^{-2}$), n (=2) is the number of moles of electrons transferred per H_2 and F, 96,485 ($C\,mole^{-1}$) is Faradays constant. The relationship between Faradaic current flux , as molar flux ($\mu moles\,cm^{-2}\,s^{-1}$) and volumetric flux ($nmL\,cm^{-2}\,min^{-1}$) is calculated as

$$j_{H_2} = \frac{i}{nF} = 5.182\,\frac{\mu moles}{cm^2\ s} = 7.603\,\frac{nmL}{cm^2\ min} \tag{3}$$

After the cell was reduced and gas compositions were changed to those specified in the test matrix, current density was varied from 0 to 1 $A\,cm^{-2}$, as temperature was varied from 650 to 800 °C. Hydrogen flux, J_{H_2}, was plotted versus current density at each temperature, including the theoretical Faradaic flux, j_{H_2}.

Fig. 7 shows an increase in hydrogen flux with temperature at current densities above 200 m cm^{-2}. At current densities below 200 mA cm^{-2}, the flux was slightly below the theoretical Faradaic prediction, and nearly constant with temperature. In the 400–800 mA cm^{-2} current density ranges, an increase of furnace temperature increases the rate of hydrogen evolution. A maximum flux of 6.0 nmL min^{-1} cm^{-2} was obtained at 775 °C with a current density of 800 mA cm^{-2}. At this current density, the theoretical Faradaic flux is 6.1 nmL min^{-1} cm^{-2}, corresponding to a 98.6% current efficiency. It is noteworthy that when increasing the temperature to 800 °C, the flux decreased slightly at current densities of 600 and 800 mA cm^{-2}. Above about 750 °C, BCZY27 begins to dehydrate, lowering the protonic conductivity, and mixed conductivity then becomes more pronounced. This effect was also observed by other investigators, and has been attributed

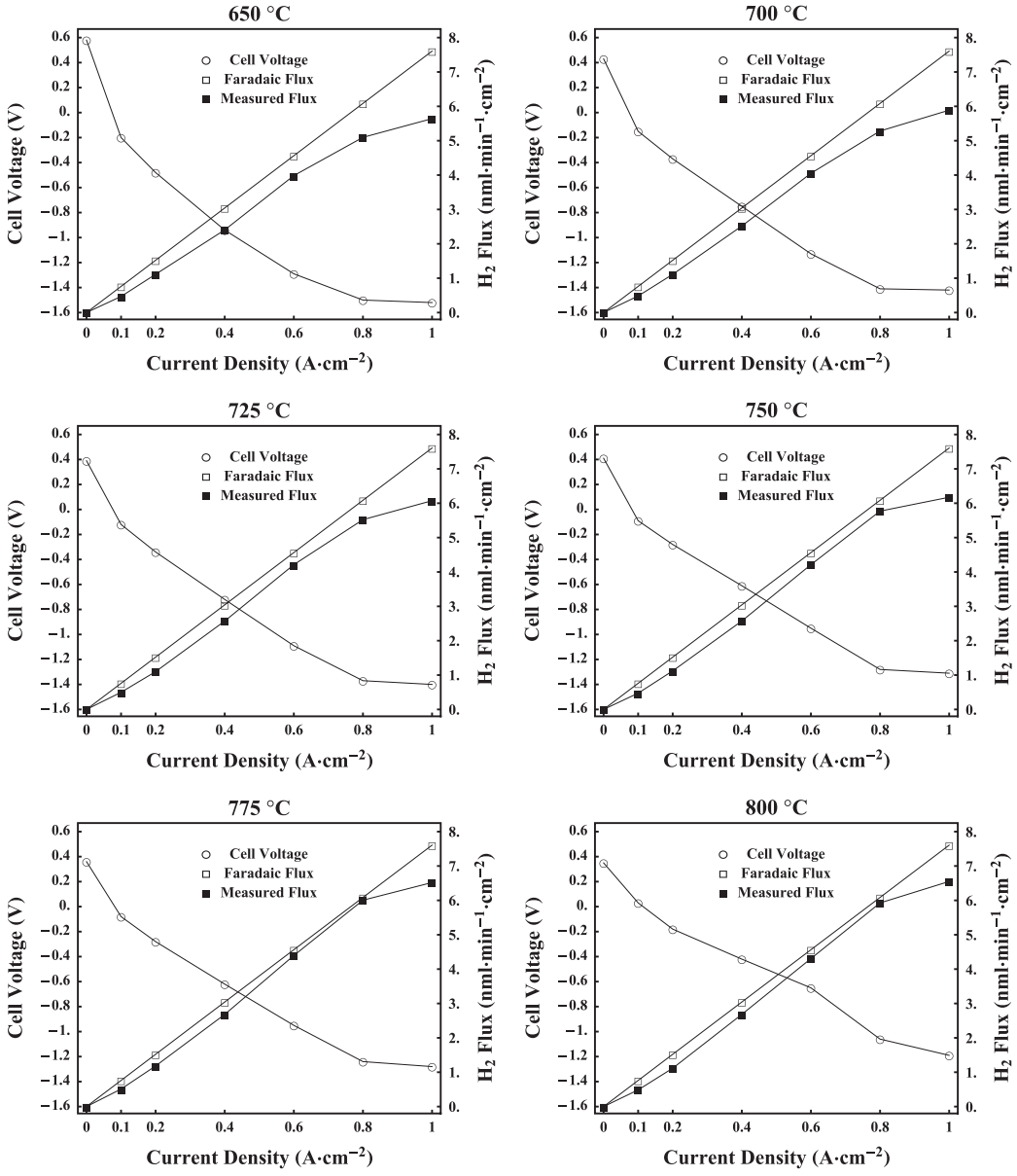

Fig. 7. Galvanic hydrogen flux and the associated voltage, from 650 °C to 800 °C and 0 to 1 A/cm^2.

V

to the increase in electronic conduction, via electron holes, at 800 °C and above [5,9,16,17]. Even though the galvanostatic Faradaic efficiency drops, hydrogen flux continues to increase due to ambipolar diffusion. The corresponding voltage from current densities of 0–100 mA cm^{-2}, indicates that there is a region of operation in which the cell potential is positive, at a non-zero current density (i.e.: sourcing current rather than sinking it), and simultaneously evolves a small but measurable H_2 flux (also described in [18]). As expected with Nernst equation predictions, the open circuit potential decreases with increasing temperature. However, as the temperature increases, a smaller voltage is necessary to drive the current required to evolve hydrogen. In fact, at 800 °C, the cell potential remains positive even at a current density of 100 mA cm^{-2}, simultaneously evolving a flux of 0.47 nmL min^{-1} cm^{-2}. This demonstrates that ambipolar diffusion of protons and electron holes are responsible for some of the flux at positive potential.

3.3. Flow rate mass balance

Flow rates were measured using a bubble-meter and volumes were corrected for altitude. As seen in Table 1, at 300 nmL min^{-1} a 47.5% inlet hydrogen concentration corresponds to 142.5 nmL min^{-1} of hydrogen inlet to the system. At 1 A cm^{-2}, the theoretical flux is 7.6 nmL min^{-1} cm^{-2}, corresponding to 167.2 nmL min^{-1} of H_2 for an active area of 22 cm^2. This correlates the decreased hydrogen flux seen at 1 A cm^{-2} in Fig. 7, with hydrogen concentration limitations at the tube electrode. These effects are also clearly seen in Fig. 8, where outlet flow rates predicted by the theoretical Faradaic flux, plotted as the dashed line, vary from the measured flow rates.

The variability in the tube and shell flow rate data increases at the higher current densities due to the temperature dependence of flux evolution. The variability seen at lower current densities was due to moisture condensation in the line used to measure flow rates. Condensation was accounted for by correcting the outlet flows at 0 A cm^{-2}, assuming no flux under these conditions. This constant correction factor was used throughout flow rate measurements at each current density and temperature. With condensation accounted for, the mass balance of both the tube and shell outlet flow rates varied from the inlet flow by less than 0.5%.

3.4. Faradaic efficiency

The Faradaic efficiency η_F is given in Eq. (4), and plotted as a function of temperature in Fig. 9. This compares the experimentally measured flux (nmL min^{-1} cm^{-2}) to the theoretical Faradaic flux (μmoles s^{-1} cm^{-2}) based on measured current density, as

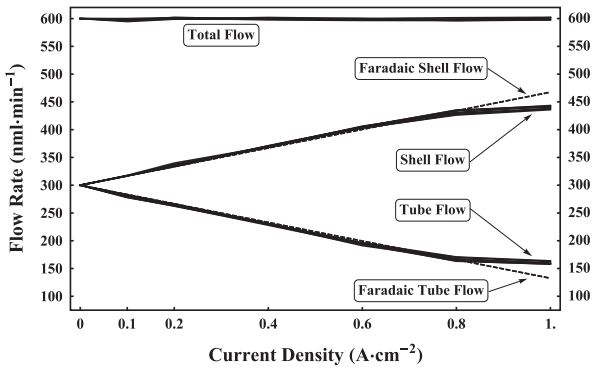

Fig. 8. Flow rates for all hydrogen pumping tests.

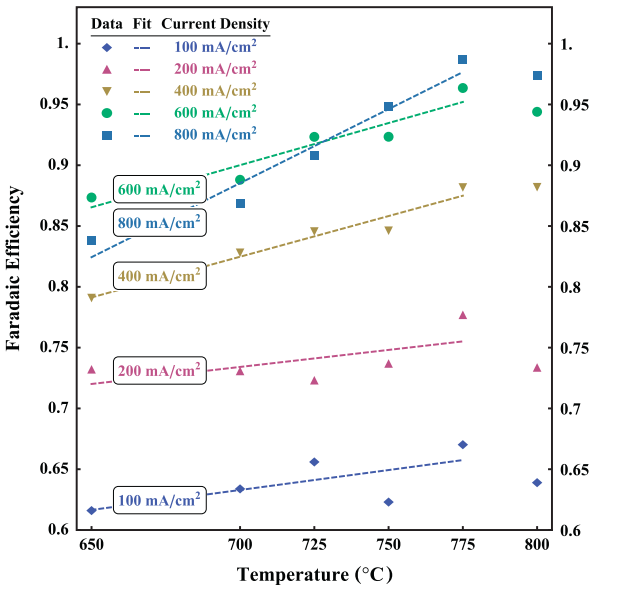

Fig. 9. Faradaic or current efficiency, and the corresponding linear fits from 650 °C to 775 °C.

described in Eq. (3).

$$\eta_F = \frac{J_{H_2}}{j_{H_2}} \tag{4}$$

Experimental data was observed to track closely with the theoretical predictions, and fits were obtained up to 800 mA cm^{-2}. The 1 A cm^{-2} data was not included due to the concentration limitations described in Section 3.3. It is notable that there are three primary slopes to the fits, indicative of different temperature and current dependent regimes of conduction. The slopes of the fits for the measured flux at 100 and 200 mA cm^{-2} show that there is only a small temperature dependency of flux at low current densities, as the Faradaic efficiency varies by less than 5%. The slopes of the fits increase at 400 and 600 mA cm^{-2}, and an increase in hydrogen flux with temperature is also observed. In the flux experiment involving MIECs at open circuit, hydrogen transport is accomplished by the ambipolar diffusion of protons and all of the minority species. The rate determining process at any given temperature is determined by the effective conductivity of the second most mobile species compared to the protons. Therefore, there are temperature regimes where oxygen ion vacancies, electrons and electron holes become rate limiting, with different activation energies, respectively. Since hydrogen transport in these experiments constitutes a mixture of galvanic and ambipolar hydrogen transport, the observation of changing slope of current vs. temperature curves is expected. The Faradaic efficiency reaches a maximum of 98.6% at 775 °C and 800 mA cm^{-2}. The slope of the 800 mA cm^{-2} fit indicates a strong temperature dependence of high-current galvanic operation. The intersection of the 600 and 800 mA cm^{-2} fits near 725 °C shows a change in high-current temperature dependent galvanic operation due to increased oxide ion or electronic conduction. As expected, an increase in oxide ion or electronic conduction will reduce Faradaic efficiency. However, in an oxygen deprived atmosphere an increase in electronic conduction results in higher rates of hydrogen ambipolar diffusion. This results in an increase in hydrogen into the permeate stream, and the apparent increase in Faradaic efficiency at high temperatures. This is an area of active research and will be explored in future work.

4. Conclusion

Experiments were conducted on a $BaCe_{0.2}Zr_{0.7}Y_{0.1}O_{3-\delta}$ (BCZY27) membrane with a large active area of 22 cm^2, over a current density range from 0 to 1 A cm^{-2}, and a temperature range from 650 °C to 800 °C. Galvanic hydrogen flux through this BCZY27 electrolyte membrane has been characterized, and the results obtained agree well with theoretical Faradaic predictions at intermediate temperatures. Flow rates for both the tube and shell gas streams were measured using a bubble meter, and the mass balance of the total flow varied by less than 0.5% from the measured input flow rate; which validates this technique for determining the rate of hydrogen evolved as a function of current density. The helium leak rate was always below the detection limits of both of the mass spectrometers. It was also determined, based on previous works, that shell side water vapor concentrations have a significant effect in preventing too reducing of a permeate stream atmosphere [10]. The current efficiency, or Faradaic efficiency, was shown to be strongly dependent on shell side water vapor concentration. However, in an adequately saturated flow stream such as that described here, the anode hydrogen concentration was observed to become the limiting factor in hydrogen evolution. The experimental apparatus described enables testing hydrogen diffusion membranes over a wide range of operating conditions, and sets the stage for further experimentation aimed at determining the thermodynamic properties of defect species involved in protonic ceramic operation.

References

[1] H. Iwahara, Hydrogen pumps using proton-conducting ceramics and their applications, Solid State Ionics 125 (1999) 271–278.

[2] H. Iwahara, T. Esaka, H. Uchida, N. Maeda, Proton conduction in sintered oxides and its application to steam electrolysis for hydrogen production, Solid State Ionics 3/4 (1981) 359–363.

[3] H. Iwahara, Proton conducting ceramics and their applications, Solid State Ionics 86–88 (1996) 9–15.

[4] T. Schober, High-temperature proton conductors: hydrogen injection and pumping, Ionics 6 (2000) 369–372.

[5] M. Tanaka, T. Ohshima, Recovery of hydrogen from gas mixture by an intermediate-temperature type proton conductor, Fusion Eng. Des. 85 (2010) 1038–1043.

[6] L. Kang, Ceramic Membranes for Separation and Reaction, John Wiley & Sons Ltd, England, 2007, ISBN 978-0-470-01440.

[7] S. Ricote, N. Bonanos, M.C. Marco de Lucas, G. Caboche, Structural and conductivity study of the proton conductor $BaCe_{0.9-x}Zr_xY_{0.1}O_{3-\delta}$ at intermediate temperatures, J. Power Sources 193 (2009) 189–193.

[8] K. Ryu, S. Haile, Chemical stability and proton conductivity of doped $BaCeO_3$-$BaZrO_3$ solid solutions, Solid State Ionics 125 (1–4) (1999) 355–367.

[9] H. Matsumoto, S. Hamajima, H. Iwahara, Electrochemical hydrogen pump using a high-temperature-type proton conductor: improvement of pumping capacity, Solid State Ionics 145 (2001) 25–29, Proceedings of the 10th International Conference on Solid State Protonic Conductors.

[10] H. Matsumoto, Y. Iida, H. Iwahara, Current efficiency of electrochemical hydrogen pumping using a high-temperature proton conductor $SrCe_{0.95}Yb_{0.05}O_{3-\delta}$, Solid State Ionics 127 (2000) 345–349.

[11] J.W. Fergus, Sealants for solid oxide fuel cells, J. Power Sources 147 (1–2) (2005) 46–57.

[12] S.B. Sohn, S.Y. Choi, G.H. Kim, H.S. Song, G.D. Kim, Stable sealing glass for planar solid oxide fuel cell, J. Non-Cryst. Solids 297 (2–3) (2002) 103–112.

[13] Z. Yang, G. Xia, K.D. Meinhardt, K.S. Weil, J.W. Stevenson, Chemical stability of glass seal interfaces in intermediate temperature solid oxide fuel cells, J. Mater. Eng. Perform. 13 (3) (2004) 327–334.

[14] P.L. Rachadel, H. Birol, A.P.N. Oliveira, D. Hotza, Development of alternative glass ceramic seal for a planar solid oxide fuel cell. Adv. Mater. Sci. Eng. (2012), Article ID 346280, 6 pp., http://dx.doi.org/10.1155/2012/346280.

[15] W.G. Coors, Advances in ceramics – synthesis and characterization, processing and specific applications; chap. 21: co-ionic conduction in protonic ceramics of the solid solution, $BaCe_xZr_{y-x}Y_{1-y}O_{3-\delta}$; part I: fabrication and microstructure. Croatia: Intech. ISBN 978-953-307-505-1; 2011.

[16] H. Iwahara, T. Esaka, H. Uchida, T. Yamauchi, K. Ogaki, High temperature type protonic conductor based on $SrCeO_3$ and its application to the extraction of hydrogen gas, Solid State Ionics 18–19 (1986) 1003–1007.

[17] T. Yajima, H. Suzuki, T. Yogo, H. Iwahara, Protonic conduction in $SrZrO_3$-based oxides, Solid State Ionics 51 (1–2) (1992) 101–107.

[18] S. Robinson, Performance Testing of the $BaCe_{0.2}Zr_{0.7}Y_{0.1}$ Electrolyte for Fuel Cells and Membrane Reactors, Master's Thesis; Colorado School of Mines, 2012.

V